Abstract

Single-molecule dynamics in clathrin-mediated endocytosis and membrane remodeling

Michael M. Lacy

2018

In this dissertation, I have investigated the molecular machinery of clathrin-mediated endocytosis (CME) and other proteins that bind and remodel cell membranes, by developing and applying single-molecule fluorescence techniques. Cells use a wide variety of proteins to manipulate their membranes through several mechanisms. Eukaryotic cells use CME to internalize nutrients and other cargo at the cell surface, assembling a complex machinery of over 60 different proteins to deform the flat plasma membrane into a 50-nm vesicle. Notably, the cytoskeletal polymer actin is involved, forming a dense meshwork that assembles and disassembles in about 20 seconds as the clathrin-coated pit invaginates and the vesicle is released. This actin meshwork is essential for successful CME in yeast, to combat the cell's high turgor pressure. These and other observations have led many researchers to propose that the actin meshwork is a key source of force generation in CME. However, key details of this mechanism are still not fully understood.

Based on previous models, we predicted that the individual components of the actin meshwork must continually polymerize and disassemble, turning over multiple times, to generate force in CME, but this prediction has not been verified in cells because

conventional fluorescence microscopy approaches cannot resolve such dynamics. In this dissertation, I developed new cell labeling and imaging protocols to track single molecules within these dense, dynamic assemblies to determine if proteins do exhibit turnover. I recorded populations of single-molecule behaviors in live fission yeast cells by imaging sparsely labeled proteins at the cell membrane and applying super-resolution localization and tracking algorithms. The resulting distributions of lifetimes yield important insights about dynamics within the larger assembly.

I first demonstrated this approach by investigating another membrane-bound structure, the eisosome, an oligomeric scaffold of membrane-bound proteins in yeast. We chose the eisosome as a target for a proof-of-principle that the sparse labeling could reveal single molecule dynamics within large cellular assemblies, because the overall structure appears to be a very stable membrane domain. Surprisingly, my experiments revealed that specifically the subunits at the ends of this linear domain rapidly bind and unbind, like a polymeric filament.

I then imaged and analyzed a number of proteins involved in CME, focusing on key components of actin assembly and disassembly. Surprisingly, their lifetimes are distributed as peaks around 2 to 4 seconds. The shapes of these lifetime distributions suggest complex multi-step pathways, and the fact that many of the actin-meshwork components have similar lifetimes suggests that the residence time of actin-bound proteins is dictated by the lifetime of the actin monomer they bind. Importantly, the single-molecule lifetimes of these proteins are much faster than the overall lifetime of endocytic actin patches (20 sec), indicating rapid turnover during CME.

Other work during my dissertation research explored the intrinsically disordered protein alpha-Synuclein (aSyn). aSyn is a major factor in Parkinson's Disease, and while its normal function in neurons is not fully understood, it is known to bind synaptic vesicles and membranes. aSyn's membrane-remodeling activity may be related to its physiological role in neurons, where it is believed to affect endocytic or exocytic processes or organelle regulation. I measured the binding affinities of several aSyn variants for lipid vesicles and compared their ability to remodel large liposomes. My results showed that the membrane-remodeling activity depends on both the hydrophobicity and length of aSyn's amphipathic helix and its interaction with negatively-charged lipid head groups.

My work contributes to our understanding of membrane-binding and membrane-remodeling mechanisms by directly assessing complex behaviors at the single-molecule level. Pil1p, aSyn, and proteins in the CME machinery all induce curvature of cellular membranes, but their mechanisms and their cellular functions differ widely.

Single-molecule dynamics in clathrin-mediated endocytosis and membrane remodeling

A Dissertation

Presented to the Faculty of the Graduate School

of

Yale University

in Candidacy for the Degree of

Doctor of Philosophy

by

Michael M. Lacy

Dissertation Director: Julien Berro, PhD

May 2018

Table of Contents

Abstract ... **1**

Table of Contents ... **6**

List of Figures and Tables ... **10**

List of frequently used abbreviations ... **11**

Acknowledgements ... **12**

1 Introduction ... **14**

1.1 What is clathrin-mediated endocytosis? ... 14

1.2 Proteins involved in CME ... 15

1.2.1 Membrane Coat Proteins ... *18*

1.2.2 Endocytic Actin meshwork ... *19*

1.2.3 Membrane scission and late regulation ... *21*

1.3 Membrane in CME ... 22

1.4 Forces in CME ... 23

1.5 Comparison of CME in yeast and mammals ... 24

1.6 CME in human health and disease ... 26

1.7 Open questions remaining in CME ... 27

1.8 Conclusions and outlook ... 28

2 Single-molecule imaging of Pil1p ... **29**

2.1 Introduction ... 30

2.2 Results and Discussion ... 32

2.2.1 Quantitative analysis of number of Pil1p molecules and density at eisosomes ... *32*

2.2.2 Single-molecule recovery after photobleaching of Pil1p *33*

2.2.3 Pil1p recruitment is not uniformly distributed *39*

2.2.4 Localization accuracy of sparsely labeled, dynamic eisosome ends *47*

2.2.5 Eisosome ends are specific sites of single-molecule recovery events *47*

2.2.6 Characterization of Pil1p kinetics using SRAP data *50*

2.2.7 SRAP reveals heterogeneities at the nanometer scale in vivo *53*

2.2.8 Filament model for the eisosome *54*

2.3 Conclusions 57

3 Single-molecule turnover dynamics during endocytosis 58

3.1 Background and motivation 58

3.1.1 Predicted turnover dynamics in CME *59*

3.1.2 Super-resolution and single-molecule microscopy *60*

3.2 Results and Discussion: Single-molecule turnover in CME 62

3.2.1 Characterization of single-molecule tracking methods *63*

3.2.2 Lifetimes of actin-bound proteins are limited by actin filament lifetime .. *70*

3.2.3 Fast lifetimes of actin-nucleation factors *74*

3.2.4 Lifetimes of actin-disassembly factors *74*

3.2.5 Lifetimes of membrane-bound proteins *75*

3.2.6 Directed motion of actin meshwork and CCP proteins *76*

3.2.7 Limitations and possible sources of error *82*

3.3 Conclusions and future work 83

4 Alpha-Synuclein membrane binding and membrane remodeling 86

4.1 Introduction 86

4.2 Experimental results 92

4.2.1 Membrane binding characterization by FCS and CD 92

4.2.2 Role of lipid headgroup charge in tubulation capacity 97

4.2.3 Role of aSyn charge and hydrophobicity in binding and remodeling 100

4.2.4 Role of aSyn length in membrane remodeling 101

4.3 Comparison of experimental results with molecular dynamics simulations 102

4.4 Conclusions 103

5 Summary and outlook 105

5.1 Future investigations into CME dynamics 105

5.2 Extensions to this work 106

5.3 Conclusions 107

Appendix 1 Methods 109

A1.1 SRAP of Pil1p 109

A1.1.1 Yeast strains and SNAP labeling 109

A1.1.2 Microscopy 111

A1.1.3 Image analysis and quantification 112

A1.1.4 Quantitative analysis of Pil1p-mEGFP 115

A1.1.5 Characterization of eisosome end localization 115

A1.1.6 Eisosome dynamics model simulations 117

A1.2 Single-molecule tracking in CME 118

A1.2.1 Yeast strains and SNAP labeling 118

A1.2.2 Microscopy 119

A1.2.3 Spot localization and tracking 121

A1.2.4 Tracks analysis *123*

A1.3 aSyn membrane binding and tubulation assays 123

A1.3.1 Protein expression, purification, and labeling *124*

A1.3.2 Vesicles *125*

A1.3.3 Fluorescence Correlation Spectroscopy *125*

A1.3.4 Vesicle tubulation *127*

A1.3.5 Circular Dichroism *128*

References **131**

List of Figures and Tables

Figure 1.1 Overview of clathrin-mediated endocytosis in fission yeast 17

Figure 2.1 Single-molecule recovery after photobleaching of Pil1p-SiR 35

Figure 2.2 SNAP labeling of Pil1p in live fission yeast 37

Figure 2.3 Image analysis for localization of SRAP spots at eisosomes 41

Figure 2.4 Single-molecule recovery of Pil1p-SiR occurs at eisosome filament ends 44

Figure 2.5 Characterization of errors in simulated eisosome end localizations due to sparse labeling 46

Figure 2.6 Alternate models for eisosome recovery dynamics 49

Figure 2.7 Analysis of Pil1p unbinding and binding kinetics 52

Figure 2.8 Model of the eisosome as a dynamic filament 55

Figure 3.1 Characterization of SNAP-tag single-molecule tracking 66

Figure 3.2 Effect of photobleaching on tracking SiR-labeled proteins 68

Figure 3.3 Single-molecule tracking of endocytic proteins 71

Figure 3.4 Assessing Z motion by TIRF intensity 79

Figure 4.1 Schematic of alpha-Synuclein structure 88

Figure 4.2 aSyn binding affinities measured by FCS 94

Figure 4.3 Circular dichroism spectra for aSyn100 and aSyn78 96

Figure 4.4 Vesicle clearance assays measure tubulation capacity of aSyn variants 98

Table 1 Yeast strains used in this study 129

List of frequently used abbreviations

AH: Amphipathic helix

BAR: Bin/Amphyphysin/Rvs domain

CME: Clathrin-mediated endocytosis

CCP: Clathrin-coated pit

FRAP: Fluorescence recovery after photobleaching

LUV: Large unilamellar vesicles

MD: Molecular dynamics

NAC: Non-amyloid-β component of Alzheimer's Disease plaques

PI: Phosphatidyl Inositol

POPG: 1-palmitoyl-2-oleoyl-sn-glycero-3-phosphoglycerol

POPC: 1-palmitoyl-2-oleoyl-sn-glycero-3-phosphocholine

POPE: 1-palmitoyl-2-oleoyl-sn-glycero-3-phosphoethanolamine

POPA: 1-palmitoyl-2-oleoyl-sn-glycero-3-phosphate

POPS: 1-palmitoyl-2-oleoyl-sn-glycero-3-phosphoserine

TIRF: Total internal reflection fluorescence

Acknowledgements

First and foremost, I want to thank my advisor, Professor Julien Berro. I truly appreciate all the support, expertise, and friendly camaraderie that he and the rest of the lab members provide. Julien is a mathematical genius, an insightful scientist, and a supportive mentor, and I consider myself lucky to have joined his lab. I want thank my former advisor, Professor Elizabeth Rhoades, whose support began my PhD training before she left Yale. Liz is not only a talented scientist and a dedicated teacher but is a wonderful person who led an excellent group of people.

I would like to thank my thesis committee, Professors David Baddeley, Enrique De La Cruz, and Shawn Ferguson for their valuable insights and helpful advice. I also thank my former thesis committee, Professors Don Engelman and Art Horwich. All of their advice, high expectations and encouragement have helped me to find the answers to difficult problems over the years. I also thank my outside dissertation reader, Professor Marko Kaksonen, for his valued time and feedback.

None of this work would have been possible in isolation, and so I thank all of the lab-mates I have had over the years. I have had the fantastic benefit of always being able to surround myself with people smarter than me, and I hope that I have contributed some amount that compares to what I have gained from them. From Team Synuclein (Adam, David, Vanessa) and Abhi, Garrett, Xiaohan and the rest of the Rhoades lab, to Ronan, Rui, Neal, Joël, and Alex, and all the summer students and visiting students who have passed through the group, I have learned so much from all of you and greatly enjoyed working with you. I would like to thank the whole Yale West Campus community, and especially the members of the NanoBiology Institute, the Baddeley and Rothman labs for

the use of their microscopes, the lunch gang, and all the friendly faces I get to see every day. I also want to thank my distant collaborators on the Synuclein project, Anthony Braun and Professor Jonathan Sachs. I want to acknowledge and thank all of my classmates and friends, and members of the MB&B department, but there are far too many to name them all individually. I particularly want to thank Professors Andrew Miranker, Enrique De La Cruz, Yong Xiong, Tony Koleske, Tom Pollard, and Mark Solomon for their direct and indirect contributions to my graduate career, both scientific and otherwise.

I want to formally thank my family for all of their love and support through the years. My parents have always supported my curiosity from childhood and throughout my education and scientific training, and I could not have gotten here without them. I'm proud to put another Lacy dissertation in the Yale library, and I thank my aunts and uncles for always sharing their Ann stories. Last but not least, I thank my fiancée Erin for her love and mutual understanding through all the ups and downs of grad school. I am so fortunate that grad school brought us together, and I'm so happy to start the rest of our lives together.

Grad school is hard, and I would not have made it through without all of these fine people. I am so deeply thankful for their humor, friendship, and support, which have kept us all human, although scientists.

1 Introduction

Adapted from Berro J, Lacy MM, Chapter 1 of "Quantitative Biology of Endocytosis", 2018 in press.

1.1 What is clathrin-mediated endocytosis?

All eukaryotic cells use endocytosis to create membrane vesicles at the cell surface. Because the plasma membrane is a physical barrier separating the cytoplasm from the cell's environment, the creation of a vesicle from the plasma membrane is a vital route for molecules to enter the cell. Endocytosis enables the intake of nutrients, recycling of cell surface proteins and lipids, and regulation of cell size. The best characterized endocytic pathway, clathrin-mediated endocytosis (CME) involves assembling a cage of clathrin to specify the size and shape of the membrane vesicle. CME has been a classic system of study in cell biology for decades, and traditional experimental methods in microscopy, genetics, and biochemistry have enabled the identification of the major components and mapping of key steps in the overall assembly pathway (Roth and Porter, 1964; Pearse, 1976; Gaidarov *et al.*, 1999; Kaksonen *et al.*, 2003; McMahon and Boucrot, 2011; Robinson, 2015). However, some key molecular mechanisms remain unresolved, especially because the event occurs within a diffraction-limited area (< 250 nm) and most of the dynamics span only a short amount of time (~20 sec).

The core protein machinery of CME is well-conserved from yeast to mammals and the timing of recruitment of most endocytic proteins has been found to be highly reproducible (Boettner *et al.*, 2011; Taylor *et al.*, 2011). The overall result of CME is the creation of a ~50 nm diameter membrane vesicle from the plasma membrane to be

released into the cytoplasm, usually carrying specific membrane proteins and membrane lipids as cargo. This is achieved by self-assembly of a complex machinery of proteins at a selected site on the membrane, invaginating the membrane into a pit or tubule, then pinching the neck and breaking the membrane into two separate surfaces, as illustrated in Figure 1.1. The protein clathrin forms a cage visible by electron microscopy of vesicles and budding pits, providing a partially spherical shape to the pit and resulting vesicle, but the process is in fact mediated by over 60 other proteins working together, including a dynamic meshwork of cytoskeletal actin filaments. We focus our work on the model organism fission yeast (*Schizosaccharomyces pombe*) because of its historical use for studies of the cytoskeleton and ease of genetic manipulation and experimental conditions, but the proteins and mechanisms are highly conserved to mammals and other eukaryotes.

1.2 Proteins involved in CME

While *in vitro* experiments have identified that the minimal components necessary to reconstitute budding of clathrin-coated vesicles are clathrin, an adaptor protein, and dynamin (Dannhauser and Ungewickell, 2012), the robust, regulated assembly of proteins in cells is much more complex (Figure 1.1). Cargo and site selection and initiation of CME are flexible, with a variety of possible initiation factors and many opportunities for regulation (Cocucci *et al.*, 2012; Brach *et al.*, 2014). We focus on the invagination and formation of the vesicle itself, where robust self-assembly proceeds after these variable early events. Once the earliest initiation factors are assembled, clathrin and other specific proteins are recruited to the site to facilitate the induction of membrane curvature, invagination of the clathrin-coated pit (CCP), and scission. Rather than rely on chronological order of recruitment or divide proteins into distinct “modules”, I will

discuss the functionalities of proteins recruited in CME, keeping in mind that there may be significant regulatory crosstalk and overlap in the timing of recruitment and assembly throughout the pathway.

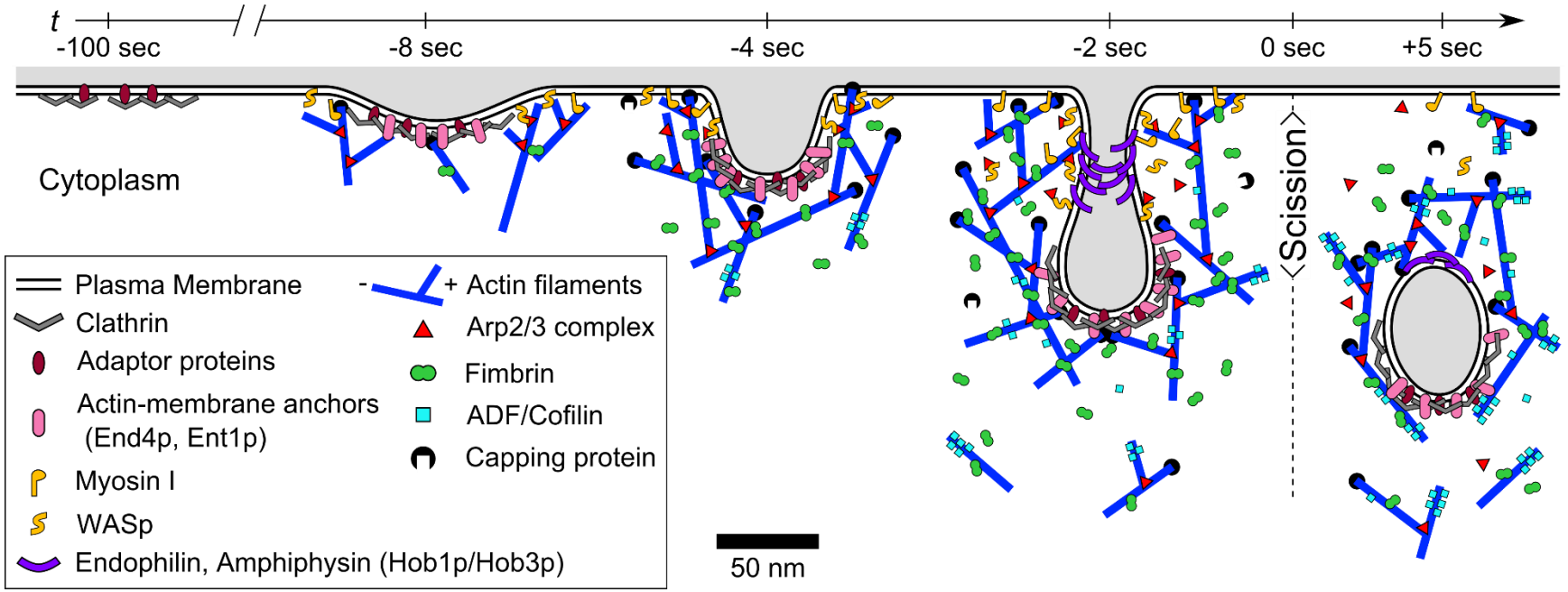

Figure 1.1 Overview of clathrin-mediated endocytosis in fission yeast

Snapshots of a developing vesicle are illustrated with key proteins, as a cross-section along the axis of invagination. Timing (with t = 0 sec as the moment of scission), positions, and numbers of proteins are based on data and models in (Sirotkin *et al.*, 2010; Berro and Pollard, 2014a, b).

1.2.1 Membrane Coat Proteins

The central protein in CME is clathrin. Three heavy chains and three light chains (Chc1p and Clc1p in yeast) form the three-armed triskelion, and many triskelia come together to form a polygonal lattice on the membrane. Clathrin lattices can assemble on flat membranes as purely hexagonal, but the final near-spherical cage is a mix of hexagons and pentagons, requiring some rearrangement (Grove *et al.*, 2014; Avinoam *et al.*, 2015). A number of clathrin adaptor proteins, including the heterotetrameric AP2 complex, mediate the interaction between clathrin and the plasma membrane, controlling the recruitment of clathrin and downstream endocytic proteins to specific sites (Merrifield and Kaksonen, 2014). Many of these membrane-binding proteins contain modular domains such as the BAR (Bin/Amphyphysin/Rvs), ENTH (epsin N-terminal homology), and ANTH (AP180 N-terminal homology) domains to mediate membrane binding and curvature (Kay *et al.*, 1999; Kozlov *et al.*, 2014), and SH3 domains and proline-rich motifs, EH domains, and others to mediate interactions with other proteins, especially factors to recruit actin machinery (Weinberg and Drubin, 2012; Merrifield and Kaksonen, 2014).

These membrane-binding and membrane curvature-inducing proteins are among the earliest proteins recruited to nascent CCPs and often have fine-tuned specificity for certain lipid molecules and membrane shapes. While many of the membrane coat and endocytic adaptor proteins are able to bend membranes and form tubules when added to model lipid membranes *in vitro*, the highly robust assembly of vesicles *in vivo* requires significant regulation across all of the components, and importantly, a significant

contribution of force from an actin meshwork. Many of these early endocytic proteins are localized to a site 1-2 minutes before the onset of invagination and scission.

1.2.2 Endocytic Actin meshwork

A dynamic actin meshwork is required for CME in yeast, providing force to invaginate the membrane to counteract the high turgor pressure and high membrane tension in yeast cells (Boulant *et al.*, 2011; Mooren *et al.*, 2012). In fact, yeast CME is inhibited when actin dynamics are inhibited by drugs or mutations (Sun *et al.*, 2006; Aghamohammadzadeh and Ayscough, 2009), but still occurs in yeast lacking functional clathrin (Payne and Schekman, 1985). Correlative fluorescence and electron microscopy studies have shown that the onset of membrane invagination does not occur until the actin meshwork starts to assemble (Kukulski *et al.*, 2012). A role for actin in CME in mammals was previously underappreciated but recent studies have shown that actin is often involved, and is required in mammalian CME when cells are under high membrane tension or require fast membrane uptake (Boulant *et al.*, 2011; Wu *et al.*, 2016).

Early fluorescence microscopy studies of yeast identified dynamic, diffraction-limited “actin patches” at the cell surface (Marks and Hyams, 1985). Later studies determined that these sites corresponded to CME events, and subsequent work has identified the components of these assemblies in detail (Kaksonen *et al.*, 2003; Sirotkin *et al.*, 2010). The actin meshwork assembled in CME is a dense, highly branched meshwork of short filaments, interconnected by the filament crosslinker Fimbrin (Goode *et al.*, 2015). New filaments are nucleated as branches from existing filaments by the Arp2/3 complex, which is itself recruited and activated by membrane-bound WASp (Wiskott–Aldrich Syndrome protein, Wsp1p in fission yeast, Las17 in budding yeast). WASp is

recruited to the membrane by a number of membrane-bound factors, where it binds and activates a new Arp2/3 complex and binds new actin monomers. The WASp-bound Arp2/3 complex then binds to the side of an actin filament (the "mother filament") and subsequently unbinds from the complex, allowing the Arp2/3-actin surface to polymerize a new "daughter filament".

Most of the filaments are quickly capped by the dimeric actin capping protein (Acp1p/Acp2p in fission yeast, Cap1/Cap2 in budding yeast), and filaments are continually disassembled by actin-depolymerizing factor ADF/Cofilin and Aip1p and other factors, limiting the average length of filaments to around 100-200 nm (Berro *et al.*, 2010). Also at the CME site is type-I Myosin (Myo1p in fission yeast, Myo3/Myo5 in budding yeast), a single-headed non-processive myosin motor which enhances actin nucleation in addition to its motor activity (Sun *et al.*, 2006).

Several of the membrane coat proteins including epsin and HIP1R (*S. pombe* homologues Ent1p and End4p) contain actin-binding domains to anchor the growing meshwork to the CCP tip to elongate the invagination (Skruzny *et al.*, 2012; Sun *et al.*, 2015). FCHo (Syp1p in *S. pombe*), syndapin (Bzz1p in *S. pombe*), and other proteins with BAR domains specifically localize nucleation to sites of curved membrane corresponding to CCPs (Daste *et al.*, 2017).

Models informed by other actin systems predict that a combination of filament polymerization, meshwork elasticity, and myosin motor activity provide sufficient force to invaginate the membrane pit. The set of actin-regulating proteins in CME is similar to those found in lamellipodia of motile cells (Theriot and Mitchison, 1991). In lamellipodia and other actin systems, the dendritic nucleation model explains how a rapidly

treadmilling actin meshwork provides sustained force by polymerizing at its barbed ends while also continuously disassembling filaments at the back of the meshwork (Pollard and Borisy, 2003). However, the actin meshwork in CME exists at much shorter length and time scales, and while models often assume similar dynamics, direct observations of these predicted mechanisms have been elusive. As the coincidence of regulatory proteins results in a coordinated burst of recruitment and actin polymerization, the actin-mediated membrane invagination phase typically takes only 10 seconds until scission.

1.2.3 Membrane scission and late regulation

Membrane scission involves a rapid recruitment of membrane-binding proteins to the neck of the invagination, inducing fission of the narrow membrane tubule into two separate surfaces. In most eukaryotes, membrane scission is mediated by the GTPase dynamin, which forms a helical scaffold around the neck before constricting and inducing breakage of the neck (Roux *et al.*, 2006). Unexpectedly in fission yeast, no dynamin homologue is recruited to the site (Sirotkin *et al.*, 2010), but several other membrane binding proteins are found, including well-conserved homologs of amphiphysin and endophilin, Hob1p and Hob3p. While these BAR-domain containing proteins are also found in late stages of mammalian and budding yeast CME and are able to vesiculate model membranes *in vitro* (Daumke *et al.*, 2014), membrane scission in CME is thought to be primarily mediated through dynamin.

The appearance of these membrane-scission proteins typically occurs in the last few seconds of CME, but some evidence suggests much earlier recruitment and roles in regulation of the progression through invagination (Reis *et al.*, 2015). The combined action of actin-disassembly proteins (and the halt of new filament nucleation) and lipid

phosphatases mediate the disassembly of the actin meshwork and unbinding of the membrane coat proteins while the vesicle diffuses into the cytoplasm.

1.3 Membrane in CME

While much of the attention on CME focuses on the proteins, the membrane itself plays a far more important role than just as a passive substrate. Specific lipid molecules, especially phosphatidyl-inositol (PI) species, mediate the recruitment of proteins and initiate biochemical cascades, contributing to the transitions between different phases of assembly, invagination, and disassembly (Cremona *et al.*, 1999; Di Paolo and De Camilli, 2006). Membrane curvature-sensitive domains are capable of recognizing fine differences in curvature, from the initial flat membrane with local deformations to the unique topologies of the curved CCP, omega-shaped neck, and resulting vesicle (Peter *et al.*, 2004; Bhatia *et al.*, 2009; Antonny, 2011). And while the topology and composition of the membrane influence protein binding, these membrane-binding domains also propagate their preferred curvature and locally enrich their preferred lipids in a positive feedback (Mim and Unger, 2012; Zhu *et al.*, 2012; Simunovic *et al.*, 2015; Madsen and Herlo, 2017). Membrane-binding proteins and changes in topology act as diffusion barriers, limiting the signals and physical properties to specific sites (for example, the newly cleaved vesicle quickly develops a unique composition from the plasma membrane). Thus, lipid composition and shape changes throughout invagination and scission act as key signals in addition to the presence of specific protein factors.

The localization of proteins to the membrane also introduces important biochemical considerations, as their local concentrations are significantly increased by spatial confinement and reduced dimensionality. As the CCP invaginates and various

membrane proteins form lattices or stable coats, the diffusion of lipids and membrane proteins can be restricted or modulated. This simple factor can accelerate biochemical rates, increase apparent binding affinities, and introduce local differences from bulk properties of the plasma membrane.

1.4 Forces in CME

As CME is inherently a physical and mechanical process, an understanding of the forces and motions is essential. Initially, forces must be applied to bend the membrane and move inwards, and later forces act to elongate the tubule and constrict the neck to the point of scission. As noted above, in yeast these forces are typically assumed to be supplied by the dynamic actin meshwork and the contractility of myosin, however the precise mechanistic details are unresolved. The magnitude of force required for CME in yeast is quite high, as the cell wall allows cells to maintain a high turgor pressure, around 0.2 to 1.0 MPa (Minc *et al.*, 2009; Goldenbogen *et al.*, 2016), which must be overcome to invaginate the pit and tubule. Because the plasma membrane exists under tension, the amount of energy required to bend the membrane into a highly-curved pit, and later vesicle, depends on the membrane tension and other features of the membrane itself, including specific lipid composition and membrane-binding proteins (Kozlov *et al.*, 2014).

Membrane fission is a complex process, as the intermediate must be an inherently high-energy transition state. Proteins such as dynamin and amphiphysin/endophilin stabilize the highly-curved states and catalyze the fission step (Roux *et al.*, 2006; Daumke *et al.*, 2014; Mattila *et al.*, 2015). In addition to the high curvature and constriction of membrane-binding proteins around the CCP neck, lipid phase separation

or membrane tension along the tubule driven by the actin meshwork may contribute to scission. The sources of energy to deform the membrane and stabilize the unfavorable intermediates remains an open question, as a number of ATPases (actin, myosin, others), GTPases (dynamin), and other sources of chemical energy and thermal motions may be able to provide the necessary mechanical energy.

1.5 Comparison of CME in yeast and mammals

The core proteins and mechanisms of CME are highly conserved across eukaryotes, and the ease of experimental manipulation of yeast has provided valuable insights to universal mechanisms and conserved protein functions (Boettner *et al.*, 2011). One of the most obvious differences between yeast and mammalian CME is the requirement of actin. This difference was initially ascribed to the much higher membrane tension and turgor pressure in yeast compared with mammalian cells, and indeed actin is recruited in mammalian CME if the membrane tension is artificially raised (Aghamohammadzadeh and Ayscough, 2009; Boulant *et al.*, 2011). Recent studies have made clear that actin is often involved in mammalian CME, if not required, especially in fast endocytic events in the pre-synaptic terminal upon neuron stimulation (Watanabe *et al.*, 2013; Wu *et al.*, 2016). Another key difference is the lack of dynamin in fission yeast CME. Because the precise molecular mechanism of scission is not fully understood, some of the functional aspects of dynamin may be performed by these other BAR domain proteins in fission yeast (Daumke *et al.*, 2014; Simunovic *et al.*, 2017).

An important factor when comparing experimental results between yeast and mammals is the difficulty of true knock-out mutations and control of expression of fusion proteins in mammalian cell culture. While classic genetic techniques enable deletions and

genetic modifications in yeast with relative ease, experiments in human cell culture often relies on imperfect knock-downs or deletion of single isoforms. Throughout evolution, many genes have been duplicated into many isoforms, and the deletion or suppressed expression of one isoform is often coupled with upregulation or increased recruitment of other isoforms or conserved proteins to compensate, obscuring a true effect. Additionally, expressing a gene with a fluorescent marker often relies on transient over-expression of a fusion protein on top of the endogenous expression level or rescuing a deleted gene with expression at a non-native protein level, which may also result in significant cell-to-cell variability in protein levels (Gibson *et al.*, 2013). On the other hand, in yeast it is routine to insert the tag at the native gene locus, maintaining protein expression at endogenous levels. These caveats are increasingly being addressed with the ease of new genome-editing techniques for human cell culture, and indeed genome-edited strains have clarified previously-established findings (Doyon *et al.*, 2011). These considerations are especially important for quantitative experiments and modeling, where precise knowledge of all the factors in the system is crucial for making accurate predictions and conclusions.

Another biological difference in CME between yeast and mammals is the additional variety of cell types and varied mechanisms in higher organisms. Many of the studies of mammalian CME have relied on specialized cell types, stimulated exocytosis/endocytosis in neurons, or adherent cells on a glass surface. Studies from these various scenarios have often suggested variable timing of recruitment or differing requirements of proteins (especially actin) under different conditions (Mettlen *et al.*, 2010), or even between different regions of the same cell types, and divergent endocytic

pathways beyond the canonical clathrin-mediated pathway (Kumari *et al.*, 2010; Johannes *et al.*, 2015). Some of these findings can be attributed to experimental constraints but others do reflect the true diversity of biological mechanisms available to achieve the same function in complex organisms (McMahon and Boucrot, 2011). Rather than focus on the differences across these disparate experimental targets, we emphasize that the fundamental principles still apply and that the variety of mechanisms available to cells highlights their diverse adaptability.

1.6 CME in human health and disease

Given its fundamental importance in cell biology, endocytosis is relevant for many aspects of human health and its dysfunction is implicated in a wide variety of diseases. Regulation of signaling processes by endocytic trafficking contribute to many developmental pathways (Bökel and Brand, 2014). CME is a necessary component of neuron function, recycling membrane after synaptic vesicle fusion and modulating neurotransmitter receptors (Saheki and De Camilli, 2012; von Zastrow and Williams, 2012). Neurological disorders and neurodegenerative diseases such as Alzheimer's or Parkinson's Disease may have both causes and symptoms arising in the endocytic phase of synaptic vesicle recycling (Cataldo *et al.*, 2001; Vargas *et al.*, 2014). Defects in CME are linked to various cancers, where aberrant signaling protein re-uptake contributes to unregulated cell growth and motility (Mellman and Yarden, 2013; Chen *et al.*, 2017). Metabolic disorders can result from defects in nutrient uptake and related endosome/lysosome trafficking (Maxfield, 2014). In addition, many viruses hijack the endocytic machinery to enter and infect host cells (Mercer *et al.*, 2010). In all of these cases, a better quantitative understanding of CME mechanisms may enable insights

beyond the traditional genetic or biochemical aspects of diseases, opening new routes for therapeutic approaches.

1.7 Open questions remaining in CME

Much is known about CME, including the timing and recruitment profiles of key proteins and mechanisms of individual components, and the minimally required proteins are known. However, between the regimes of knowledge at the macro-scale (genetic interactions, recruitment timelines) and molecular scale (biochemistry of individual proteins and interactions, molecular structures), several important gaps remain.

For example, although a dynamic actin meshwork is required for successful CME in yeast, the nanoscale organization and mechanisms of force production in the meshwork are not fully understand. Quantitative models of membrane deformation and actin dynamics have not yet been able to address molecular details due to technical or theoretical constraints. How are actin filaments oriented? How does the meshwork convert chemical energy into mechanical force to deform the membrane? How do the dynamics and interactions across the system of regulatory proteins lead to such a robust self-assembly process? How do these features change over time during the formation of a single endocytic patch?

One major unresolved aspect is how the CME proteins produce enough force to deform the membrane. As will be discussed in Chapter 3, theoretical estimates of the amount of force needed to overcome the turgor pressure in yeast to bend the membrane and invaginate the CCP are significantly higher than estimates of the amount of force produced by actin polymerization. Several other sources of force generation, including meshwork elasticity (Ma and Berro, 2017) and myosin motor activity (Sun *et al.*, 2006),

may help to reach this requirement. Another possible solution to this problem is that if the actin meshwork turns over multiple times, it would generate much more force than previous calculations. While actin turnover has been shown to be an important component of other dynamic actin systems, CME presents unique challenges for experimental study.

1.8 Conclusions and outlook

Much is known about CME through classical cell biology, genetics and microscopy, but some important aspects are still not fully understood. As a fundamental process in eukaryotic cells, CME is well conserved across species, enabling experimental accessibility and universal insights into the assembly and regulation of the proteins involved by using model organisms. Important features which remain unknown include the nanoscale organization, mechanisms and energetics of actin force production, and the system's robust regulation. Quantitative cell biology tools have made critical contributions to our understanding of this complex process, especially quantitative fluorescence microscopy (Sirotkin *et al.*, 2010; Berro and Pollard, 2014a; Picco *et al.*, 2015) and mathematical modeling (Liu *et al.*, 2009; Berro *et al.*, 2010; Carlsson and Bayly, 2014; Lowengrub *et al.*, 2016). New super-resolution microscopy techniques are revealing ultrastructural details on the CME structures in live cells (Mund *et al.*, 2017; Sochacki and Taraska, 2017; Arasada *et al.*, 2018), but the dynamics of these structures are still difficult to observe. As will be discussed in later chapters, modern techniques such as super-resolution microscopy and single-molecule methods are well-positioned to uncover details that conventional microscopy tools have been unable to resolve, leading to new advances in our understanding of CME.

2 Single-molecule imaging of Pil1p

Adapted from Lacy MM, Baddeley D, Berro J (2017). "Single-molecule imaging of the BAR-domain protein Pil1p reveals filament-end dynamics." *Molecular Biology of the Cell* 28:2251-2259.

In this chapter I investigate the eisosome as a proof-of-principle demonstration of sparse labeling for single-molecule detection within dense cellular assemblies. Before assessing single-molecule behaviors in the complex and highly dynamic assembly of CME, we wanted to demonstrate the strategy of sparse labeling to measure single molecule residence times in a different cellular target. The eisosome was an attractive target of study because it was reported to be highly static and yet, paradoxically, it is also known to be rapidly remodeled under cellular stress conditions. My technique, which we call SRAP (single-molecule recovery after photobleaching), revealed that steady-state eisosomes are in fact highly dynamic. The specific pattern of binding and unbinding of Pil1p subunits was consistent with a biophysical model of the eisosome as a dynamic oligomeric filament. Such a model had not been previously considered for this structure but is well-established for other biophysical systems and can explain both the bulk stability and the dynamic remodeling. Although eisosomes are not directly involved in CME, the core structure is composed of a BAR-domain containing protein which binds the membrane in a curvature-sensitive and curvature-inducing manner. I expect these results will inform the yeast cell biology field, encouraging new investigations of eisosomes, and will also inform studies of other BAR-domain containing proteins, which are well-conserved and found in membrane-remodeling processes across eukaryotes.

2.1 Introduction

Molecular assemblies can have highly heterogeneous dynamics within the cell, but the limitations of conventional fluorescence microscopy can mask nanometer-scale features. Here I perform single-molecule recovery after photobleaching (SRAP) within dense macromolecular assemblies to reveal and characterize binding and unbinding dynamics within such assemblies. I applied this method to study the eisosome, a stable assembly of BAR-domain proteins on the cytoplasmic face of the plasma membrane in fungi. By fluorescently labeling only a small fraction of cellular Pil1p, the main eisosome BAR-domain protein in fission yeast, I visualized whole eisosomes and, after photobleaching, localized recruitment of new Pil1p molecules with ~30-nm precision. Comparing the data to computer simulations, I show that Pil1p exchange occurs specifically at eisosome ends and not along their core, supporting a new model of the eisosome as a dynamic filament. This result is the first direct observation of any BAR-domain protein dynamics *in vivo* under physiological conditions consistent with the oligomeric filaments reported from *in vitro* experiments.

The eisosome is a multimolecular assembly on the cytoplasmic face of the plasma membranes of fungi, a structure similar to caveolae in mammals. It consists of a stable assembly of proteins clustered on a small invagination of membrane (Malinska *et al.*, 2003; Walther *et al.*, 2006; Strádalová *et al.*, 2009; Douglas and Konopka, 2014), whose various functions in cell membrane organization and lipid regulation remain questions of study (Aguilar *et al.*, 2010; Frohlich *et al.*, 2014; Kabeche *et al.*, 2015a; Kabeche *et al.*, 2015b). Fission yeast eisosomes are highly stable, linear domains (50 nm wide and 1–2 μm long), whereas budding yeast eisosomes appear as diffraction-limited puncta. The

main protein component of the eisosome, Pil1p in fission yeast, contains a Bin/amphiphysin/Rvs (BAR) domain, which facilitates its organization *in vivo* (Olivera-Couto et al., 2011; Ziolkowska et al., 2011) and its oligomerization into filaments *in vitro* (Kabeche *et al.*, 2011; Karotki *et al.*, 2011), features conserved in budding yeast Pil1. Other BAR-domain proteins, common throughout eukaryotes, play critical roles in membrane-remodeling events and similarly form filaments *in vitro*, but the extent of oligomerization in cells remains unclear (Suetsugu, 2016). Because Pil1p is closely related in structure to the classical N-BAR protein endophilin (Ziolkowska *et al.*, 2011) and the fission yeast eisosome is highly stable and observable up to micrometer lengths, it provides an interesting model to study BAR domain oligomerization dynamics in live cells.

Methods such as fluorescence recovery after photobleaching (FRAP) have been invaluable for characterizing cellular organization and dynamics at the micrometer scale. However, detecting spatial heterogeneities at the nanometer scale and dynamics within multimolecular assemblies in cells is still challenging. In physiological conditions, eisosomes are essentially immobile and exhibit no dynamics in FRAP experiments on time scales up to 20 min (Walther *et al.*, 2006; Kabeche *et al.*, 2011), and are therefore considered to be static microdomains.

Here I demonstrate a strategy to monitor nanometer-scale single-molecule dynamics within dense macromolecular assemblies in live cells, which we call single-molecule recovery after photobleaching (SRAP). By labeling only a small fraction of Pil1p molecules, I visualized whole eisosomes, and after photobleaching, I observed isolated Pil1p molecules binding to existing eisosomes. This strategy allows us to

measure with high precision the positions and the on- and off-rates of dynamic Pil1p molecules in eisosomes in live cells. I show that binding and exchange of Pil1p occurs specifically at the ends of eisosomes and not along the filament body. By comparing data with computer simulations, I reject simple models of the eisosome as a static or uniformly dynamic microdomain and show that the data support a model of the eisosome as a dynamic filament. This result is, to our knowledge, the first report of a BAR-domain protein as a membrane-bound oligomeric filament in normal cellular conditions. I expect that these studies of the eisosome will enable further insights into BAR protein oligomerization and function in other organisms.

2.2 Results and Discussion

2.2.1 Quantitative analysis of number of Pil1p molecules and density at eisosomes

I used quantitative microscopy (Wu and Pollard, 2005; Wu *et al.*, 2008) of live fission yeast to directly determine the cellular concentration of Pil1p as well as the local density of Pil1p at eisosomes in cells for the first time. By comparing the fluorescence intensity of cells expressing Pil1p fused to monomeric enhanced green fluorescent protein (mEGFP) to a calibrated standard strain expressing Fim1p-mEGFP, I determined the total expression of Pil1p-mEGFP to be 619,000 ± 60,300 molecules/cell, or 38.2 ± 3.7 μM global concentration (mean ± SD across six images, 150 cells). This result is comparable to that reported by mass spectrometry experiments (Carpy *et al.*, 2014), confirming that Pil1p is one of the most highly expressed proteins in fission yeast. In addition, I determined the cytoplasmic concentration of Pil1p-mEGFP to be 22.8 ± 4.7 μM; ~40% of the total protein is bound to the membranes in eisosomes.

The local density of Pil1p-mEGFP at eisosomes is 2890 ± 680 molecules/μm along the linear eisosome axis, or approximately seven dimers per 5 nm of length, remarkably consistent with the lattice dimensions of *in vitro*-reconstituted filaments (Karotki *et al.*, 2011). Assuming a hemicylindrical geometry as seen in electron micrographs, this corresponds to a surface density of 28,700 ± 6700 Pil1p dimers/μm^2, or a membrane surface area of ~35 nm^2 per Pil1p dimer.

This density is similar to the theoretical close-packed limit and much higher than BAR protein scaffolds necessary to generate membrane tubules in experiments *in vitro* (Bhatia *et al.*, 2009; Sorre *et al.*, 2012; Shi and Baumgart, 2015). I interpret this remarkably high local density as evidence that the lattice organization of Pil1p in filaments observed *in vitro* indeed also exists in eisosomes in live cells, facilitating their high stability through extensive protein–protein interactions.

2.2.2 Single-molecule recovery after photobleaching of Pil1p

To determine whether any subpopulations within eisosomes are dynamic, I devised a general strategy called SRAP that extends concepts from other microscopy methods, such as TOCCSL (Brameshuber and Schutz, 2012), sptPALM (Manley *et al.*, 2008), and single-molecule speckle microscopy (Danuser and Waterman-Storer, 2006; Yamashiro *et al.*, 2014). I fluorescently label only a small fraction of a protein of interest in the cell with an organic fluorophore at sufficient density that the overall shape of the multimolecular assembly is visible. In a continuous microscopy movie under normal imaging illumination, I allow the structure to photobleach completely and then visualize reappearance of spots corresponding to single fluorescently tagged proteins recruited to dynamic regions of the multimolecular assembly.

To perform SRAP experiments in live fission yeast, I sparsely labeled Pil1p by fusing a SNAP-tag to the protein C-terminus and incubating cells with low concentration (0.5 μM) of benzylguanine-conjugated silicon-rhodamine 647 dye (SiR647; (Keppler *et al.*, 2003; Lukinavicius *et al.*, 2013; Lukinavicius *et al.*, 2015)) and then imaged cells in total internal reflection fluorescence (TIRF) microscopy. This protocol yielded sufficient density of Pil1p-SNAP labeled with SiR647 (referred to as Pil1p-SiR; typically 3–5% of cellular Pil1p-SNAP) to visualize long, linear eisosomes on the cell membrane (Figure 2.1A and Figure 2.2A). Pil1p-SiR structures were similar in shape, size, and number to structures in cells expressing Pil1p-mEGFP (Figure 2.1, F–H), and I observed very low nonspecific fluorescence (Figure 2.2B).

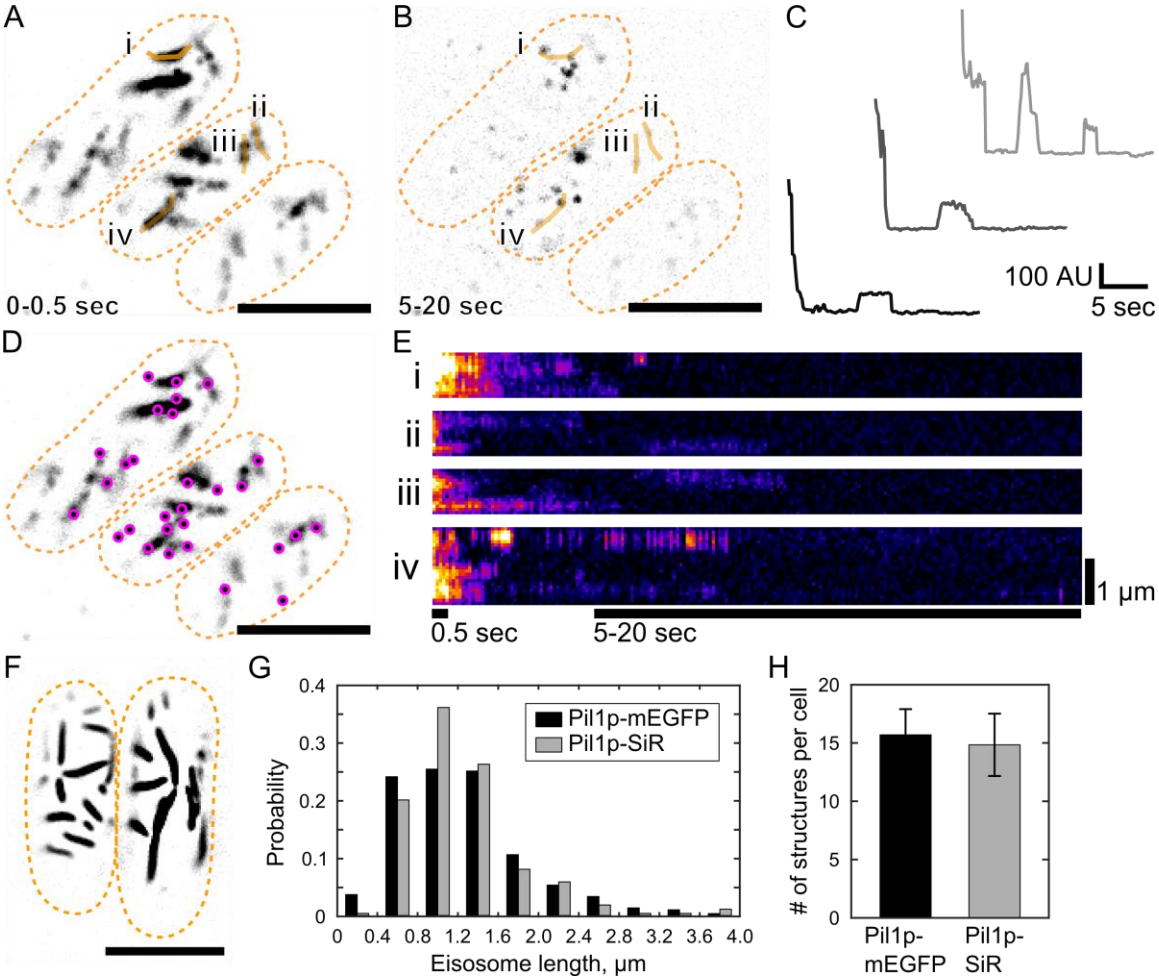

Figure 2.1 Single-molecule recovery after photobleaching of Pil1p-SiR

Cells expressing Pil1p-SNAP were labeled with SNAP-SiR647 at 0.5 µM for 15 hours, washed, and imaged in TIRF. A: Average intensity projection of the first 5 frames (0.5 seconds) of a movie reveals linear eisosomes. B: Maximum intensity projection of frames 50-200 (5 to 20 sec) of the same movie shows single molecule recovery events. Orange lines i-iv are the line traces used for the kymographs in E. C: Example intensity traces of SRAP spots show stepwise photobleaching and single-molecule recovery of Pil1p-SiR. D: The positions of single-molecule recovery events (SRAP spots, magenta) are mapped on the visible eisosomes. E: Kymographs of line traces along eisosomes (i-iv as labeled in A and B), with bars indicating the time spans for the projection images. F: Cells

expressing Pil1p-mEGFP imaged in TIRF are similar in appearance to SNAP-tag labeled cells in (A). G: Comparison of eisosome lengths measured in cells with Pil1p-mEGFP (black, 1250 +/- 650 nm for N = 304 eisosomes) or labeled Pil1p-SiR (grey, 1240 +/- 580 nm for N = 275 eisosomes) show no significant difference by two-sample Kolmogorov-Smirnov test ($p = 0.33$). H: Comparison of number of eisosome objects visible in cells expressing Pil1p-mEGFP (black, 15.7 +/- 2.2) or labeled Pil1p-SiR (grey, 14.8 +/- 2.7) shows no significant difference by two-sample Kolmogorov-Smirnov test ($p = 0.89$). A, B, D, F scale bar: 5 μm. Cell outlines are drawn in orange dashed lines. Mean +/- S.D. reported for at least 16 cells in each measurement. Reprinted from (Lacy *et al.*, 2017).

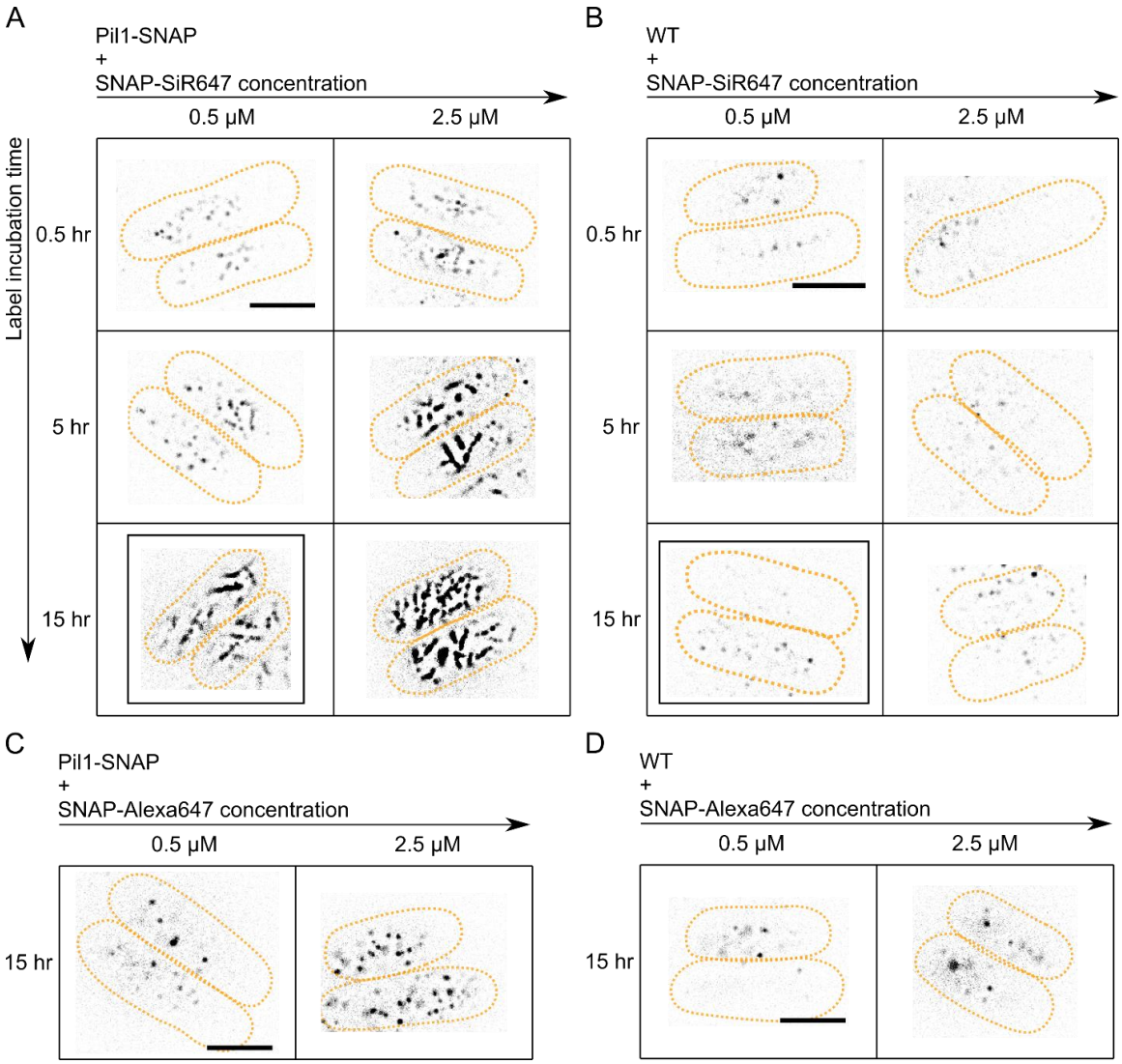

Figure 2.2 SNAP labeling of Pil1p in live fission yeast

A-B: *S. pombe* cells expressing Pil1p-SNAP (A) or wild-type cells (B) were incubated with SNAP-SiR647 at indicated concentrations in EMM5S media for various times, washed and imaged in TIRF. The boxed panel highlights the sample condition used for further imaging and analysis, 15 hours at 0.5 μM SNAP-SiR647. C-D: *S. pombe* cells expressing Pil1p-SNAP (C) or wild-type cells (D) were incubated with SNAP-Alexa647 at indicated concentrations in EMM5S media, washed and imaged in TIRF. Images shown are inverted contrast, maximum intensity projections of 20-sec movies with

median-filter background subtracted. Cell outlines are drawn in orange dash. All image panels are at same scale with scale bar 5 μm and same brightness scale. Reprinted from (Lacy *et al.*, 2017).

After ~5 s of imaging under low-power TIRF illumination (~20 W/cm^2), the fluorescently labeled eisosomes visible in the first few frames photobleached. Because TIRF imaging illuminates only molecules within ~500 nm above the coverslip, unbleached Pil1p-SiR molecules in the cytoplasm or on the membrane beyond the TIRF field may diffuse into the illumination field in later frames of the movie (Figure 2.1, A and B). Because only a small fraction of Pil1p molecules were fluorescently labeled, fluorescence reappeared as isolated spots. Intensity traces of recovery spots over the length of the movie revealed stepwise increases and decreases (Figure 2.1C) characteristic of single fluorescent molecules binding and unbinding or photobleaching. Although it is conceivable that fluorophore blinking could also give rise to recovery events, such events would appear uniformly along the eisosome. My observation that recovery is localized at eisosome ends implies that the fraction of recovery events due to blinking is negligible, a conclusion supported by the fact that SiR647 has been shown to be very stable and usually requires high laser intensity or additives to enhance blinking (Uno *et al.*, 2014).

In addition, SRAP spots at the sites of eisosomes were immobile, suggesting that they were not freely diffusing on the membrane surface and indeed corresponded to fluorescent Pil1p-SiR incorporated into eisosomes. My SRAP method revealed that new Pil1p molecules bind at eisosomes within a few seconds after initial photobleaching of the labeled structure.

2.2.3 Pil1p recruitment is not uniformly distributed

Further inspection of the recovery events suggested that eisosome ends are hot spots of Pil1p exchange (Figure 2.1D). Kymographs of lines drawn along eisosomes

showed that fluorescence signal at eisosome ends persisted longer and recovered after photobleaching more frequently than along the interior (Figure 2.1E). To calculate precisely the distance of SRAP spots to the eisosome end, I determined the position of each spot with super-resolution localization and determined the position of each eisosome end by fitting a sigmoidal curve to the intensity profile of the eisosome end extracted from initial frames (see Appendix and Figure 2.3A). I found that 92% of SRAP spots were within 250 nm from their corresponding eisosome end, with an average position of 97 ± 119 nm (mean ± SD, 191 spots in 20 cells; Figure 2.3B).

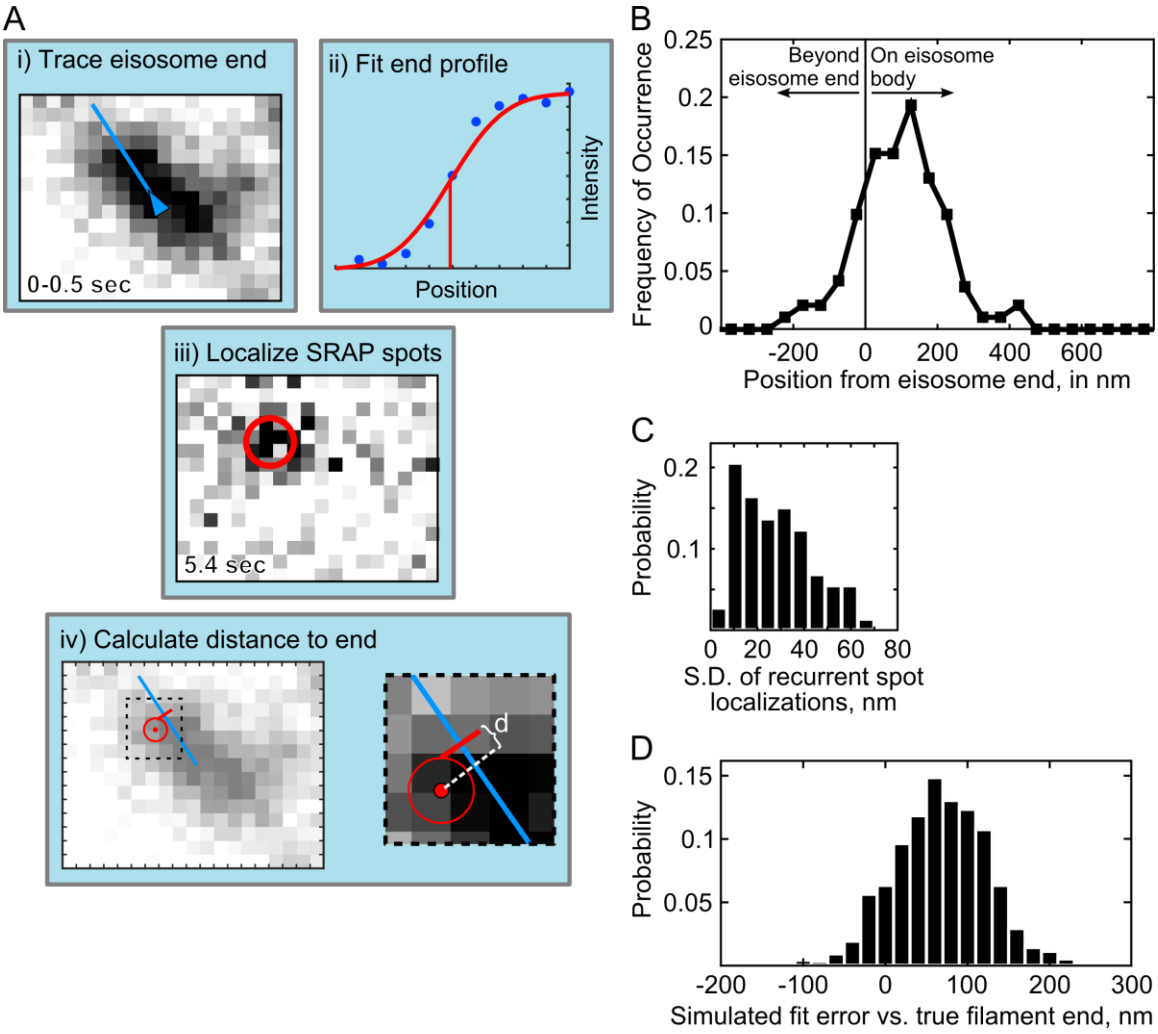

Figure 2.3 Image analysis for localization of SRAP spots at eisosomes

A: Schematic of the measurement of distance to eisosome end: (i) The end of an eisosome is traced in the average projection of the first 5 frames (0-0.5 sec); (ii) the line intensity profile at the eisosome end is fitted to determine the position of the diffraction-limited end (red line); (iii) a SRAP spot position is determined with the PeakFit plugin for ImageJ in the movie frame when it appeared, and super-resolution localizations from multiple frames are averaged to calculate the position of the SRAP event; (iv) the distance *d* is calculated from the SRAP spot along the eisosome line trace to the end; in i, iii, and iv, one image pixel is 70 nm. B: Measured SRAP spot positions relative to the

eisosome end, average 97 +/- 119 nm S.D. (N = 191 spot/filament pairs across 20 cells). C: Spot localization precision is determined as standard deviation calculated for each SRAP spot that included multiple localizations in time, average 27.9 +/- 15.9 nm S.D. (N = 73 sets). D: Errors in fitting of simulated sparsely labeled, dynamic eisosome ends. Mock eisosome end intensity profiles (as in A.ii) were generated according to a 3% labeling efficiency, with three extra emitters added to the end position and fitted as described in Appendix 1.1. Average difference between the fitted end position and the simulated true end is 67.8 +/- 56 nm S.D. (N = 1000 simulations). Reprinted from (Lacy *et al.*, 2017).

To more clearly interpret this distribution of positions, I simulated data sets based on hypothetical models for Pil1p dynamics, including any possible sources of experimental noise or errors. In a first model (referred to as the uniform model), I assumed that binding events occur uniformly along the eisosome (Figure 2.4, blue). The simulations included noise terms to mimic the uncertainty in the localizations for spots and eisosome ends (Figure 2.3, C and D, and Figure 2.5) and took into account the observed distribution of eisosome lengths (Figure 2.1G). The simulated positions were broadly distributed, with an average position of 346 ± 254 nm, clearly disagreeing with the SRAP data (Figure 2.4).

In a second model (referred to as the end model), I assumed that binding of new Pil1p occurs only at eisosome ends, as in a dynamic oligomeric filament (like actin monomers polymerizing into a filament). The simulated distribution followed a shape more similar to the experimental data but with a mean position of 0 ± 67 nm (Figure 2.4, dashed magenta). The slight offset of the SRAP spot localizations toward the interior of the eisosome (97 ± 119 nm) seems to contradict a model of dynamics strictly confined to the end. This shift cannot be explained by the spot localization precision, as the SD of recurrent localizations at a given SRAP site was 27.9 ± 15.9 nm (Figure 2.3C). I wondered whether the offset could be explained by the accuracy of localization of eisosome ends and whether a dynamic end could introduce a systematic bias.

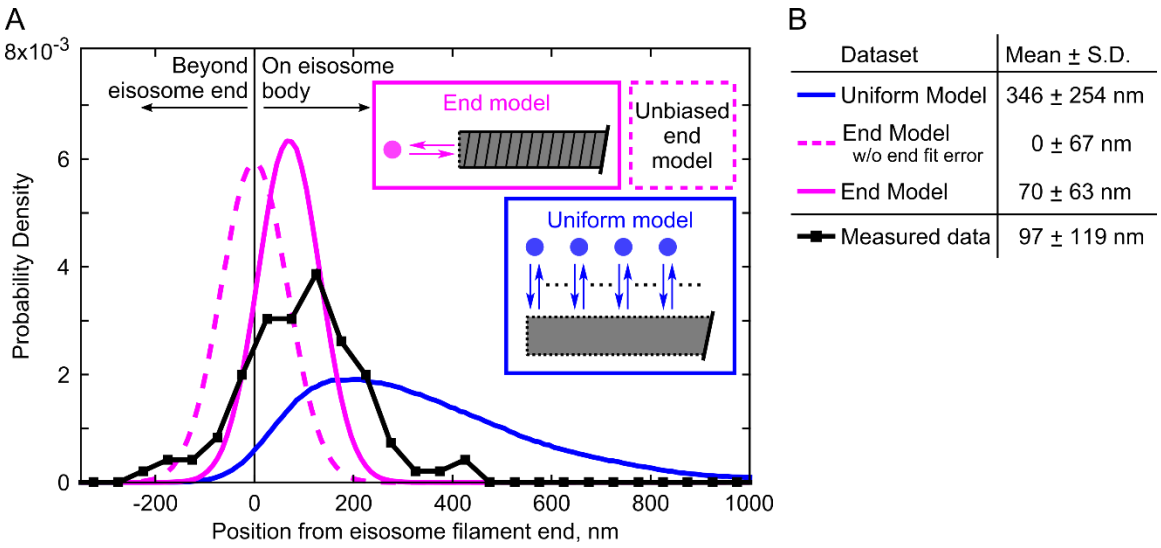

Figure 2.4 Single-molecule recovery of Pil1p-SiR occurs at eisosome filament ends

A: Probability distributions of measured distances (black squares, N = 191 spot/filament pairs across 20 cells) and simulation results (uniform dynamics model, blue; end dynamics model, dashed magenta, N = 275,000 runs for each tested model). The simulation models are illustrated in schematic form. For the end model simulations, the dashed line represents simulations using an unbiased Gaussian noise distribution for eisosome end localizations, and the solid line represents simulations using the true noise predicted from fitting a dynamic end (as in Figure 2.3D). B: Table of mean and standard deviation of distributions for simulated datasets and measured SRAP spots. Reprinted from (Lacy *et al.*, 2017).

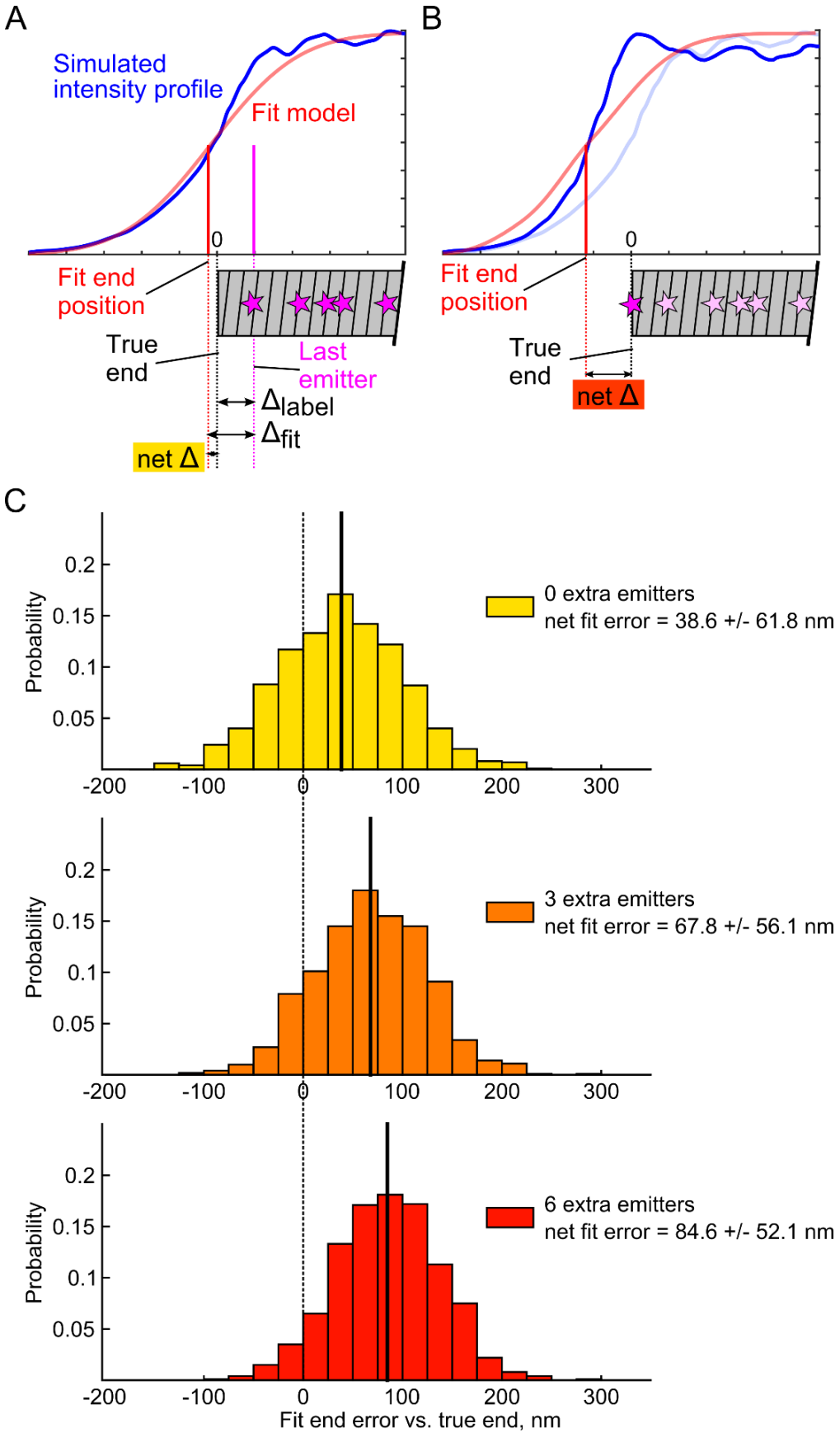
A
Simulated intensity profile
Fit model
0
Fit end position
True end
Last emitter
Δlabel
Δfit
net Δ
B
0
Fit end position
True end
net Δ
C
Probability
0.2
0.15
0.1
0.05
-200
-100
0
100
200
300
0 extra emitters
net fit error = 38.6 +/- 61.8 nm
3 extra emitters
net fit error = 67.8 +/- 56.1 nm
6 extra emitters
net fit error = 84.6 +/- 52.1 nm
Fit end error vs. true end, nm

Figure 2.5 Characterization of errors in simulated eisosome end localizations due to sparse labeling

A: Schematic of errors in fitting: mock fluorescence intensity traces (blue) were generated by simulating a number of emitters uniformly distributed on a 350-nm region and then fit with the error function model (red line). Δ_{label}, distance between the last emitter (closest to the eisosome end) and the eisosome end; Δ_{fit}, distance between the eisosome end position estimated by fitting the fluorescence intensity and the last emitter; Δ_{net}, difference between the eisosome end position estimated by fitting the fluorescence intensity and the true end position. B: Recruitment of new fluorescent molecules only at the filament ends introduces a systematic error in fitting. Mock fluorescence intensity traces (blue) were generated by simulating a number of emitters in a 350-nm region with one or more additional emitters at the eisosome end, and then fit with the error function model (red). Δ_{label} is reduced to zero and the intensity profile is skewed beyond the true eisosome end position. C: Distributions of the differences between the fitted end and the true end (Δ_{net}) for simulated eisosome traces according to 3% labeling fraction with zero (yellow, 38.6 + 61.8 nm), three (orange, 67.8 + 56.1 nm), or six (red, 84.6 + 52.1 nm) extra emitters added to the eisosome end (N = 1,000 simulations for each case). For each plotted distribution, the mean is shown as a black line, with the true end position shown as black dashed line. In all plots, the sign of Δ is given as the effect on the calculated spot position (estimating the end to be past the true structure causes the calculated SRAP spot position to be shifted toward the filament interior, a positive value).

2.2.4 Localization accuracy of sparsely labeled, dynamic eisosome ends

I evaluated the accuracy of the eisosome-end localizations by fitting simulated data mimicking linear filaments labeled with low density, similar to the experimental data (Figure 2.5A). First, I found that fitting the intensity profile with an error function – a model that assumes a continuous distribution of emitters – overestimates the end position beyond the true position by a significant distance, depending on the number of fluorophores present. In simulations corresponding to 3% labeling efficiency, the average error of the fitted eisosome-end position is 38.6 ± 61.8 nm (Figure 2.5C).

However, because I extracted intensity profiles from an image averaged over a short time, if Pil1p recruitment is actually localized to the eisosome end, then any new labeled molecules that bind during the recording time would skew the intensity profile toward the end (Figure 2.5B). Indeed, in kymographs of sparsely labeled eisosomes (Figure 2.1E), the signal at eisosome ends persisted longer than the signal along the eisosome body, likely due to additional Pil1p-SiR molecules binding before the initial labeled molecules have photobleached. I simulated this effect by adding extra emitters at the true end position before fitting the intensity profile. Simulations with three or six extra emitters (numbers as expected based on estimates of Pil1p binding rate; see later discussion) resulted in net fitting errors of 67.8 ± 56.1 or 84.6 ± 52.1 nm, respectively (Figure 2.3D and Figure 2.5C), mirroring the offset in the measured SRAP spot positions.

2.2.5 Eisosome ends are specific sites of single-molecule recovery events

I repeated simulations of the end model for Pil1p-SiR recovery incorporating this biased localization error for the eisosome end. Based on the more conservative bias estimated from simulations of three extra fluorophores in the initial fluorescence trace,

the result resembled the SRAP data (70 ± 63 nm; Figure 2.4, solid magenta). Importantly, the only assumption of this model is that the eisosome end is the specific site of Pil1p binding; the bias in the eisosome-end localization arises from the sparse labeling of the sample.

As a putative alternative hypothesis, I considered a model in which Pil1p binding occurs on a "ragged end" or a dynamic region at the eisosome end rather than a flat end. Simulations of a ragged end model using various sizes for the dynamic region showed that a 125-nm region at the eisosome end was necessary to produce a result similar to the SRAP data (97 ± 76 nm; Figure 2.6). However, a ragged or tapered filament end is difficult to quantify from electron micrographs (Karotki *et al.*, 2011) but might span only a few nanometers – not sufficient to cause the distribution of localizations I observed experimentally. In addition, the SD of recurrent localizations at the same SRAP site (27.9 ± 15.9 nm; Figure 2.3C) indicated that binding events occur at a fixed position on each eisosome, in contradiction with a large dynamic region. I conclude that the measured distribution of SRAP data is consistent with Pil1p binding only at the ends of eisosome filaments, but the sparse labeling introduces a slight error in conventional fluorescence image-fitting models.

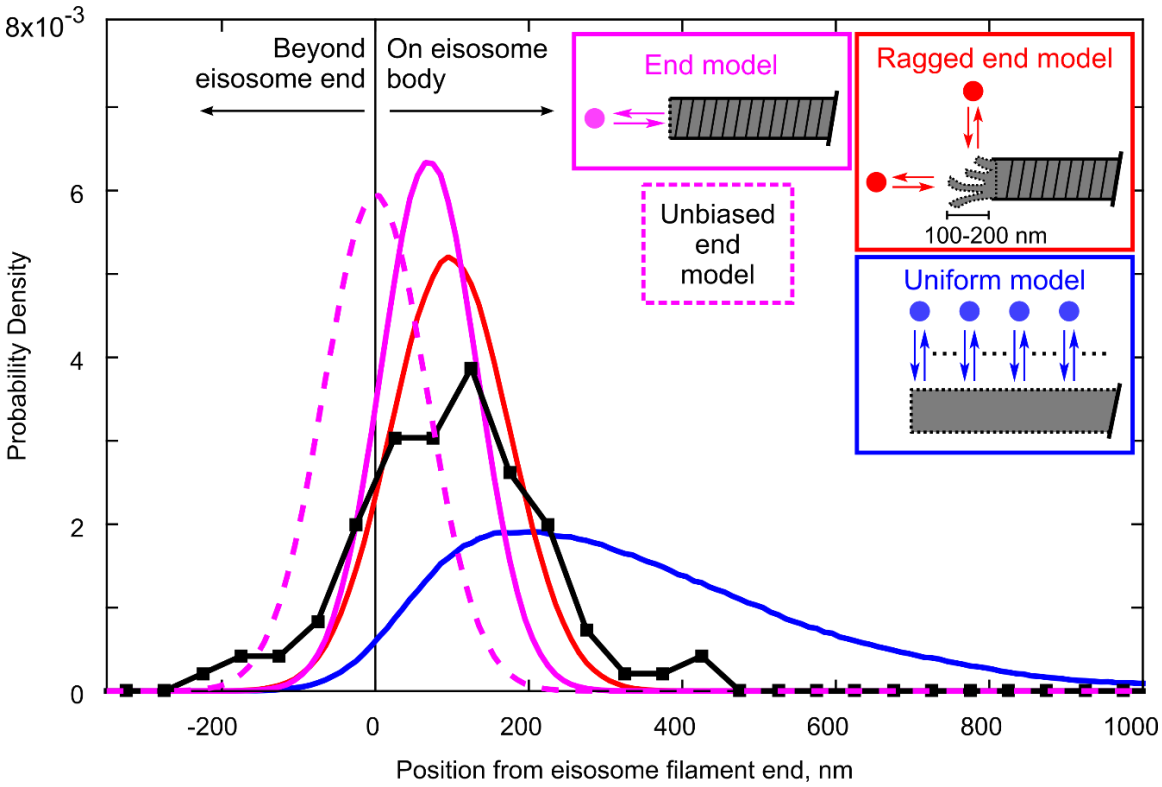

Figure 2.6 Alternate models for eisosome recovery dynamics

Probability distributions of measured distances (black squares, N = 191 spot/filament pairs across 20 cells) and simulation results (similar to Figure 2.4, N = 275,000 runs for each tested model). An additional "ragged end" model is shown (red), where simulations used simple Gaussian noise for the eisosome end position and calculated spot positions uniformly distributed within a discrete zone at the eisosome end. Simulated end model with biased end error (solid magenta) and unbiased end error (dashed magenta), uniform model (blue), and measured dataset (black) are as shown in Figure 2.4. Several values for the ragged end model zone were tested (not shown) to find an average position of 97 $\pm$ 76 nm for a 125-nm zone, similar to the measured data (97 $\pm$ 119 nm).

2.2.6 Characterization of Pil1p kinetics using SRAP data

In addition to localization, a variety of other single-molecule analyses can be applied to SRAP spots, such as lifetimes analysis to determine rates of binding and unbinding. I first measured the lifetimes of SRAP spots and fitted the distribution with an exponential curve to determine an off-rate. The apparent off-rate, 2.4 ± 0.2 sec^{-1}, was much faster than the overall rate of photobleaching in the images, 0.48 ± 0.03 sec^{-1} (fitted value ± 95% confidence intervals; Figure 2.7A), suggesting that Pil1p-SiR molecules are not only photobleaching but also unbinding from the eisosomes. By subtracting the photobleaching rate from the spots' disappearance rate, I estimate the unbinding rate of Pil1p to be 2.0 ± 0.2 sec^{-1}, consistent with the findings of (Olivera-Couto *et al.*, 2015).

I then measured the distribution of wait times between SRAP events to determine the apparent binding rate of Pil1p-SiR to an eisosome end (Figure 2.7B). Assuming mass-action kinetics, the distribution can be fitted to a single exponential. I noticed that the spot localization algorithm caused the bins for very short wait times (< 0.4 sec) to be artificially overpopulated because it occasionally missed a localization for a spot that actually persisted over many frames. I excluded these bins and fitted the distribution of wait times between binding events with an exponential curve; I found an apparent on-rate of 1.2 ± 0.2 sec^{-1} (Figure 2.7B). This apparent on-rate is the product of a binding rate constant and the concentration of Pil1p-SiR (0.9 μM, i.e., the product of the labeling efficiency, 4%, and the cytoplasmic Pil1p concentration, 22.8 μM). Therefore, the binding rate constant for Pil1p binding to the end of an eisosome is 1.3 ± 0.9 μM^{-1} sec^{-1}. I used single-exponential fits for binding and unbinding because we did not expect multiple populations of different rates, such as in a polar filament with unique kinetics at

each end. Pil1p exists primarily as a symmetric dimer, which would result in a filament with no polarity (Karotki *et al.*, 2011; Olivera-Couto *et al.*, 2011), and indeed I observed a number of filaments with Pil1p recruitment at both ends (Figure 2.1D). Taken together, these data indicate that Pil1p is undergoing fast single-molecule exchange at eisosome ends, even in the absence of large-scale eisosome remodeling.

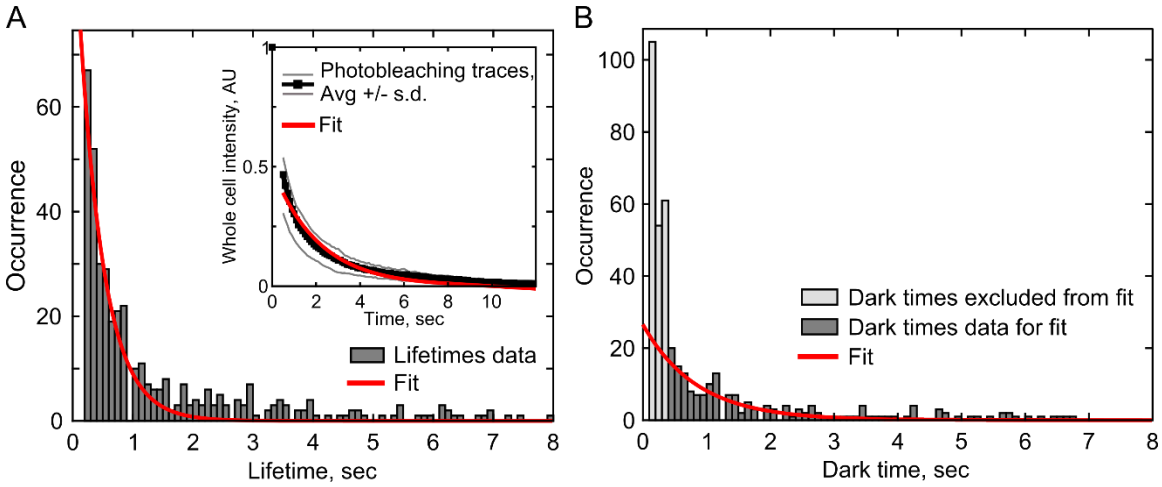

Figure 2.7 Analysis of Pil1p unbinding and binding kinetics

A: The distribution of SRAP spot lifetimes (dark grey, N = 433 events) was fit with a single exponential decay (red line) to determine the apparent off-rate of SRAP spots, -2.4 +/- 0.2 sec^{-1}. Inset: Photobleaching of whole cells. Ten curves of normalized whole-cell intensity were averaged (black, gray lines +/- 1 S.D.), and the average curve (starting at frame 5) was fit with a single exponential (red line) to determine the photobleaching rate, -0.48 +/- 0.03 sec^{-1}. To determine Pil1p-SiR unbinding rate at eisosomes, the photobleaching rate was subtracted from the total off-rate, resulting in an unbinding rate 2.0 +/- 0.2 sec^{-1}. B: The distribution of dark times between SRAP spot appearances (dark grey, N = 189) was fit with a single exponential decay (red line) to determine the apparent binding rate of Pil1p-SiR, 1.2 +/- 0.2 sec^{-1}. The very short dark times ($t < 0.4$ sec, light grey) were excluded as mostly artifacts of missed localizations causing artificial blinks. Fitted rate parameters are given with 95% confidence intervals. Reprinted from (Lacy *et al.*, 2017).

2.2.7 SRAP reveals heterogeneities at the nanometer scale in vivo

Pil1p exchange at the eisosome has previously been unobservable using conventional imaging approaches. FRAP experiments (Walther *et al.*, 2006; Kabeche *et al.*, 2011) were unable to observe this dynamic subpopulation because detecting single fluorescent proteins is challenging when fully labeled structures are imaged in the same frame. One study using fluorescence fluctuation techniques detected a subpopulation of Pil1 oligomers exchanging between the cytoplasm and plasma membrane (Olivera-Couto *et al.*, 2015), but this method lacked the spatial resolution to determine the precise location and role of dynamic molecules relative to the nanoscale structure of the eisosome.

My SRAP method was critical for revealing the behavior of individual protein molecules in the context of the larger eisosome structure. I expect that the SRAP method will be easily and broadly applicable to reveal localized single-molecule dynamics and heterogeneities within other multimolecular assemblies because it requires only sparse labeling and a TIRF microscope with single-molecule detection capabilities. Although similar sparse fluorescence conditions might be achieved by partial photobleaching of the sample (Brameshuber and Schutz, 2012) or photoswitching of fluorescent proteins (Manley *et al.*, 2008), the SRAP protocol has several advantages over existing methods. This approach avoids high-intensity laser illumination required for FRAP methods, which can be damaging to cells. I use organic fluorophores that are brighter and more photostable than fluorescent proteins, enabling better localization precision. By using a single fluorophore to characterize both the initial structure and the recovery dynamics, I avoid challenges of multichannel imaging and alignment. Importantly, I demonstrated

that sparse labeling is sufficient to determine the overall shape of a macromolecular assembly but may require a minor adjustment from conventional fluorescence image-fitting models. Future applications of SRAP imaging for large cellular assemblies should consider this factor when modeling a structure of interest.

2.2.8 Filament model for the eisosome

My results demonstrate that the eisosome is highly dynamic, with continuous and fast exchange of Pil1p at its ends, even in the absence of perturbation. Models of the eisosome as a membrane microdomain (Walther *et al.*, 2006; Kabeche *et al.*, 2011; Karotki *et al.*, 2011) would predict Pil1p exchange to occur uniformly around its edges. Instead, my data support a new model for the eisosome as a membrane-bound filament with a stable body and dynamic ends (Figure 2.8).

Pil1p and other BAR-domain proteins have been observed to oligomerize and form filaments and membrane tubules *in vitro*, but it has been unclear to what extent this oligomerization exists *in vivo* or whether instead BAR proteins are loosely clustered on patches of curved membranes (Adam *et al.*, 2015; Daum *et al.*, 2016; McDonald and Gould, 2016; Suetsugu, 2016). Recent *in vitro* studies of BAR proteins propose that binding at low or moderate surface density is sufficient to generate membrane tubes (Simunovic *et al.*, 2016). My quantitative analysis of Pil1p-mEGFP eisosomes indicates that Pil1p exists at extremely high density, consistent with the lattice structure of filaments reconstituted *in vitro* (Karotki *et al.*, 2011). Although a polymer filament model has been previously hypothesized for eisosomes (Moseley, 2013), my results are the first experimental evidence of dynamic behavior that supports a filament model.

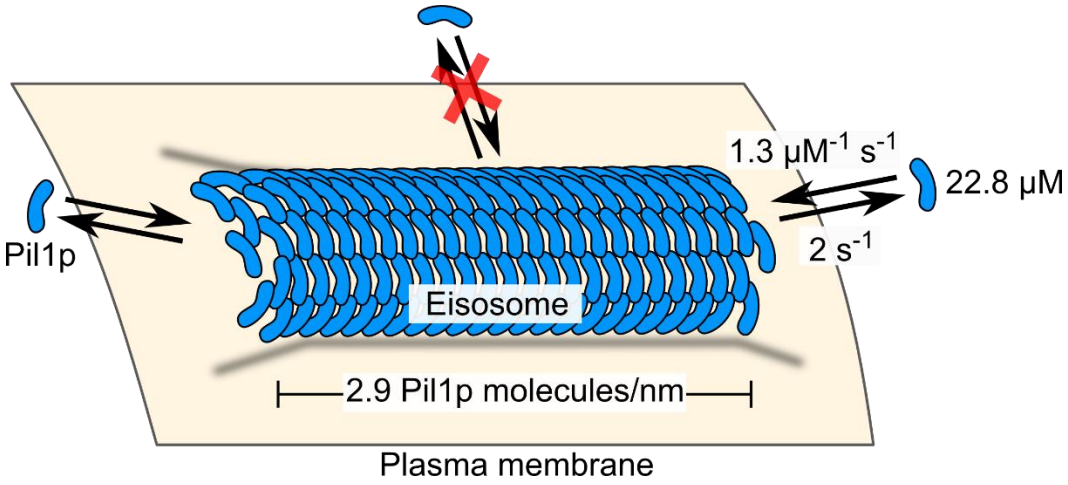

Figure 2.8 Model of the eisosome as a dynamic filament

Pil1p dimers assembled into a filament on the cytoplasmic surface of the plasma membrane are free to associate and dissociate at the ends but not at the interior. Binding and unbinding rate constants, cytoplasmic concentration of Pil1p, and density of Pil1p in the eisosome are given as reported in the text. Reprinted from (Lacy *et al.*, 2017).

Reconsidering the eisosome as a membrane-bound oligomeric filament enables several predictions and poses new questions for future investigation. Of interest, electron micrographs of eisosomes in cells show that the membrane adopts a hemicylindrical furrow instead of a full tube as observed *in vitro* (Karotki *et al.*, 2011). The physical or biochemical means by which a hemicylindrical scaffold of proteins is stabilized remain open questions, but my results clearly indicate that the filament body and long edge do not provide suitable binding sites for new Pil1p molecules.

The measured rate constants predict a net growth of eisosome filaments of ~28 Pil1p molecules/s, or ~0.6 μm/min. This high rate of polymerization is surprising, considering that eisosomes grow very slowly throughout the cell cycle, ~1 μm/h, and I do not observe large distances between successive Pil1p-SiR spots (Figure 2.3C). A likely reason for this discrepancy is that some eisosome ends might be capped, limiting the number of actively polymerizing filaments in the cell at any time. Indeed, I observed that ~70% of filament ends did not have any SRAP events over the 15-s movies. If instead, all ends were active, this proportion would be far smaller, equal to:

$$P(t) = \exp(-k_{bind} * [Pil1p\text{-}SiR] * t)$$

$$= \exp(-1.3\ \mu M^{-1} sec^{-1} * [4\% * 22.8\ \mu M\ ] * 15\ sec) = 1.9 * 10^{-8}$$

where P(*t*) is the probability of observing a wait time of length *t*, k_{bind} is the binding rate constant, and [*Pil1p-SiR*] is the concentration of free Pil1p-SiR available.

Importantly, a filament model predicts that rapid eisosome remodeling could occur in response to physical or biochemical cues by simply modulating the rates of Pil1p binding and/or unbinding to achieve polymerization or depolymerization, just like other cytoskeletal filaments such as actin and microtubules (Gardner *et al.*, 2011; Pollard,

2016). One recent study found that in yeast cells lacking a cell wall, eisosomes rapidly disassemble in response to high osmotic stress, within minutes (Kabeche *et al.*, 2015a), which could easily occur for a dynamically regulated filament.

2.3 Conclusions

A precise physical understanding of the eisosome not only will improve our knowledge of the cell biology and stress responses of fungi and pathogens, but it will also add to our understanding of BAR-domain protein assemblies in other organisms. I expect that filament-like oligomerization may be a feature of other BAR-domain proteins, even in diffraction-limited clusters or transient complexes, which have been difficult to study using conventional microscopy approaches in cells. As demonstrated here, the methodology of sparse labeling and single-molecule localization after photobleaching should be valuable for studying other cellular systems where researchers want to uncover the dynamics of individual molecules within the context of a larger multi-molecular assembly.

3 Single-molecule turnover dynamics during endocytosis

In this chapter I apply a sparse fluorescent labeling strategy similar to the method described in Chapter 2 and (Lacy *et al.*, 2017), to explore single-molecule behavior during clathrin-mediated endocytosis (CME). Analysis of actin and actin-binding proteins will determine if their residence times reflect disassembly and turnover of the actin meshwork. Similarly, turnover dynamics of other proteins such as clathrin will reveal fundamental details of the membrane coat. My experiments provide the first direct experimental evidence for turnover dynamics in the CME actin meshwork, supporting predicted mechanisms for force production to achieve membrane remodeling.

3.1 Background and motivation

The core protein machinery in CME is well-conserved from yeast to mammals and the recruitment of endocytic proteins is highly reproducible (Sirotkin *et al.*, 2010; Boettner *et al.*, 2011; Taylor *et al.*, 2011). As discussed in Chapter 1, a complex machinery of over 60 different proteins is assembled and disassembled in about 20 seconds to deform the flat plasma membrane into a 50-nm vesicle (Figure 1.1), including a dynamic meshwork of actin filaments and actin-associated proteins. Many observations have led researchers to propose that the actin meshwork generates the force required to invaginate the membrane, overcoming the high turgor pressure in yeast cells or other sources of high membrane tension (Aghamohammadzadeh and Ayscough, 2009; Boulant *et al.*, 2011; Collins *et al.*, 2011), but the detailed mechanisms of force production have been debated.

3.1.1 Predicted turnover dynamics in CME

Quantitative microscopy studies indicate the endocytic actin meshwork contains about 100-200 filaments (Sirotkin *et al.*, 2010; Berro and Pollard, 2014a; Picco *et al.*, 2015), but only a few filaments are actively polymerizing at any time. Theoretical calculations estimate that the amount of force needed to invaginate the membrane during CME is in the range of 1000 to 3000 pN (Carlsson and Bayly, 2014; Dmitrieff and Nedelec, 2015; Tweten *et al.*, 2017), which would require an unrealistically high amount of force per filament. The architecture and force-production mechanisms of the endocytic actin meshwork are thought to be similar to other force-generating actin systems such as lamellipodia (Theriot and Mitchison, 1991; Pollard and Borisy, 2003), where a highly dynamic and rapidly turned-over meshwork is capable of generating much more force than simple polymerization. We hypothesized that turnover of proteins – i.e. continuous polymerization and disassembly of actin filaments – underlies the observed dynamics in CME, generating more force than simple estimates based on the number of polymerizing filaments. Although similar turnover dynamics have been observed in large actin structures like lamellipodia (Watanabe and Mitchison, 2002), this mechanism has not been directly observed in CME because conventional microscopy tools lack the resolution to measure such behavior.

Fluorescence recovery after photobleaching (FRAP) experiments have shown that the polymerizing actin meshwork moves away from the membrane at a rate of 45 nm/sec (Kaksonen *et al.*, 2003; Kaksonen *et al.*, 2006) – promising evidence that the endocytic actin meshwork (which spans a distance of around 150-250 nm (Kukulski *et al.*, 2012)) turns over multiple times during the patch lifetime (Goode *et al.*, 2015). However,

interpretation of turnover rates by FRAP experiments is complicated because the total number of proteins in CME sites is rapidly changing and many new molecules are recruited during the time of observation – even if there were no exchange of molecules, new labeled molecules would still be recruited after bleaching, so the observation of recruitment after photobleaching is not necessarily indicative of true turnover, or unbinding and exchange. *In vitro* single-molecule studies of actin associated proteins have also been invaluable for measuring binding and unbinding rates and exploring mechanisms (Kuhn and Pollard, 2007; Smith *et al.*, 2014; Bombardier *et al.*, 2015; Jansen *et al.*, 2015), but it is difficult to reconstitute the full complexity of competition and interplay of all the actin-regulatory proteins in CME.

3.1.2 Super-resolution and single-molecule microscopy

Fluorescence microscopy has long been a valuable tool for studying molecular assemblies in live cells but the detection of discrete objects is fundamentally limited by the wavelength of light used for observation – fluorescent molecules separated by distances smaller than ~250 nm are impossible to distinguish. The advent of single-molecule localization microscopy (SMLM) and other super-resolution techniques has enabled a revolution in studying biological systems at high resolution (Sahl *et al.*, 2017). If the fluorescent emitters are isolated in space or time, each diffraction-limited image records only a few emitters and the spots in it can be fitted to precisely determine their positions. This separation of fluorescent molecules can be achieved by dilution (easily achieved *in vitro* with purified proteins) or by manipulating the fluorophores, as in the two most commonly used SMLM techniques: stochastic optical reconstruction microscopy (STORM), in which chemical fluorophores are induced to randomly blink on

and off (Rust *et al.*, 2006); and photoactivation localization microscopy (PALM), in which a subset of fluorophores (usually activatable fluorescent proteins) are triggered to switch on by an activation laser (Betzig *et al.*, 2006; Hess *et al.*, 2006).

By collecting a long series of images where each spot is attributed to a single fluorescent molecule and different subsets of molecules are emitting in each frame, the total set of positions can be used to reconstruct the underlying structure. In these SMLM-based methods, the positions of fluorescent molecules can be determined with theoretically unlimited precision, routinely enabling resolution of features in the 20-50 nm range with typical microscope hardware (Sahl *et al.*, 2017). Although STORM and PALM provide valuable structural information at the nanometer scale, they do not provide information about the dynamics of the labeled proteins because individual molecules' positions are recorded at a brief point in time.

Another valuable application of SMLM is single-molecule tracking. Instead of rapidly switching molecules on and off as in PALM or STORM, isolated fluorescent molecules can be monitored to extract the positions of the same molecule over time. A wide variety of behaviors can be assessed by analyzing these trajectories, such as the diffusion or directed motion of molecules, binding and unbinding kinetics, and more (Yu, 2016). Actin and other cytoskeletal systems have been important targets of study for techniques such as single-molecule speckle microscopy (SiMS (Watanabe and Mitchison, 2002; Yamashiro *et al.*, 2014)) or single-particle tracking PALM (sptPALM (Manley *et al.*, 2008)). In both of these methods, a small subset of the protein of interest (e.g. actin monomer) is made visible (through photoactivation or chemical labeling of a small fraction of the proteins in the cell), and then imaged under conditions that enable tracking

of the sparse molecules over time. However, these techniques have usually been applied to large cellular structures like the lamellipodia and focal adhesions (Smith *et al.*, 2013; Yamashiro *et al.*, 2014) or other systems where molecules are present for many seconds and trajectories might span hundreds of nanometers.

Nanometer-scale observation of actin dynamics in CME in live cells has remained elusive. Techniques like SiMS and sptPALM have not been applied to CME because the structure is so small and its composition changes so rapidly. Super-resolution imaging of CME sites has given increasingly detailed structural organization (Mund *et al.*, 2017; Sochacki *et al.*, 2017; Arasada *et al.*, 2018), but these techniques are not yet able to quantify the dynamics of molecules in the site. Inferences from mathematical modeling and *in vitro* experiments have been useful but there are clear limitations and added complexity in live cells.

In this chapter, I present data on single-molecule dynamics within endocytic patches obtained by recording trajectories of sparsely labeled actin and other CME proteins, similar to methods like SiMS (Watanabe and Mitchison, 2002; Yamashiro *et al.*, 2014) and following protocols related to those demonstrated in Chapter 2 and (Lacy *et al.*, 2017). These experiments provide the first direct experimental evidence for the turnover underlying the actin force production and membrane remodeling in CME.

3.2 Results and Discussion: Single-molecule turnover in CME

Previous quantitative fluorescence microscopy studies have discussed "lifetimes" of endocytic patches, or the total time that a fluorescently tagged protein is visible at a site. Here, I refer to the lifetimes of single-molecule tracks, representing the "residence times" of individual molecules within these patches in contrast to the patch lifetimes.

Proteins with short single-molecule residence times compared to their previously measured patch lifetimes are said to undergo fast turnover.

3.2.1 Characterization of single-molecule tracking methods

In my previous experiments with Pil1p (Chapter 2 and (Lacy *et al.*, 2017)), specific labeling could be confirmed visually by the characteristic shape of eisosomes. In CME however, the structures of interest are diffraction-limited puncta (as seen in Fim1p-mEGFP images in Figure 3.1A), and I aim to have only one or zero fluorescent molecules in any single CME patch, so it was important to determine that single-fluorophore spots observed in the sparse labeled SNAP-tag samples indeed correspond to CME sites. After the sparse labeling of Fim1p-SNAP with SNAP-conjugated silicon-rhodamine 647 (referred to as Fim1p-SiR, as in Chapter 2 and (Lacy *et al.*, 2017)), only a few spots are visible in each cell (4.2 +/- 0.5 spots per cell, Figure 3.1B,E). To also confirm that any fluorescent spots visible at the cell membrane were due to specific labeling of the SNAP-tag fusion protein and not from non-specific accumulation of the free fluorophore, I prepared samples of wild-type cells, which express no SNAP-tag protein, using the same labeling and washing protocols and analyzed these movies with the same spot localization and tracking parameters as in later experiments. As seen in Figure 3.1C, there is no detectable fluorescence in wild-type cells, and any cell autofluorescence or background signal in the images leads to near-zero contribution of track data (2 tracks detected in five analyzed images containing 591 cells, Figure 3.1E).

To assess what fraction of Fim1p-SiR spots represent true endocytic sites, I recorded two-color images of cells co-expressing Fim1p-SNAP and Acp2p-mEGFP (which localizes to CME patches) labeled with SNAP-SiR (Figure 3.1D). Automated

colocalization analysis of the merged image is difficult because the Acp2p-mEGFP signal often overlaps in crowded regions of the cell (such as the cell tips), and because patches are at various stages of endocytosis so their intensities vary, but comparison of spots visible in the SiR channel with signal in the GFP channel indicate that at least 95% of SiR spots coincide with endocytic patches. At the start of the movie, around four Fim1p-SiR spots per cell are visible (Figure 3.1E), or about 35% of endocytic patches that would be visible. To avoid the possibility of multiple SNAP-SiR molecules in the same endocytic patch or multiple spots overlapping in crowded regions of the cell, the initial frames (0.5 sec) of each movie were discarded before tracking analysis, so that typically 2 to 3 molecules are visible per cell at any single time.

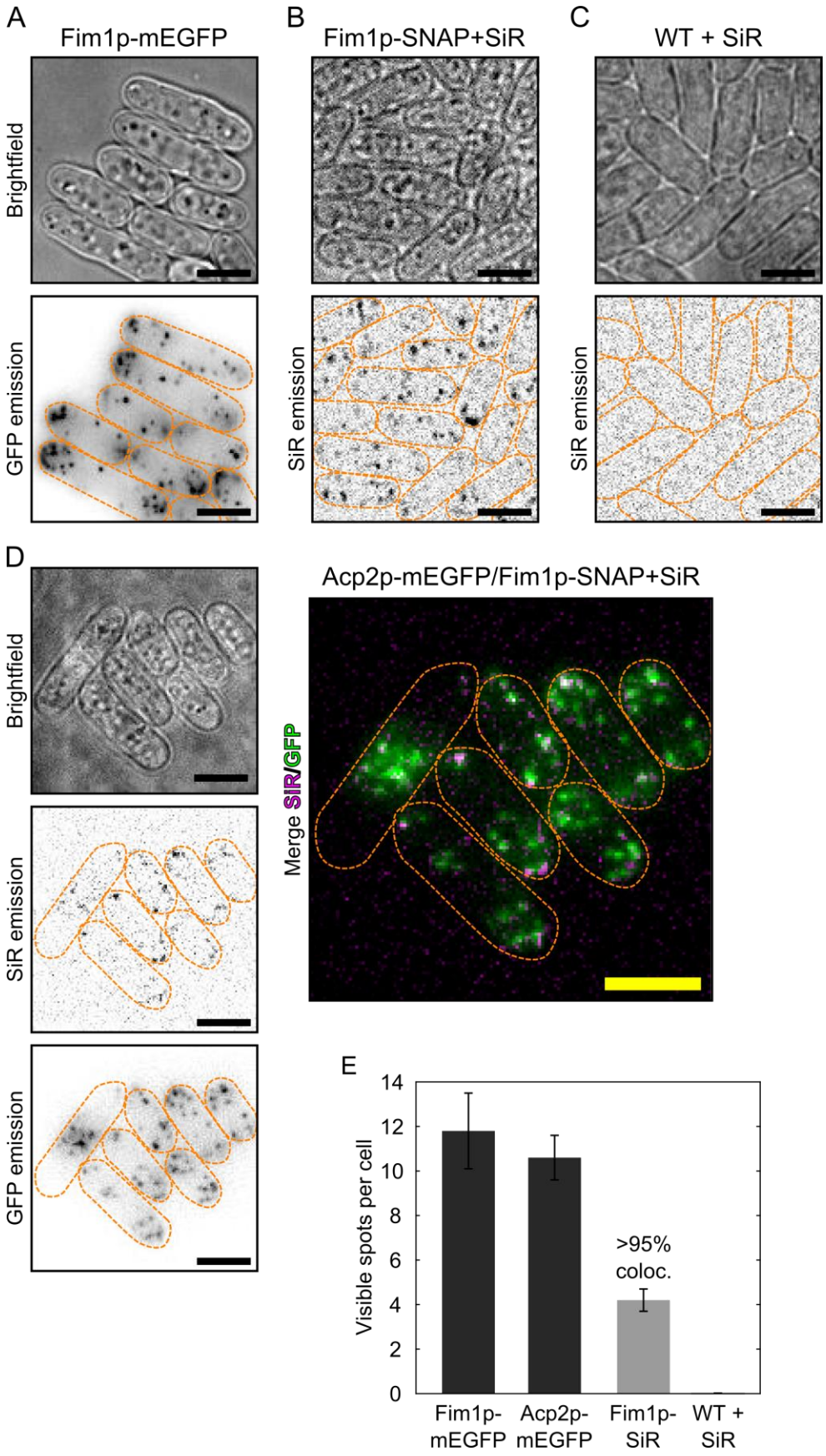
A
Fim1p-mEGFP
B
Fim1p-SNAP+SiR
C
WT + SiR
Brightfield
GFP emission
SiR emission
SiR emission
D
Acp2p-mEGFP/Fim1p-SNAP+SiR
Brightfield
SiR emission
GFP emission
Merge SiR/GFP
E
Visible spots per cell
14
12
10
8
6
4
2
0
>95%
coloc.
Fim1p-
mEGFP
Acp2p-
mEGFP
Fim1p-
SiR
WT +
SiR

Figure 3.1 Characterization of SNAP-tag single-molecule tracking

A: *S. pombe* cells expressing Fim1p-mEGFP imaged in TIRF with 488 nm excitation (upper: bright-field image, lower: GFP emission). B-C: Fim1p-SNAP cells (B) and wild-type cells (C) incubated with 1 µM SNAP-SiR overnight and imaged in TIRF with 642 nm excitation (upper: bright-field image, lower: SiR emission). D: Cells co-expressing Fim1p-SNAP and Acp2p-mEGFP were labeled with 1 µM SNAP-SiR overnight and imaged in bright-field (upper left), SiR channel (middle left), GFP channel (lower left), and overlaid (right) to assess colocalization of single-molecule Fim1p-SiR spots with endocytic patches. E: Average number of visible spots of Fim1p-mEGFP (as in A), Acp2p-mEGFP (as in D) or Fim1p-SiR (as in B and D), and wild-type cells (as in C). At least 3 images were analyzed for each sample, manually counting spots in 50 to 60 cells; for wild-type cells five images containing 591 cells were analyzed with spot localization and tracking thresholds as described in the text. Cell outlines are drawn in orange dash for fluorescence images. Scale bars for A-D are 5 µm.

We anticipated that disappearance of a fluorescent molecule could be attributed either to dissociation of the labeled protein (as it diffuses into the cytoplasm it leaves the illumination field and the focal plane) or to destruction of the fluorophore by photobleaching. To determine the rate of photobleaching in the imaging conditions, I recorded images at two different laser powers, (measured as 1.2 and 2.1 W/cm^2 exiting the microscope objective). The total number of fluorescent spots decreases over time, following an exponential curve (Figure 3.2A), as expected because photobleaching is a single-step kinetic process. The rate of photobleaching is proportional to the intensity of illumination (Song *et al.*, 1995), and comparison of representative SiR tracking sets at two laser powers shows reasonably good agreement with this expectation (1.75-fold change in laser power, ~1.9-fold change in bleaching rate). In addition, the rate of bleaching at low laser power is slow enough (~0.1 sec^{-1}, or average lifetime of 10 sec) that I expect to be able to measure the relevant lifetimes of single molecules recruited to endocytic patches.

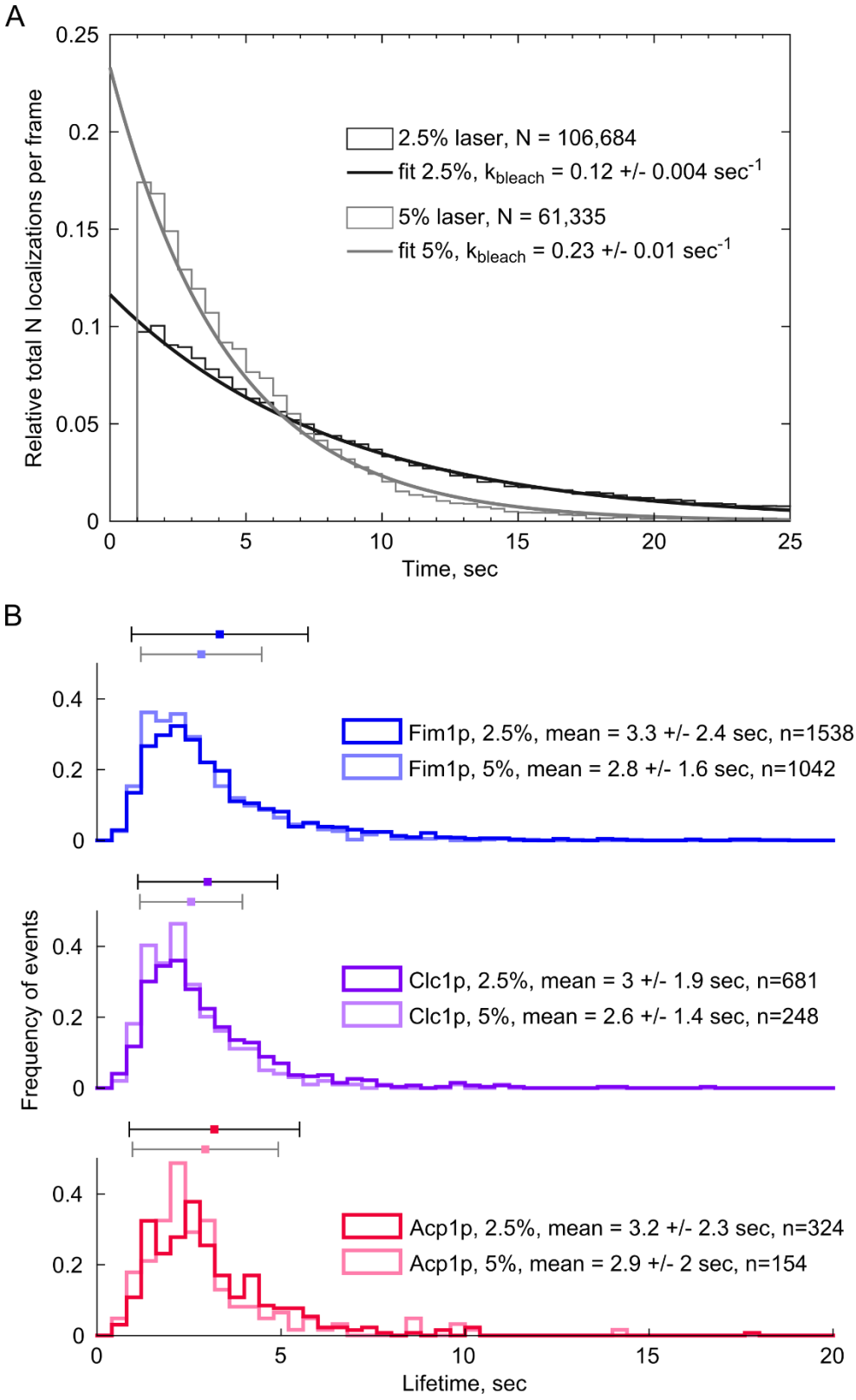

Figure 3.2 Effect of photobleaching on tracking SiR-labeled proteins

A: The number of spots across all movies decreases over time due to photobleaching of SiR. Fim1p-SiR samples were imaged at two laser powers (dark and light gray as 2.5% and 5%, measured as 1.2 and 2.1 W/cm^2, for 49 and 14 images, respectively). The total number of spots per frame is plotted and fit with an exponential decay, excluding early time bins which are under-populated due to image crowding or high background signal. The rates are given for the two fitted curves, 0.12 +/- 0.004 sec^{-1} and 0.23 +/- 0.01 sec^{-1}. B: Track lifetimes for three proteins (Fim1p-SiR, Clc1p-SiR, and Acp2p-SiR), from images recorded at 2.5% and 5% laser power (dark and light curves, respectively). Each dataset is taken from a single set of three or more images recorded in the same sample. The points and error bars above each distribution show the mean and standard deviation, and number of tracks are given in the legends for each plot.

3.2.2 Lifetimes of actin-bound proteins are limited by actin filament lifetime

I recorded single-molecule trajectories for eleven SNAP-tag fusion proteins sparsely labeled with SiR-SNAP (Figure 3.3). Somewhat surprisingly, for all of the proteins measured here, the lifetimes data do not follow exponential distributions (as would be expected if the rate-limiting step is a one-step unbinding event). Instead they display peaked distributions with exponential tails, resembling Gamma distributions. The proteins generally have residence times around 3 seconds (overall, 25% of tracks are less than 1.8 sec, and 25% are greater than 3.8 sec), much faster than the overall patch lifetimes of actin proteins (~20 sec) (Sirotkin *et al.*, 2010). The shapes of these distributions suggest multi-step pathways (Floyd *et al.*, 2010), but the data do not fit well to simple models of multi-step pathways with shared rate constants, making quantitative interpretation difficult. The shapes may be similar to actin monomer lifetimes in models of polymerization and disassembly (Roland *et al.*, 2008). Many actin-associated proteins display lifetime distributions similar to actin (Act1p), suggesting that their lifetime is dictated by the lifetime of the actin monomer or segment of filament they are bound to.

These residence times are also substantially shorter than the estimated photobleaching rates, and imaging at two-fold higher laser power results in only a small decrease in average lifetime (1.9-fold increase in bleaching rate yields 10% decrease in tracks mean lifetime, Figure 3.2). These two observations suggest that photobleaching makes only a minor contribution to the disappearance rate of SiR spots recorded under these conditions and the disappearance of signal can be attributed to protein dissociation from the endocytic patch.

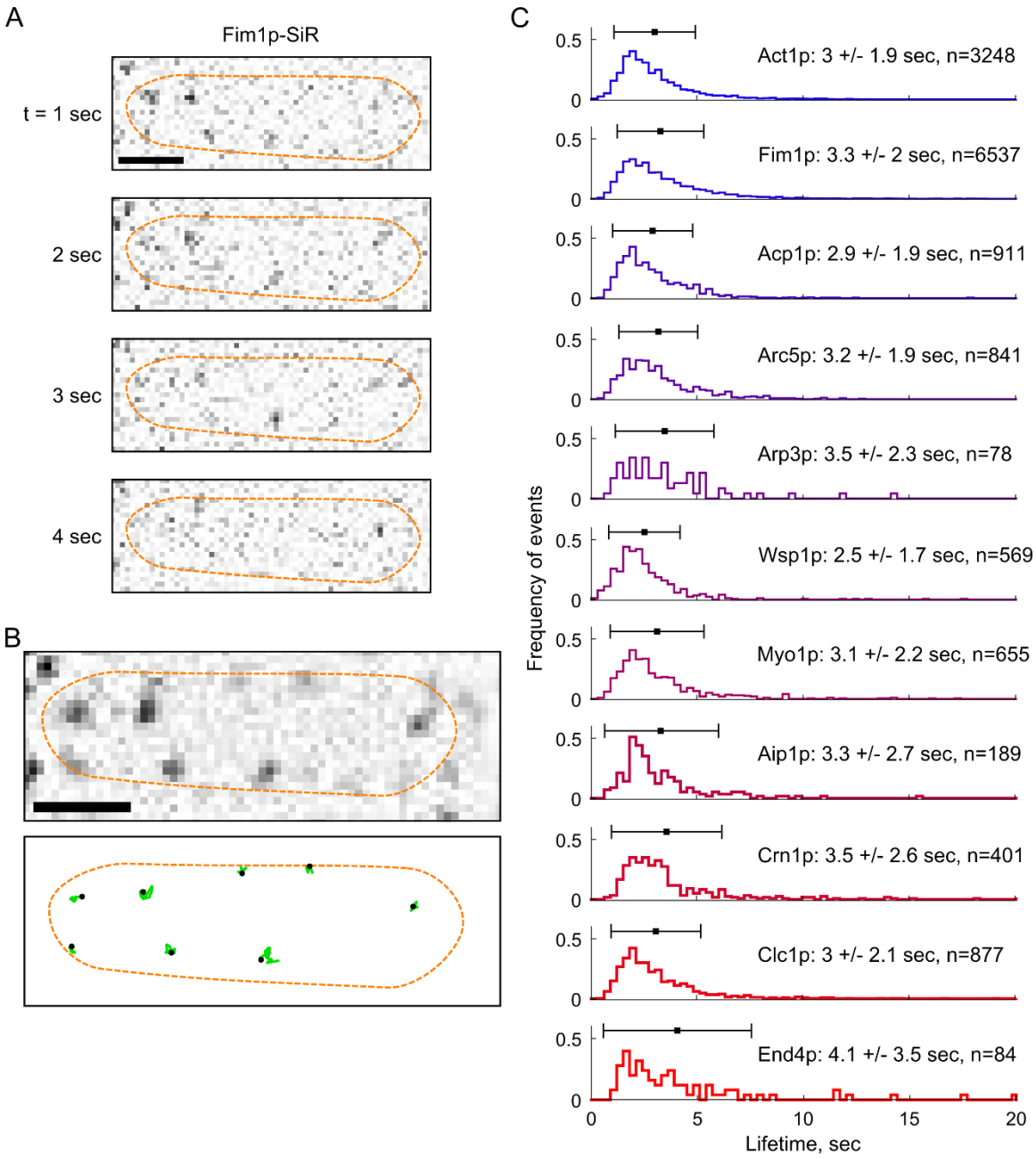

Figure 3.3 Single-molecule tracking of endocytic proteins

A: Montage of single-molecule imaging movie of Fim1p-SNAP cells sparsely labeled with SiR, showing individual frames of SiR fluorescence at the indicated times during illumination, with median-filtered background subtracted. Movies were recorded at 10 frames per second, but only individual frames are shown here. B: Sum intensity projection of the single cell region displayed in A (upper), and tracks extracted from the

movie overlaid on the cell outline (lower), drawn in green with a dot at the start position. Tracks for spots in the neighboring cells are not drawn. Cell outlines are drawn in orange dash for all fluorescence images. Scale bars are 2 μm. C: Distributions of single-molecule track lifetimes for eleven endocytic proteins of interest. Samples are labeled and the dataset statistics are given in the legends for each plot. The points and error bars above each distribution plot show the mean and standard deviation for each population.

Several notable trends and comparisons are apparent in these data. For example, actin capping protein (Acp1p) and the crosslinker fimbrin (Fim1p) have been reported to have very slow unbinding rates from actin filaments *in vitro* (Kuhn and Pollard, 2007; Skau *et al.*, 2011; Bombardier *et al.*, 2015). The good agreement of the distributions of Acp1p and Fim1p residence times with actin residence times supports the hypothesis that these proteins bind almost immediately after a new filament fragment is polymerized and they do not leave the CME site until that actin filament is disassembled. The population of rapidly diffusing monomers that never get incorporated to a filament is small or difficult to detect with my methods.

Similarly, we expected that once the Arp2/3 complex is incorporated into the meshwork as a new filament branch site, it cannot dissociate until the mother filament is severed or depolymerized. However, models of WASp-nucleated Arp2/3 branching also suggest that both a free-diffusing population and a WASp-bound population of Arp2/3 also exist at the actin patch (Berro *et al.*, 2010). It does not appear that these transient populations add to a population of Arp2/3 components Arc5p and Arp3p with significantly faster turnover than the actin filaments (Figure 3.3C). Instead, it appears that the conversion of free Arp2/3 to WASp-bound to filament-bound to branch-incorporated is highly efficient – i.e. recruitment and activation of free Arp2/3 complexes most often leads to successful branching events rather than a significant fraction of failed or rapidly released Arp2/3. The slightly longer residence times of Arc5p and Arp3p compared to actin (0.2 to 0.5 sec longer) might account for the extra time needed for these initial steps of nucleation and activation.

3.2.3 Fast lifetimes of actin-nucleation factors

Notably, the fastest turnover dynamics are displayed by Wsp1p, the actin nucleation-promoting factor (2.5 +/- 1.7 sec, Figure 3.3). It is unknown if an individual Wsp1p protein remains bound to the membrane and stays localized to a CME patch to catalyze numerous branch-nucleation events processively (Khanduja and Kuhn, 2014) or if instead the protein dissociates after a nucleation event (Berro *et al.*, 2010; Wang *et al.*, 2016). My data suggest that individual Wsp1p proteins unbind and dissociate from the CME patch relatively rapidly. Although my data cannot determine whether Wsp1p unbinding occurs after a single nucleation event or multiple events, it is clear that Wsp1p molecules exchange and turn over faster than the overall lifetime in the patch (12 sec, (Sirotkin *et al.*, 2010)).

Myo1p is variously reported to play a role in nucleation, anchoring of actin filaments to the membrane, and production of constrictive force (Jonsdottir and Li, 2004; Sun *et al.*, 2006; Sirotkin *et al.*, 2010; Arasada *et al.*, 2018). My data indicate that Myo1p does not turn over as rapidly as Wsp1p, but I cannot rule out the potential existence of multiple populations. This might be due to Myo1p's ability to directly bind both the plasma membrane and actin filaments, while Wsp1p is indirectly recruited by interactions with other proteins, which may be more transient. Further experiments would be needed to determine if Myo1p turnover is related to its motor activity or if its turnover rate is limited by actin turnover.

3.2.4 Lifetimes of actin-disassembly factors

Somewhat surprisingly, the actin-disassembly factors Aip1p and Crn1p have average lifetimes similar to actin itself. They might be expected to display shorter

lifetimes than actin if new filaments needed a significant time to age before disassembly proteins bind and catalyze rapid severing. Previous reports indicate that the ATP hydrolysis and P_i release is very fast in CME (Bryan and Rubenstein, 2005; Berro *et al.*, 2010; Ti and Pollard, 2011), suggesting that these proteins could indeed bind actin filaments rapidly after the new monomer is added and the delay time until severing/disassembly would dictate the lifetime of both the actin monomer and the severing protein. This agrees with *in vitro* studies of mouse Aip1 and coronin (yeast Crn1p) (Jansen *et al.*, 2015), which report rates of unbinding from actin filaments that are far slower than the total lifetime of the actin patch. Thus, these proteins' residence times should be dictated only by the wait time until severing or depolymerization of the actin filament segment to which they are bound.

3.2.5 Lifetimes of membrane-bound proteins

Do membrane-binding proteins assemble a stable coat or a dynamic structure? The assembly of clathrin triskelia into a hemispherical cage dictates the shape and size of the resulting vesicle (Kirchhausen *et al.*, 2014). Previous evidence from FRAP and electron microscopy studies support a model where a clathrin lattice assembles on the flat membrane then rearranges into the curved pit structure (Wu *et al.*, 2001; Wu *et al.*, 2003; Avinoam *et al.*, 2015). Such a rearrangement would require unbinding of individual triskelia, converting from a hexagonal lattice to a mixed hexagonal-pentagonal lattice. Careful FRAP experiments on individual CCPs indicated that about 60% of the clathrin exchanges and recovers during lifetime of the pit, with a recovery half-time of 2 sec during invagination (Avinoam *et al.*, 2015). However, the overall lifetime of clathrin at endocytic patches is nearly 2 minutes, with little change in the total number of molecules

during this time (Kaksonen *et al.*, 2005; Sirotkin *et al.*, 2010). Therefore, this recovery of new clathrin molecules must be balanced by unbinding.

My data support this model of clathrin coat rearrangement, demonstrating that individual molecules have residence times of about 3 seconds (Figure 3.3C). This short residence time might seem surprising compared to the long bulk lifetime of clathrin at CCPs (nearly 2 minutes), but it should also be noted that my tracking data specifically select the molecules which appear during the imaging time, excluding any spots that were present in the initial frames, as in (Lacy *et al.*, 2017) and Chapter 2. It is possible that the core of the clathrin lattice is more stable and only a subset of molecules exhibits binding and unbinding (such as those at the edge of the lattice). It is also possible that different behavior would be observed for the clathrin heavy-chain, Chc1p.

Additional membrane-binding proteins of interest include End4p (*S. cerevisiae* Sla2, mammalian Hip1), which links the tip of the CCP to the actin meshwork (Baggett *et al.*, 2003; Skruzny *et al.*, 2012). I observe End4p to have longer residence times than the actin meshwork components (Figure 3.3C), consistent with its proposed role anchoring actin filaments to the membrane. However, repeated measurements would be needed to make strong conclusions about the significance of this difference and any sub-populations of longer- or shorter-lived events.

3.2.6 Directed motion of actin meshwork and CCP proteins

In addition to turnover of actin filaments, the dendritic nucleation model also predicts retrograde flow of filaments as the meshwork exerts force against the membrane. The trajectory of a labeled actin monomer (or filament-bound protein) will indicate the direction of the force on that filament. Unlike in lamellipodia, where the actin meshwork

spans micrometer distances, the CME meshwork spans only 150-250 nm (Kukulski *et al.*, 2012), and so motions within the actin patch have been unobservable with conventional microscopy. Previous quantitative fluorescence microscopy approaches have assessed the motions of the whole CME patch as the CCP invaginates and the vesicle is released (Kaksonen *et al.*, 2003; Sirotkin *et al.*, 2010; Berro and Pollard, 2014a; Picco *et al.*, 2015), but it has been unclear whether changes in the bulk position of the patch correspond only to cohesive motions of the patch or if they mask other diffraction-limited behaviors within the patch. My sparse labeling and super-resolution localization methods are uniquely poised to assess the motion of individual actin meshwork components.

Because I am using TIRF imaging at the cell membrane, the motion of fluorescent molecules in the image plane corresponds only to the motion in the plane of the membrane, and not the inward motion along the Z axis – the axis of invagination and, supposedly, the direction of force and retrograde flow in the actin meshwork. However, I can access this lost dimension of motion by determining whether a track's intensity increases or decreases during its lifetime. TIRF illumination intensity decays exponentially with the distance from the coverslip, so the intensity of a SNAP-labeled protein spot is correlated with the fluorophore's distance from the membrane (Figure 3.4A). Although slight variations in cell position or illumination profile on the sample will cause heterogeneity and make it difficult to interpret the absolute intensity of spots, the relative changes of intensity within an individual track should be a valuable metric to infer changes in the Z position. By visual inspection, Fim1p-mEGFP patches recorded in TIRF are visible long enough to observe the fast-diffusing stage after membrane scission,

indicating that the endocytic patch remains in the TIRF illumination field throughout invagination and scission.

Inspection of individual tracks suggested a trend of decreasing intensities (Figure 3.4B). In order to assess if a protein displays a tendency to move inwards during its lifetime in the CME site, I determined whether each track's intensity was increasing or decreasing by comparing the average intensity of points in the first third of the track lifetime with those of the final third. As shown in Figure 3.4C, most of the CME meshwork components I measured do exhibit this decreasing intensity trend, likely corresponding to retrograde flow of the actin meshwork and the invagination of the CCP tip and motion of the released vesicle.

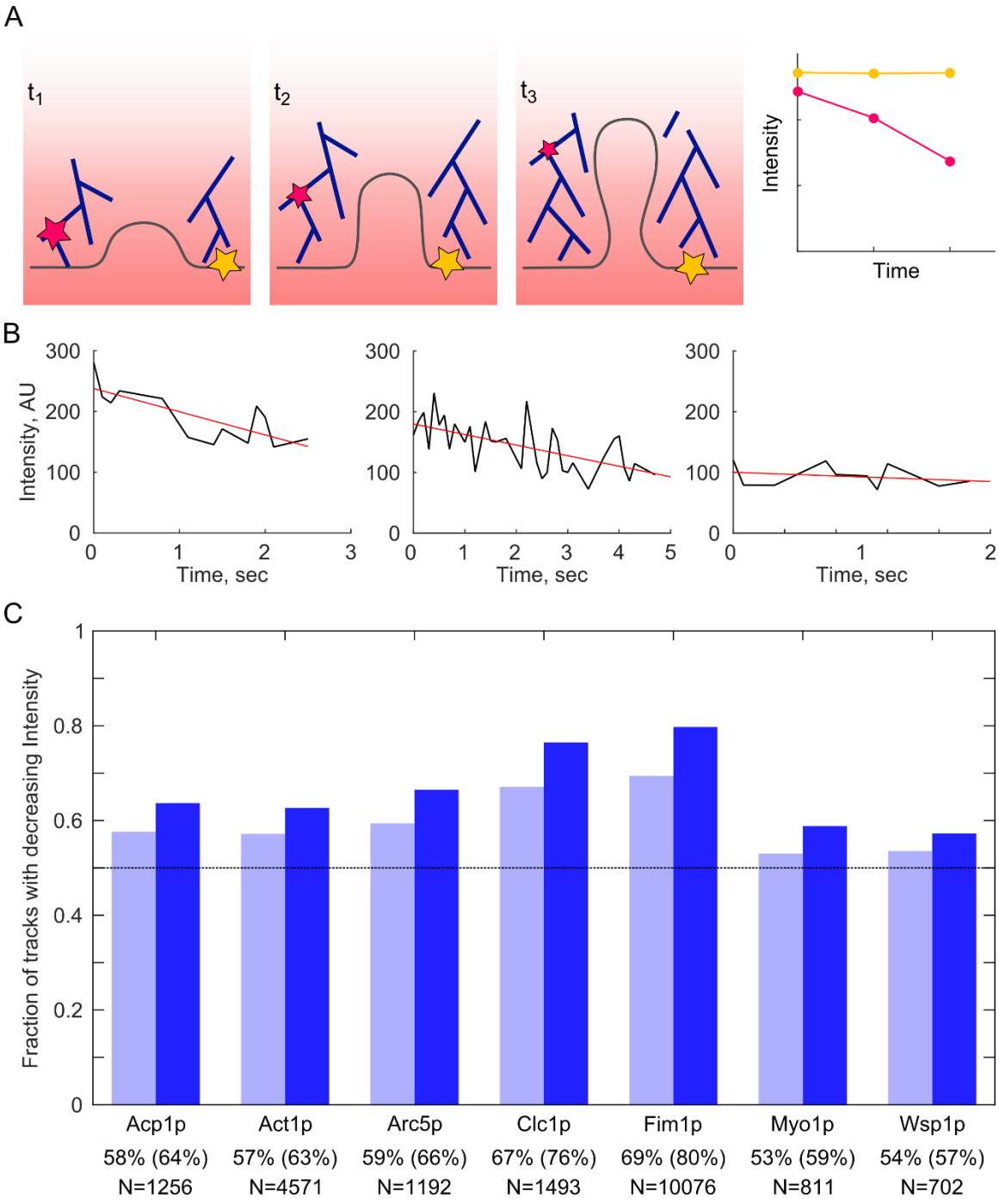

Figure 3.4 Assessing Z motion by TIRF intensity

A: Schematic showing hypothesized inward motion of actin meshwork components. Left: As a labeled molecule moves inward from the cell surface, the TIRF illumination intensity decreases, and so the detected fluorescence signal will also decrease. Right:

Hypothetical intensity traces for labeled molecules that move inward during CME (magenta) or stay at a constant depth (yellow). B: Representative intensity time traces for Fim1p-SiR tracks (black), with linear fits (red). C: Fraction of tracks that have decreasing intensity over their lifetime, calculated as described in the text. Only tracking datasets which have more than 500 tracks were used. The light blue bar is the fraction of all tracks in each dataset and the dark blue bar represents the subset of tracks longer than the median track lifetime, with the respective values given below each bar. The dashed line indicates 50%, i.e. equal probability to increase or decrease.

The strong tendency of Clc1p tracks to decay in intensity – with an even greater proportion (76%) among longer tracks – is easy to explain by the well-characterized inward motion of clathrin during invagination and eventual diffusion of the vesicle. The less pronounced decay of actin, Acp1p and Arc5p may be due to a radial expansion of the actin meshwork rather than a strictly inward motion. It is unclear why Fim1p would display a greater tendency to move inward than other actin associated proteins.

Notably, Wsp1p and Myo1p display a weak tendency of decreasing intensity. The lack of inward motion of Myo1p has been previously observed (Sirotkin *et al.*, 2010; Picco *et al.*, 2015; Arasada *et al.*, 2018), as it localizes to the base of the neck during invagination and remains on the plasma membrane after vesicle scission. However, the lack of motion for Wsp1p is surprising. Previous studies of CME patch dynamics have shown that while budding yeast WASp (Las17) does not move inward (Picco *et al.*, 2015), fission yeast Wsp1p does move inward, albeit not as far as other actin meshwork components (Sirotkin *et al.*, 2010; Arasada and Pollard, 2011; Arasada *et al.*, 2018). My results indicate that individual molecules of Wsp1p do not move inward, suggesting that perhaps the observed motion of GFP-labeled WASp is due to turnover and recruitment of new Wsp1p to new positions throughout the development of the CCP.

It should also be noted that this metric does not consider the extent of motion, only the likelihood of the direction of motion. Further analysis will be needed to refine these measurements and to quantitatively interpret the rates of motions, but these trends are a promising preliminary result.

3.2.7 Limitations and possible sources of error

It is possible that I may have missed some extremely fast events (below 0.3 sec) due to limitations in image acquisition and tracking (movies were recorded at 100 msec per frame and only tracks spanning three or more frames were counted). However, the distribution peaks are significantly higher than my limit of detection, suggesting that such fast events are rare. Previous studies have argued that binding rates are increased and unbinding rates are slow due to the high local concentration of proteins, thus it would be unlikely that a significant fraction of free diffusing molecules would enter the CME patch without binding. The current dataset does not use strong thresholds for excluding spots and tracks of lower quality, and it is possible that errors in the tracking analysis that could lead to an artificially high number of long tracks.

Importantly, several potential factors may be responsible for the observed decreasing intensity trends. Previous studies have shown that the actin patch and membrane coat proteins move inward from the plasma membrane as the CCP invaginates and the vesicle is released into the cytoplasm. My analysis here does not distinguish between motions of the whole patch or motions of individual proteins within the patch, but future analysis might be able to determine if tracks are in developing CCPs or to released vesicles based on the lateral motion or by two-color experiments with a second marker for the timing of CME.

I have not quantified the rate of motion in this analysis, but this information should be accessible within the current dataset or with new analysis of images recorded at higher laser power, which would increase the localization precision but shorten the observable lifetimes. It would be interesting to compare the single-molecule motions to

previous reports of actin meshwork motion in CME (45 nm/sec in (Kaksonen *et al.*, 2003)) or to the rates of retrograde flow in lamellipodia (30 nm/sec in (Yamashiro *et al.*, 2014)), as well as previous studies of bulk CME patch dynamics (Sirotkin *et al.*, 2010; Berro and Pollard, 2014a; Picco *et al.*, 2015).

The differences in tracking results between different proteins are usually small but are not likely to be greatly limited by contributions of noise or other artifacts in tracking. With the exception of Clc1p, Wsp1p and End4p, all of the proteins tracked here are directly incorporated into the actin meshwork, so it is reasonable to expect that they would have similar lifetimes as actin. There are differences between proteins in other behaviors, such as the intensity decay described in Figure 3.4. Note that longer tracks display even higher likelihood to move inward, which would not be the case if this behavior were due to noise or artifacts (it would revert to the mean, i.e. 50%). Although the single-molecule lifetimes of all actin meshwork components follow similar distributions, it is unclear why Fim1p tracks have a substantially higher tendency for decreasing intensity compared with other actin-associated proteins. It is probably not a likely explanation that every molecule that unbinds simply becomes dimmer as it diffuses away, as Wsp1p and Myo1p do not follow the trend of decaying intensity. Filtering localization data excludes diffusive spots from being included in tracks, and inspection of individual tracks shows that the decay in intensity is gradual rather than stepwise.

3.3 Conclusions and future work

The results presented here give the first direct experimental observation of turnover of actin and other proteins in CME. If the ~20 sec lifetime of the endocytic actin meshwork were simply the result of an accumulation phase and a disassembly phase, the

average monomer lifetime would be 10 sec. My results show actin monomers displaying an average residence time of 3 sec, suggesting that the entire CME actin meshwork turns over three times during the lifetime of the patch. This result is consistent with previous models and predictions but has never been directly observed before.

These data will require further refinement to improve the confidence of these conclusions, and additional experiments will be necessary to dissect the mechanisms of actin turnover in CME. Careful calibration of the camera and re-analysis of the images will allow more stringent thresholding for spot identification and linking, improving the precision of localizations and reducing the potential for false spots or false linking events. Repeated measurements to collect larger datasets (especially for low copy-number proteins) will improve the statistical confidence of comparisons across samples and will enable closer investigation of the possible sub-populations within the distributions.

Future experiments can use mutational or pharmacological perturbations to more clearly interpret the role of single-molecule turnover in CME. Various drugs are frequently used to stabilize F-actin (jasplakinolide), inhibit polymerization (latrunculin A or cytochalasin D), or inhibit Arp2/3 (CK-666), and deletions or semi-functional mutations in various actin machinery proteins are known to induce specific defects. Because these drugs and mutants have been previously shown to disrupt CME in measurable ways and their molecular mechanisms are well-established, single-molecule tracking of endocytic proteins in the presence of these drugs or mutants could show how the actin turnover is affected when CME fails. For example, a severing-defective cofilin mutant strain accumulates more total actin in CME patches (Chen and Pollard, 2011, 2013). I expect that single-molecule tracking in this mutant background would also

display longer single-molecule residence times of actin meshwork components, but this has not been directly shown before. Conversely, I expect mutations disrupting the binding surfaces of proteins known to mediate their recruitment would result in decreased residence time, even if the total number is unchanged or increases.

Single-molecule tracking provides a wealth of information about molecular behaviors in cells. The trajectories recorded in these experiments can be further analyzed to extract other features, such as mobility within CME sites. Future experiments can also implement two-color imaging and track alignment to separate the motions of an individual molecule within an endocytic patch from the motions of the patch itself.

In conclusion, the data presented here provide evidence for rapid single-molecule dynamics in CME faster than the previous observations of bulk patch dynamics. If the actin meshwork indeed turns over multiple times, it will be able to exert much more force than previous predictions. The short lifetimes of actin and actin-associated proteins support the hypothesis of turnover as predicted by the dendritic nucleation model of a force-generating actin meshwork.

4 Alpha-Synuclein membrane binding and membrane remodeling

Parts of this chapter are adapted from Braun AR, Lacy MM, Ducas VC, Rhoades E, Sachs JN (2014). "α-Synuclein induced membrane remodeling is driven by binding affinity, partition depth, and inter-leaflet order asymmetry." *Journal of the American Chemical Society* 136:9962-72; and Braun AR, Lacy MM, Ducas VC, Rhoades E, Sachs JN (2017). "α-Synuclein's uniquely long amphipathic helix enhances its membrane binding and remodeling capacity." *Journal of Membrane Biology* 250:183–193.

In this chapter, I investigated the membrane remodeling capacity of the N-terminal membrane-binding domain of α-synuclein (aSyn). Using fluorescence correlation spectroscopy and vesicle clearance assays, I explored the impact of the length and hydrophobicity of the amphipathic helix on membrane binding energy and tubulation of the binding energy. In addition to these experiments, our collaborators in the Sachs lab (U. Minnesota) performed coarse-grained molecular dynamics (MD) simulations to investigate the observed effects at a molecular scale, in terms of protein partition depth and lipid acyl chain disorder, interleaflet coupling and bilayer asymmetry, locally induced membrane curvature and protein organization of the membrane. These simulations were not part of my dissertation research but the published results will be referred to.

4.1 Introduction

α-Synuclein (aSyn) is a 140-amino acid, intrinsically disordered neuronal protein whose N-terminal domain (residues 1–93) adopts an amphipathic helix (AH) upon binding to lipid membranes (Figure 4.1) (Georgieva *et al.*, 2008; Jao *et al.*, 2008; Trexler and Rhoades, 2009). aSyn is the primary protein found in Lewy bodies, the protein and

lipid aggregates associated with Parkinson's disease and Lewy body dementia (Spillantini *et al.*, 1998; Gandhi and Wood, 2005; Moore *et al.*, 2005; Goedert *et al.*, 2017). It is well-established that aSyn is capable of dramatic remodeling of lipid bilayers, a behavior which is believed to play a role in the normal physiological function of aSyn, although a specific function is not known. *In vivo*, overexpression of aSyn was shown to induce mitochondrial fragmentation and fission (Kamp *et al.*, 2010; Nakamura, 2013). *In vitro* experiments have shown that aSyn induces externally protruding membrane tubules from synthetic lipid vesicles and can cause full fragmentation at high enough protein concentrations (Varkey *et al.*, 2010; Jiang *et al.*, 2013).

The N-terminal domain of aSyn is composed of seven imperfect 11-mer repeats with the KTKEGV partial consensus sequence (George *et al.*, 1995) imparting two unique characteristics. First, the imperfect nature of the 11-mer repeat introduces heterogeneity in the hydrophobic moment. In particular, the 6^{th} 11-mer of aSyn is almost entirely hydrophobic and comprises the core of the non-amyloid-β component (NAC) domain, a region of aSyn best known for its role in aggregation (Crowet *et al.*, 2007). Second, aSyn contains the longest AH in any known protein structure, spanning nearly 15 nm (Ulmer and Bax, 2005; Trexler and Rhoades, 2009; Braun *et al.*, 2012), almost 20% longer than any known AH outside the Synuclein family of proteins (Cornell and Taneva, 2006). Beta- and gamma-Synuclein contain six and seven repeats, respectively (Uversky *et al.*, 2002; Sung and Eliezer, 2006; Ducas and Rhoades, 2014).

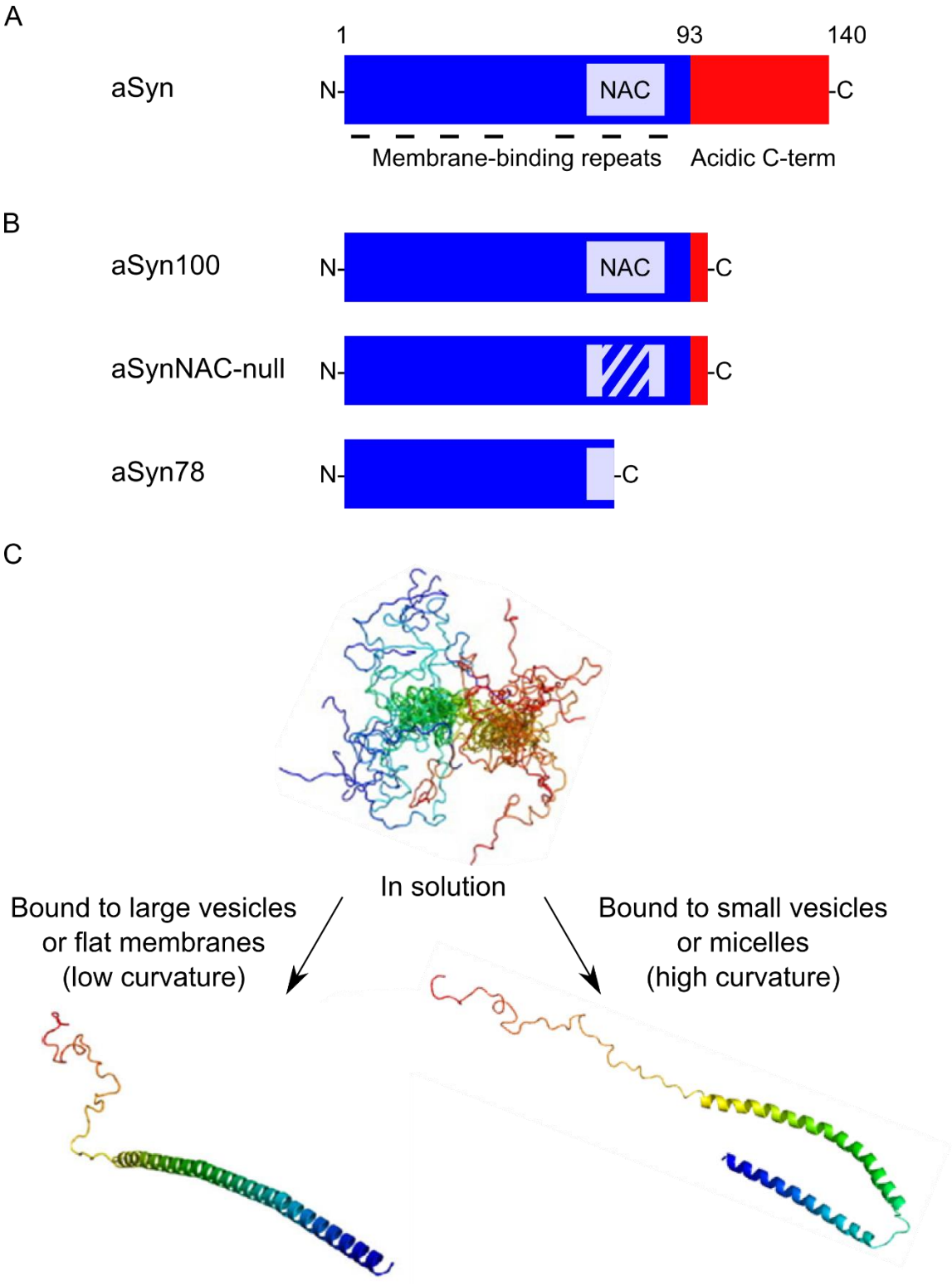

Figure 4.1 Schematic of alpha-Synuclein structure

A: Domain structure of aSyn, showing the amphipathic membrane-binding region (blue) and the acidic tail region (red). The imperfect 11-mer repeats as well as the hydrophobic non-amyloid-β component (NAC) region are indicated. B: Schematic of the modified aSyn constructs used in this study. C: Illustration of aSyn conformations in solution (disordered ensemble), extended helix bound to flat or low curvature membranes, and a horseshoe-shaped helix bound to high curvature membranes. Panel C is modified and adapted from (Nath and Rhoades, 2013).

Extensive studies have shown that amphipathic helices like that of aSyn can both sense and induce curvature upon binding a membrane, because binding requires wedging its long AH between the head groups of one leaflet of the lipid membrane to bury the hydrophobic residues (Hatzakis *et al.*, 2009; Drin and Antonny, 2010; Middleton and Rhoades, 2010; Varkey *et al.*, 2010; Cui *et al.*, 2011; Braun *et al.*, 2012; Westphal and Chandra, 2013). The 47 C-terminal residues of aSyn have a net negative charge are known to remain disordered upon binding of the AH (Chandra *et al.*, 2003; Ulmer *et al.*, 2005; Georgieva *et al.*, 2008; Jao *et al.*, 2008; Trexler and Rhoades, 2009). Proteins with bulky disordered regions can induce membrane curvature by steric crowding (Busch *et al.*, 2015) but whether the C-terminal residues of aSyn play such a role in tubulation has not been established. Similarly, a role for the hydrophobic NAC domain in tubulation has not been explored. Theory and simulations have emphasized the importance of protein insertion depth in dictating curvature induction (Zemel *et al.*, 2008) and binding energy in promoting protein organization, curvature, and membrane disruption (Simunovic *et al.*, 2013).

Due to the overall positive charge of aSyn's AH, the extent of binding to membranes, and therefore the extent to which it induces remodeling, is sensitive to the content of charged lipid headgroups. At high concentrations, aSyn causes complete tubulation and fragmentation of negatively charged giant unilamellar vesicles (GUVs) but has a negligible effect on neutral GUVs (Varkey *et al.*, 2010). This difference is attributed to a very low binding affinity of aSyn for POPC lipids (Middleton and Rhoades, 2010). Less aggressive tubulation has also been observed in vesicles with a

mixed anionic and zwitterionic lipid composition, compared with pure POPG bilayers (Varkey *et al.*, 2010; Jiang *et al.*, 2013).

Previous work in the Rhoades lab combined fluorescence correlation spectroscopy (FCS) and X-ray scattering with coarse-grained molecular dynamics simulations by the Sachs lab to show that aSyn thins membranes and induces complex curvature fields (Braun *et al.*, 2012). Other work in the Rhoades lab used FCS to investigate the preference of aSyn binding to membrane vesicles of varying size and lipid composition, showing that aSyn has stronger binding affinity to vesicles of higher curvature (smaller radius) and higher content of negatively charged phospholipids (Middleton and Rhoades, 2010).

While previous aSyn tubulation studies were done at extremely high protein concentrations, they did not account for potential differences between the K_D values for pure POPG and POPG:POPC (PG:PC) mixtures (Varkey *et al.*, 2010; Jiang *et al.*, 2013). This difference in affinity complicates the interpretation of the reduced tubulation propensity in the mixture, which could simply be attributed to a subthreshold density of protein bound to the vesicle surface. Immersing a vesicle in a protein solution results in a membrane-bound protein concentration dependent on the protein concentration in bulk and the affinity for the specific lipid membrane (Sorre *et al.*, 2012). It was therefore essential that I carry out the tubulation experiments and simulations under conditions where an equal amount of protein was bound regardless of membrane lipid composition.

I first demonstrated that the C-terminal residues of aSyn are not necessary for tubulation, showing instead that tubulation can be achieved solely by the membrane-bound AH. Second, in comparison with molecular simulations, we confirmed that the

reduction of aSyn-induced tubulation of 1:1 PG:PC bilayers compared with pure POPG bilayers can be attributed to differences in the protein's interaction with the lipid matrix (partition depth and mobility) and not dismissed as a consequence of a subthreshold density of bound protein. Third, I investigated the role of the hydrophobic NAC domain on binding affinity and tubulation by engineering an aSyn variant lacking the hydrophobic core of the domain.

Lastly, we turned our attention to the 7th 11-mer repeat, to address aSyn's unique length. I explored how residues 79–100 (this stretch includes the seventh 11-mer from the AH, an additional four helical residues, as well as seven additional unstructured residues, and carries a +1 charge) contribute to aSyn's AH binding affinity and tubulation capacity on POPG bilayer. Specifically, the presence of these 21 residues at the end of the AH influences both the binding affinity and remodeling capacity, further confirming the relationship between these behaviors.

4.2 Experimental results

4.2.1 Membrane binding characterization by FCS and CD

First, I used FCS to determine the relative affinity of aSyn100 or aSyn78 (residues 1-100 or 1-78) binding to large unilamellar vesicles (LUVs) composed of 100% POPG or 1:1 (mol/mol) PG:PC under dilute conditions. Binding of fluorescently labeled protein to unlabeled vesicles results in a shift in the autocorrelation curves to longer diffusion times (Figure 4.2A). The autocorrelation curves were fitted to determine the fraction of bound protein at varying lipid concentrations, and the dependence of bound protein on lipid concentration was fit to determine an apparent binding affinity, K_D (Figure 4.2B-E). aSyn100 binds to 100% POPG vesicles with ~60 times greater affinity than to 1:1 PG:PC

vesicles ($K_{D(aSyn100, POPG)}$ = 2.25 +/- 0.23 μM and $K_{D(aSyn100, PG:PC)}$ = 137 +/- 13 μM) in these buffer conditions. This result agrees with previous studies showing that aSyn binding to lipids is driven primarily by electrostatic interactions between anionic lipid headgroups and positively charged lysine residues in the membrane-binding region of the protein (Kjaer *et al.*, 2009; Pandey *et al.*, 2009; Middleton and Rhoades, 2010; Hellstrand *et al.*, 2013), although the complex roles of hydrophobic lipid-protein interactions and entropy cannot be ruled out. aSyn78 binding to 100% POPG vesicles has an approximately five-fold reduction in affinity compared to aSyn100 ($K_{D(aSyn78, POPG)}$ = 11.6 +/- 1.3 μM and $K_{D(aSyn100, POPG)}$ = 2.25 +/- 0.23 μM).

I also confirmed that the truncation of these fragments did not disrupt the expected transition from intrinsically disordered to alpha-helical conformation when aSyn binds to the membrane. I performed circular dichroism (CD) experiments demonstrating that both aSyn100 and aSyn78 indeed transition to alpha-helical signature upon mixing with POPG vesicles (Figure 4.3). These results agree with previous measurements of full-length aSyn (Varkey *et al.*, 2010), confirming that I am studying the AH wedge mechanism of curvature induction, rather than other mechanisms such as nonspecific protein crowding (Stachowiak *et al.*, 2010; Busch *et al.*, 2015).

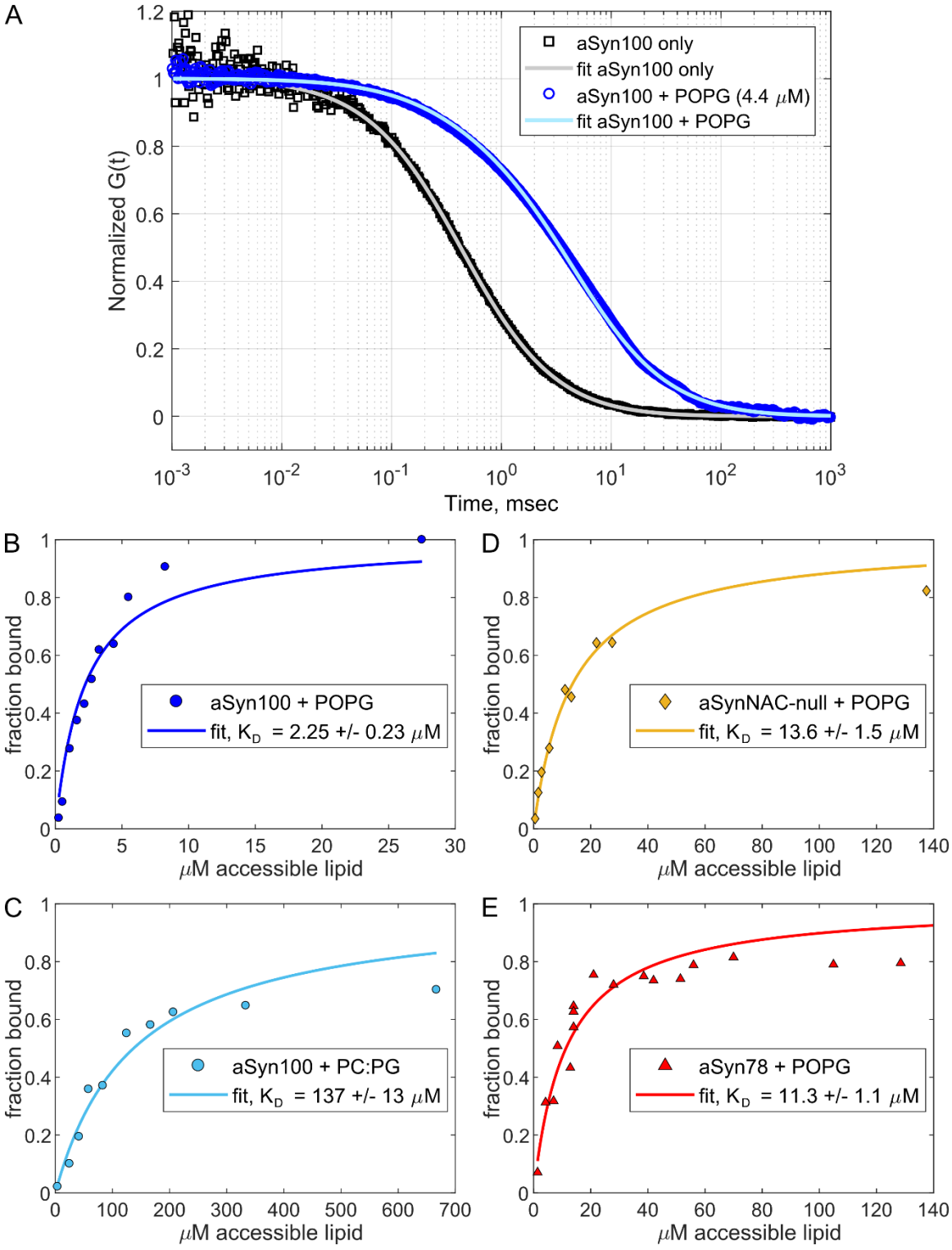

Figure 4.2 aSyn binding affinities measured by FCS

A: FCS traces for free-diffusing aSyn100 and aSyn bound to POPG (4.4 μM accessible lipid). Autocorrelation curve for aSyn100 alone (black squares) was fitted (gray line) to determine a diffusion time of 0.43 msec; the curve for aSyn100 with POPG (blue circles) was fitted (light blue line) to determine the vesicle-bound population diffusion time of 4.9 msec and the relative populations of free protein (36%) and vesicle-bound species (64%). B-E: FCS measurements were recorded at various lipid concentrations and the fraction of bound protein is plotted to determine K_D, as indicated in the plot legends for aSyn100 with POPG (B), aSyn100 with 1:1 PC:PG (C), aSynNAC-null with POPG (D), and aSyn78 with POPG (E). K_D values are given with the standard error of the curve fitting. Adapted from data published in (Braun *et al.*, 2014, 2017).

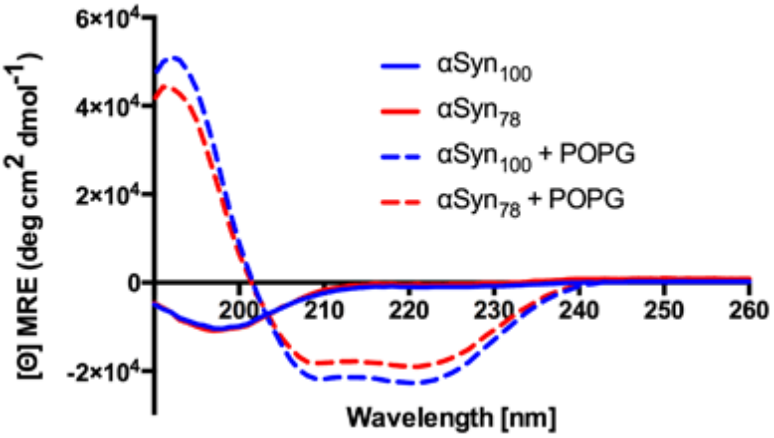

Figure 4.3 Circular dichroism spectra for aSyn100 and aSyn78

CD spectra for aSyn100 (blue) and aSyn78 (red) free in solution (solid lines) and incubated with POPG vesicles (dashed lines). Both proteins transition from characteristic random-coil signatures in solution to α-helical conformations upon binding membranes. Reprinted from (Braun *et al.*, 2017).

4.2.2 Role of lipid headgroup charge in tubulation capacity

I quantified the ability of aSyn100 to tubulate liposomes using a vesicle clearance assay, monitoring the change in the amount of scattered light from a liposome solution upon addition of protein (Varkey *et al.*, 2010). In order to test the effect of headgroup charge on aSyn100-induced tubulation at equal bound-protein density, I adjusted the added protein concentration to ensure equal density of bound protein based on the measured K_D values. I quantified aSyn100's tubulation capacity by determining the ratio of the initial scattering intensity before addition of protein to the near-final scattering intensity (t = 2400 to 2500 s) for each absorbance trace. Figure 4.4 shows the dramatic aSyn100-induced reduction in the amount of light scattered by POPG vesicles. However, the signal change upon adding aSyn100 to the 1:1 PG:PC vesicles is equivalent to that of the lipid-only control, even though the effective concentration of membrane-bound protein is the same for both samples.

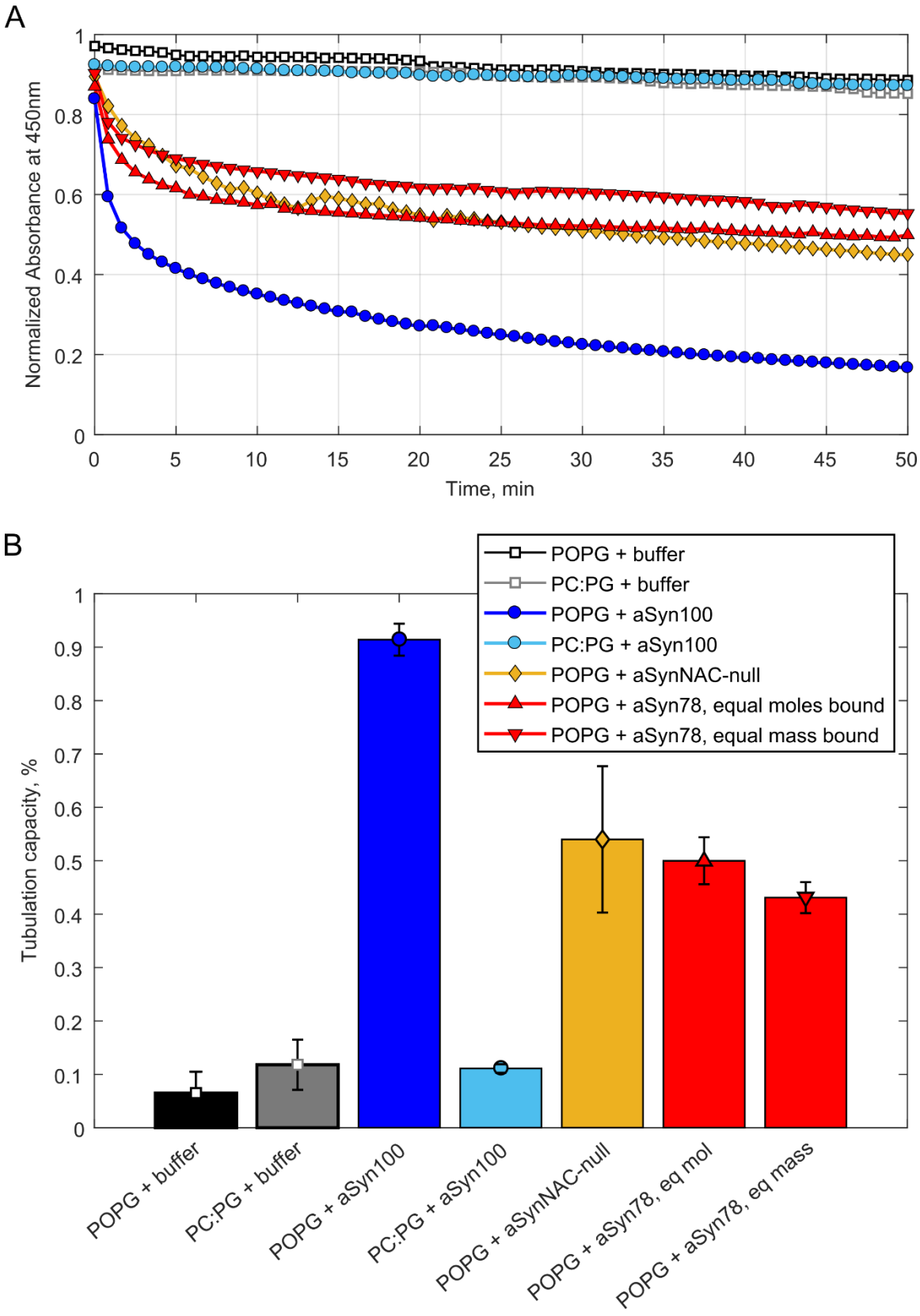

Figure 4.4 Vesicle clearance assays measure tubulation capacity of aSyn variants

A: Representative vesicle clearance curves for POPG only (black squares), 1:1 PG:PC only (gray squares), aSyn100 with POPG (blue circles), aSyn100 with 1:1 PG:PC (light blue circles), NAC-null with POPG (tan diamonds), aSyn78 with POPG (red triangles, upright), aSyn78 with POPG adjusted for equal mass bound (red triangles, inverted). All protein:lipid mixtures used 380 μM lipid and appropriate amount of protein to achieve 38 μM bound protein (except for equal-mass adjusted aSyn78 sample). B: Quantification of multiple traces for each sample, using the same color scheme as (A). Error bars show standard deviation across replicates each repeated at least 3 times. Adapted from data published in (Braun *et al.*, 2014, 2017).

4.2.3 Role of aSyn charge and hydrophobicity in binding and remodeling

Simulation data comparing aSyn100 in 100% PG and the 1:1 PG:PC mixture suggest, but do not prove, a direct correlation between the depth of partition relative to the hydrophobic thickness, the order parameter asymmetry across the leaflets, the induced positive curvature, and tubulation. Parsing the relative contributions of these driving forces – binding energy, partition depth, hydrophobic thickness, and order perturbations – is far from trivial.

In an effort to isolate the binding-energy component, we engineered a minimally altered variant of aSyn100 that would partition to the same depth in pure POPG bilayers (maintaining a constant membrane thickness and local curvature induction) but have a reduced K_D. aSyn's membrane binding domain comprises seven imperfect heptad repeats with consensus sequence XKTKEGVXXXX (X = any residue) (George *et al.*, 1995). I replaced the hydrophobic NAC domain (the sixth heptad) with a replicate of the fifth heptad ($_{68}$GAVVTGVTAVA$_{78}$ → EKTKEQVTNVG). The anticipated effect on K_D and the depth was uncertain, as the alteration reduces the hydrophobicity while adding extra charged residues (zero change in net charge). Because the positively-charged Lys residues in aSyn associate strongly with negatively-charged PG headgroups, we expected that any measured increase in binding affinity would be due to this increased charge density, while a reduction in binding affinity would be attributed to the loss in hydrophobicity.

By FCS, I found that the NAC-null variant shows approximately six-fold decrease in affinity relative to aSyn100 in POPG ($K_{D(aSynNAC\text{-}null,\ POPG)}$ = 13.6 +/- 1.5 μM, Figure 4.2), suggesting that binding of the native protein (and possibly the stability of the bound

protein-lipid complex) is significantly driven by hydrophobicity rather than primarily by electrostatics. In contrast, the ~60-fold reduction in affinity of aSyn100 for 1:1 PG:PC versus POPG has previously been shown to be electrostatically driven (Kjaer *et al.*, 2009; Pandey *et al.*, 2009; Middleton and Rhoades, 2010; Hellstrand *et al.*, 2013). These findings strongly suggest at least a two-component binding process: (1) electrostatically driven adsorption of the unfolded protein and (2) a combination of electrostatic and hydrophobic stabilization of the α-helical bound state. The NAC-null variant had an approximately 50% reduction in tubulation capacity compared to aSyn100 on POPG vesicles (Figure 4.4), even with the protein concentration adjusted to have equal density of bound protein as in the aSyn100 sample, indicating that hydrophobicity is an important driver of curvature induction upon membrane insertion.

4.2.4 Role of aSyn length in membrane remodeling

Using the same vesicle clearance assay, I found that the shorter construct aSyn78 had a reduced membrane remodeling capacity compared to aSyn100 (Figure 4.4). The assays were performed at protein concentrations to account for both the reduced affinity of aSyn78 and its shorter length, to achieve equal moles of bound protein or equal mass of bound protein. The difference between these samples was not significant, but both had significantly reduced tubulation capacity compared to aSyn100 (~50% reduction in tubulation). This suggests that the reinforcement of the local curvature contributions of individual membrane-bound proteins is affected by the length of the AH. The effect of reducing AH length from aSyn100 to aSyn78 was slightly greater than the effect of reducing the hydrophobicity in the NAC-null variant (40% reduction in tubulation).

All three members of the Synuclein protein family possess a long AH, with significant homology to aSyn (Uversky *et al.*, 2002; Ducas and Rhoades, 2012). The reduction of AH length (βSyn is shorter, containing only six 11-mer repeats) or hydrophobicity (γSyn lacks the NAC domain) may explain their reduced binding affinities relative to aSyn and the reduced membrane remodeling observed with βSyn (Varkey *et al.*, 2010). Ideally, in order to further understand these findings, I would have tested a peptide of shorter or intermediate length (aSyn 1-41 or aSyn1-93) or a NAC-null aSyn78. Unfortunately, these constructs proved difficult to express and purify.

4.3 Comparison of experimental results with molecular dynamics simulations

There are several important features for aSyn-induced membrane curvature and tubulation. I showed that at equal bound density the protein has a dramatically reduced effect on tubulation of PG:PC mixtures compared with POPG bilayers. This effect correlates with increases in bilayer hydrophobic thickness, partition depth of the protein, and lipid order parameter asymmetry in MD simulations (Braun *et al.*, 2014). These findings suggest that depth and order asymmetry alone do not explain the reduction in tubulation. Rather, the simulations suggest that the NAC domain may be essential in stabilizing protein-lipid complexes, promoting organization on the bilayer surface. A previous study highlighted the importance of the hydrophobic NAC domain in aSyn-induced membrane remodeling (Iyer *et al.*, 2014). Using supported lipid bilayers, that study showed a reduction of induced membrane defects and reduced membrane-bound protein cluster size with an aSyn variant lacking the hydrophobic sixth 11-mer.

Simulations indicate that the full length of the membrane-bound aSyn limits its rotational mobility more than aSyn78, enhancing the propagation of curvature fields of

individual proteins (Braun *et al.*, 2017). These simulations and experimental results suggest that lipid order asymmetry (either through protein partition depth or membrane hydrophobicity) and binding affinity are also necessary but are not sufficient for tubulation. Indeed, high local densities can induce curvature and recruit more proteins (Simunovic *et al.*, 2013).

Overall, these experiments showed that the extent of membrane remodeling correlates with the energy associated with binding of aSyn's AH and as well as other microscopic features of the protein-lipid interaction. Truncating the length of the amphipathic region or reducing its hydrophobicity reduce both its membrane binding affinity and its membrane remodeling capacity. MD simulation results correlate well with the experiments and support the explanation that high protein density stabilizes individual protein-induced membrane curvature fields. The extent of tubulation depends on the extent of stabilization of these curvature fields, which can be affected by a variety of features of the protein and membrane.

4.4 Conclusions

These results explain how aSyn binding to curved membranes can both stabilize high local curvature and propagate this curvature to lead to tubulation. While cellular membranes are extremely crowded with other proteins, aSyn is indeed one of the most abundant synaptic proteins with a reported average of 70 aSyn molecules per synaptic vesicle (Fakhree *et al.*, 2016). This density (1:250 protein:lipid ratio) is lower but still comparable to our and others' *in vitro* experiments and simulations, and is high enough to affect the physical properties of the membrane (Braun and Sachs, 2015). These findings suggest that aSyn might contribute to neuronal function by stabilizing the crowded,

highly curved membranes of synaptic vesicles and the plasma membrane during endocytosis or exocytosis. As current progress in the field continues to explore the physiological function of aSyn, it has become increasingly clear that its membrane-binding and membrane-remodeling activities are likely important for a role in neurotransmitter release (Busch *et al.*, 2014; Benskey *et al.*, 2016; Lautenschlager *et al.*, 2017), suggesting that a loss of normal function in addition to the pathological effects of amyloid oligomers and aggregates could be driving Parkinson's disease.

5 Summary and outlook

5.1 Future investigations into CME dynamics

In addition to the future experiments and analyses proposed in Chapter 3, further insights can be gained by comparison of my experimental results and mathematical models and simulations. I would like to compare the data generated here to simulations of dynamic actin meshworks to determine how the balance of nucleation/polymerization and disassembly could produce the observed monomer lifetime distributions (Roland *et al.*, 2008). The complexity of the process makes it difficult to extract individual rates from experiments alone, but because many components of the mechanism are well-studied, comparison to simulated models can reveal discrepancies with current knowledge or identify specific rates and steps of the models that need revision (Berro *et al.*, 2010). We can also use the experimental results to constrain simulations. Even though my residence time measurements do not reflect specific rates of individual processes, they are an important characteristic of CME dynamics that have not been described before.

The rate of turnover may also be a valuable metric for assessing the effects of drugs, mutants, or environmental stresses on the cell. Even if CME is successful under some non-native condition, it could be that the perturbation alters the molecular dynamics in ways that were not detectable by conventional fluorescence methods. For example, if cells are stressed with increased membrane tension, an increased rate of actin polymerization and turnover might enable the CME machinery to overcome the increased force without greatly altering other observable features such as the timing or total number of recruitment.

I am also interested in other CME components in addition to the actin machinery. Further experiments could measure single-molecule lifetimes to further characterize other membrane-binding proteins such as the early initiation factors or the proteins involved in scission.

5.2 Extensions to this work

It would be interesting to connect ideas across these projects. For example, because yeast do not have an endogenous Synuclein protein, an interesting extension to this work could be to investigate CME dynamics in a strain expressing aSyn. Yeast has been a valuable model organism for investigating the pathological effects of aSyn oligomers and amyloid aggregates and aSyn's effects on vesicle trafficking (Outeiro and Lindquist, 2003; Auluck *et al.*, 2010; Tenreiro *et al.*, 2016), but the physiological effects on physical properties of membranes are less well-studied. In neurons, endocytosis is tightly linked to exocytosis to recover membrane surface after synaptic vesicle fusion, and so the specific contribution of aSyn in one event or the other can difficult to isolate. In yeast, the balance between these processes is less tightly controlled as both processes proceed constitutively under normal conditions. Our lab's quantitative techniques for tracking the assembly and disassembly of CME actin dynamics can be a useful readout for experimental conditions that alter the membrane properties. I would predict that expression of aSyn in fission yeast might alleviate membrane tension and stabilize highly curved intermediates, thus lowering the force required and accelerating CME or reducing the total recruitment of actin machinery.

Similarly, it is unclear how aSyn tubulation depends on the lifetime of individual membrane-bound proteins. A single-molecule approach like the one developed here

could be useful to determine if different aSyn variants or disease-linked mutations have altered membrane-unbinding kinetics, which are not directly addressable from measurements of binding affinity. The MD simulations do not cover long enough time-scales to address how curvature propagation depends on the residence time of the protein on the membrane, but single-molecule experiments *in vitro* or *in vivo* could shed light on this aspect of the process.

Other ongoing work in our lab is investigating the role of eisosomes in modulating the cell's membrane tension, measuring the adaptations of the CME machinery in cells with and without eisosomes when challenged with osmotic or mechanical stress. We could apply similar single-molecule techniques here to monitor the Pil1p turnover and disassembly of eisosomes under stress or assess how the CME actin machinery adapts to exert higher forces on the membrane.

5.3 Conclusions

In this dissertation, I have developed new techniques to investigate the dynamics of complex membrane-binding assemblies and demonstrated that sparse labeling and single-molecule detection can reveal hidden dynamics within cellular structures. I also hope that the sparse labeling and single-molecule tracking methods developed here will be applicable in other cellular systems of interest. My work contributes to our understanding of membrane-binding and membrane-remodeling mechanisms by directly assessing behaviors at the single-molecule level. Pil1p, aSyn, and proteins in the CME machinery all induce curvature of cellular membranes, but their mechanisms of action and their cellular functions differ widely.

My findings advance our understanding of these processes in three ways: 1) providing direct evidence for dynamic turnover of the actin meshwork during CME, which supports models of force production; 2) supporting a new filament-oligomer model of the eisosome, which can explain its stability and dynamic regulation; and 3) highlighting key features of aSyn membrane binding and remodeling, which may influence its physiological role in neurons.

Appendix 1 Methods

A1.1 SRAP of Pil1p

Adapted from Lacy MM, Baddeley D, Berro J (2017). "Single-molecule imaging of the BAR-domain protein Pil1p reveals filament-end dynamics." *Molecular Biology of the Cell* 28:2251-2259.

A1.1.1 Yeast strains and SNAP labeling

I tagged the pil1 gene at its C-terminus with SNAP-tag (cloned from Addgene Plasmid #29652 pENTR4-SNAPf, inserted into pFA6a vector with KanMX6 selection marker) or mEGFP, in its native locus in a wild-type *S. pombe* strain by homologous recombination (Bahler *et al.*, 1998). Cells were grown at 32^{o} C in liquid YE5S medium to exponential phase (OD_{595nm} between 0.4 and 0.8), then diluted into liquid EMM5S medium and grown for 12 to 24 hours at 25^{o} C before labeling with SNAP fluorophore.

Although the SNAP-tag has been used successfully in a variety of applications (Klein *et al.*, 2011; Stagge *et al.*, 2013; Bosch *et al.*, 2014; Lukinavicius *et al.*, 2015), labeling cellular SNAP fusion proteins in live yeast is difficult because the cell wall impedes entry of the fluorophore substrate and because multidrug exporters prevent its accumulation in the cytoplasm (McMurray and Thorner, 2008; Stagge *et al.*, 2013). These issues may be avoided by enzymatically digesting the cell wall, deleting the multidrug exporter genes or using electroporation to allow a large amount of dye to enter the cells. However, such approaches may be problematic if the structure of interest is sensitive to cell integrity, as is the case with the eisosome. To avoid these difficulties, we opted a minimally disruptive approach, adding a low concentration of SNAP substrate fluorophore in the media for a long incubation.

To label SNAP-tag protein in live cells, 0.5 mL of cells at OD_{595nm} 0.5 were incubated at 25° C on a rotator in liquid EMM5S media containing 0.1, 0.5, or 2.5 µM of the silicon-rhodamine benzylguanine derivative SNAP-SiR647 or SNAP-Alexa647 (SNAP-Cell® 647-SiR, SNAP-Surface® Alexa Fluor® 647, New England Biolabs) for 0.5, 5, or 15 hours. For samples incubated for 15 hours, the cells were initially diluted to OD_{595nm} of 0.1 to avoid over-growing during the incubation time. Cells were washed three times by centrifuging at 900xg for 3 minutes and resuspending in 0.5 mL of EMM5S, then additionally incubated at 25° C for one hour in 0.5 mL of EMM5S, then washed three times again by centrifuging at 900xg for 3 minutes and resuspending in 0.5 mL of EMM5S. Cells were finally resuspended in about 50 µL of 0.22-µm filtered EMM5S to achieve suitable cell density for imaging.

I estimated the extent of labeling by dividing the total intensity of cells in the first frame by the mean pixel intensity of the late-appearing single molecule spots to determine the number of fluorophores per cell. I then determined the fraction of labeled Pil1p-SNAP molecules by dividing the number of fluorophores per cell by the expected visible membrane-bound fraction of total number of Pil1p molecules as determined by quantitative microscopy analysis. The samples I used for SRAP analysis (labeled 15 hours at 0.5 µM SNAP-Sir647) consistently had labeling efficiencies between 3 and 5%. Future applications of SRAP imaging should aim for a similarly low labeling efficiency, but the precise value is not critical as long as the overall shape of the structure is visible and a single-molecule regime can be reached after a short time of illumination and photobleaching. This protocol is the first reported use of SNAP-tag in live fission yeast,

and similar protocols should be easy to adapt in other organisms, especially those lacking a cell wall.

This protocol still requires use of a cell-permeable fluorophore conjugate, as incubation with SNAP-Alexa647 yielded poor labeling (Figure 2.2). Incubation with 2.5 µM of SiR647 for 15 hours achieved a higher density of labeled Pil1p-SiR (15-20% or more), but short incubations yielded only sparse labeling with greater cell-to-cell variability.

A1.1.2 Microscopy

Live cells were imaged on 25% gelatin pads in 0.22-µm filtered EMM5S media, with coverslips that had been washed in ethanol for 20 minutes and plasma treated for 2 minutes to avoid nonspecific attachment of dyes and other auto-fluorescent particles on the surface. Cells were imaged with an inverted fluorescence microscope (Ti Eclipse, Nikon) equipped with a 60x/1.49NA objective (Nikon), illuminated with a 642 nm laser (for imaging SiR647 samples) or 488 nm laser (for imaging mEGFP samples) directed through the objective to achieve TIRF, and recorded with an electron-multiplying charge-coupled device (EMCCD) camera (iXon DU897, Andor). Samples labeled with SiR647 were imaged under low illumination intensity, approximately 20 W/cm^2. Movies were recorded at a single focal plane near the cell base at 10 frames per second.

For quantitative microscopy of mEGFP-tagged proteins, cells were imaged on an inverted fluorescence microscope (Ti Eclipse, Nikon) equipped with a 60x/1.4NA Plan Apochromat Lambda objective (Nikon), coupled with a CSU-W1 spinning-disk confocal system (Yokogawa), illuminated with 488 nm laser, and recorded with an EMCCD

camera (iXon Ultra888, Andor). Cells expressing Pil1p-mEGFP or Fim1p-mEGFP were imaged in z-stacks spanning the entire cell height with 21 z-slices in 500-nm steps.

A1.1.3 Image analysis and quantification

Image analysis was carried out in the Fiji distribution of ImageJ (Schindelin *et al.*, 2012; Schneider *et al.*, 2012) and further quantification was performed in Matlab (MathWorks, Inc.), using built-in tools as well as self-written macros and scripts (Lacy *et al.*, 2017).

I first measured the lengths of filaments in the Average intensity projection of frames 1-5 (AVG1-5) of Pil1p-SiR and Pil1p-mEGFP movies by drawing a line along the full length of visible fluorescence for each filament. I then identified SRAP spots in the Maximum intensity projection of frames 50-200 (MAX50-200), after labeled eisosomes had photobleached. I first generated a preliminary list of SRAP spot positions from the MAX50-200 image by using the Find Maxima command and determining the brightness-weighted centroid of a 3-pixel diameter circle at each point.

To determine the end position of the underlying eisosome for each point in this list, I manually traced the eisosome filament in the AVG1-5 image with a 3-pixel wide line spanning past the spot position to extend beyond the end of the filament (Figure 2.3A) and analyzed the intensity profile along this line in Matlab. Spots which were more than 4 pixels away (280 nm) from the nearest eisosome were discarded (< 10% of detected spots). To find the position of the end of the eisosome underlying the diffraction-limited image, the intensity profile was fitted with the following step-like function:

$$I(x) = \frac{1}{2} * A * \left[1 - erf\left(\frac{x - x_0}{\sqrt{2} * \sigma}\right)\right]$$

This equation is equivalent to the cumulative intensity of a continuous distribution of Gaussian emitters, where I(x) is the intensity along the line coordinate x, A is the amplitude, *erf*() is the error function, x_0 is the position of the underlying step corresponding to the end of the labeled structure, and σ is the standard deviation of the diffraction-limited Gaussian spot. Measured intensity profiles were fitted in Matlab using a nonlinear fitting algorithm, with A and x_0 as independent variables and σ fixed to 1.85 pixels (130nm) representing the diffraction-limited spot width.

I used the PeakFit plugin for FIJI (University of Sussex, http://www.sussex.ac.uk/gdsc/intranet/microscopy/imagej/smlm_plugins) to determine super-resolution localizations of the spots that appeared in frames 50 to 200, calibrated with the following parameters: pixel size 70nm, wavelength 642nm, objective NA 1.49, objective proportionality factor 1.4, electron-multiplying gain 37.7; resulting in an estimated point-spread function width of 1.837 pixels. This generated a list of localizations with precision < 40 nm. From the list of SRAP events' spot centroids determined in the MAX50-200 projection, I matched each SRAP event with all localizations within a 1-pixel radius from the SRAP spot centroid. I calculated the distance from each localization to the fitted eisosome end position projected along the filament line trace (Figure 2.3A(iv)), and calculated the average distance to the end of all the associated localizations for each SRAP event. For spot centroids that did not have any associated localizations spots of sufficiently high precision, I used the brightness-weighted centroid of the SRAP spot in the projection image to determine its distance from the eisosome end.

To determine the lifetimes of SRAP events, I measured the intensity of a 3-pixel diameter circle centered on the SRAP spot position through the length of the movie after subtracting the median-filter background. I processed these intensity time-traces in Matlab with a Chung-Kennedy filter (Reuel *et al.*, 2012) to highlight discrete intensity steps (Figure 2.1C). I computed the lengths of time between steps above and below a threshold intensity, then fit the distribution of lifetimes with a single exponential curve.

To determine the photobleaching rate, I measured the mean intensity of an ROI containing an entire cell through the length of the movie. For each ROI's intensity decay profile, I subtracted the minimum baseline and normalized the intensities to the maximum value, then computed the average across all movies. I fit the average photobleaching profile with a single exponential curve, starting at frame 5 to avoid biasing the fit with the fast-bleaching autofluorescence component. I estimated the protein unbinding rate by subtracting the bulk photobleaching rate from the SRAP spot lifetime decay rate.

To determine the Pil1p binding rate, I computed the length of time between recurrent localizations in the single-molecule localization data set (from PeakFit results). I analyzed all the inter-event dark times as well as the initial dark time before the first appearance. This approach is more error-prone as missing localizations of sub-optimal spots could cause an artificially high number of very short dark times. I therefore fit a subset of the data with a single exponential curve, excluding events shorter than 0.4 sec. I considered fitting with alternative models, accounting for photobleaching of the limited pool of free Pil1p-SiR or multiple rates or other processes. However, more complex

analysis yielded little improvement and would require much larger datasets to be justified.

A1.1.4 Quantitative analysis of Pil1p-mEGFP

To quantify the number of Pil1p-mEGFP, I used quantitative microscopy approaches as described in (Wu and Pollard, 2005; Wu *et al.*, 2008). I first corrected the raw z-stacks for camera offset noise and uneven illumination. I measured the integrated intensity of sum projections of z-stacks spanning whole cells expressing Fim1p-mEGFP, Pil1p-mEGFP, or wild-type cells. I subtracted the autofluorescence intensity of wild-type cells and calibrated the brightness per mEGFP molecule in cells expressing Fim1p-mEGFP (using 86,500 +/- 9,100 molecules of Fim1p-mEGFP per cell as reported in (Wu and Pollard, 2005)) to determine the total number of Pil1-mEGFP molecules per cell. To determine the local density of Pil1p-mEGFP at eisosomes, I used sum projections of z-stacks spanning only the lower half of the cell. I measured the integrated intensity of rectangular ROIs drawn across eisosomes and subtracted the local cytoplasmic background intensity as measured in an adjacent ROI. Using the intensity per molecule calibrated from Fim1p-mEGFP stacks, I converted these intensities to number of Pil1p-mEGFP molecules per ROI. I calculated a linear density along the length of the eisosome axis (without assuming any geometry for the structure) as well as the membrane surface area density (assuming the geometry of a half cylinder with radius 16 nm, as determined from published electron micrographs (Karotki *et al.*, 2011).

A1.1.5 Characterization of eisosome end localization

I performed simulations to estimate the precision of my method of fitting an error function to the intensity traces of sparsely labeled eisosomes to localize their ends.

Indeed, this continuum model might not find the eisosome ends accurately when the structures are only sparsely labeled. From the quantitative microscopy of Pil1p-mEGFP filaments, I estimated there are approximately 2.8 Pil1p proteins per nanometer length of eisosome lattice. Therefore, for a 350-nm region (equivalent to the typical 5-pixel region of eisosome body covered by the line profile extracted above) I expect 980 possible Pil1p sites. With my estimated 3% labeling efficiency there are most likely between 20 and 50 fluorescently tagged Pil1p-SiR in this region. For each simulation, I first calculated a set of expected numbers of emitters according to a binomial distribution, then simulated each number of "emitter positions" on a uniform distribution along a 350-nm line. I added a Gaussian profile of intensity at each emitter position (mean xi, standard deviation 135 nm, peak height of 1 AU) to mimic the point spread function of the microscope, added signal from emitters outside the simulated region to account for other fluorophores on the rest of the eisosome body, and also added noise to the sum traces (random value of mean 0, standard deviation 1 AU at each x value, approximately 10-20% of the simulated fluorescence signal). I fit the resulting intensity profile (10 pixels long, including the 5-pixel region of simulated fluorophores plus 5-pixel tail region) with the error function model described above. I determined the distance from the fitted end position (position x_0) to the true end of the eisosome (position 350 nm) in each simulation.

To determine a full population average of these errors, I simulated 1,000 filaments. I repeated a similar set of simulations with a number of added fluorophores at the end position to account for the possibility of additional Pil1p-SiR binding during the imaging time which leads to a characteristic bias in fitting (Figure 2.3D and Figure 2.5).

A1.1.6 Eisosome dynamics model simulations

I compared the distribution of experimentally measured distances to datasets simulated under different hypotheses. In one model (referred to as the "uniform model"), Pil1p SRAP events occur uniformly along the eisosome, in a second model (referred to as the "end model") events occur exclusively at the end of the filament (Figure 2.4). For all models, each simulation was initialized by picking one of the eisosome lengths experimentally measured in Pil1p-SiR cells (10,000 runs with each of N = 275 filaments, Figure 2.1G). For the uniform model, the true SRAP spot positions were simulated by picking a number following a uniform distribution between zero and half the filament length, and for the end model, the true SRAP spot position was taken as the true end position of the eisosome end (position 0); a number following a Gaussian distribution (mean 0, standard deviation 30 nm) was added to represent the spot localization uncertainty as measured experimentally (Figure 2.3C). For each simulation, I added a number following a Gaussian distribution with mean 0 and standard deviation 60 nm to the true position of the eisosome end (position 0) to simulate the unbiased localization precision of the experimental fit of the eisosome end in the image analysis. Each simulated SRAP spot position was subtracted from the simulated end position to determine the relative distance from the end. In a second set of simulations to account for the fitting bias arising from a dynamic filament end, I used for the eisosome end position distribution a Gaussian distribution with mean -70 nm and standard deviation 55 nm (as in Figure 2.3D).

I also simulated a third class of models (referred to as "ragged end models") where events occur uniformly within a zone of defined length at the eisosome end. For

the ragged end models, the true SRAP spot position was simulated by picking a number following a uniform distribution between zero and the length of the end zone (e.g. 200 nm), and the end position and noise terms were generated with unbiased Gaussian distributions as described above.

A1.2 Single-molecule tracking in CME

A1.2.1 Yeast strains and SNAP labeling

S. pombe strains were generated containing the SNAP-tag inserted at genomic loci for various proteins (see Table 1), either by homologous recombination and selection with Kanamycin (Bahler *et al.*, 1998) or by CRISPR-Cas9 genome editing with fluoride selection as described in (Fernandez and Berro, 2016). Because *S. pombe* cannot survive when actin is fused with fluorescent proteins (Wu and Pollard, 2005; Wu *et al.*, 2008), I used an analogous approach as previous studies, integrating SNAP-actin into the *leu1+* locus under control of the *41nmt* promoter. The expression level of SNAP-Actin or its effect on actin functionality were not measured here, but we expect it to behave similarly to mEGFP-Actin used previously. For cells expressing mEGFP-Actin in this way, the fusion protein represents around 5% of the total actin in the cell (Wu and Pollard, 2005; Sirotkin *et al.*, 2010; Berro and Pollard, 2014b).

As discussed previously (Lacy *et al.*, 2017), SNAP-substrate fluorophore does not accumulate in high amounts in yeast cells, so I use a long labeling incubation to achieve sparse labeling. Cells were grown at 32º C in liquid YE5S medium to exponential phase (OD_{595nm} between 0.4 and 0.6), then diluted into liquid EMM5S medium and grown for 4 to 8 hours at 25º C to maintain exponential phase growth. Cells were then diluted to OD_{595nm} 0.1 in 1 mL of EMM5S containing 1 µM of the silicon-rhodamine

benzylguanine derivative SNAP-SiR647 or (SNAP-Cell® 647-SiR, New England Biolabs). Tubes were wrapped in aluminum foil to protect them from light and incubated overnight (about 15 hours) at 25° C on a rotator. Cells were washed three times by centrifuging at 1200xg for 3 minutes and resuspending in 1 mL of fresh EMM5S, then additionally incubated at 25° C for one hour in 1 mL of EMM5S, then washed three times again by centrifuging at 1200xg for 3 minutes and resuspending in 1 mL of EMM5S. Cells were finally resuspended in about 20 to 50 µL of 0.22-µm filtered EMM5S to achieve suitable cell density for imaging.

The SNAP labeling efficiency was not determined before tracking analysis, but is estimated to be around 0.1% to 1% of the total copy number of the endogenous protein level. The labeling efficiency depends on both the SNAP-fluorophore concentration and the protein expression level, so proteins that are very highly expressed or very densely localized in CME patches (e.g. Fim1p or Actin) may be labeled with lower concentration of SNAP-SiR (0.25 µM) and still achieve good single-molecule imaging conditions. Low copy-number proteins can be labeled with higher concentration of SNAP-SiR (2 to 5 µM), but this may still not be sufficient for proteins with extremely low expression. Precise knowledge of the labeled fraction is not important for typical tracking analysis as long as the images contain suitable density of spots, but it would be necessary to determine the labeled fraction in order to convert apparent event rates into binding rates.

A1.2.2 Microscopy

Cells were pipetted on to 0.25% gelatin pads, covered with a #1.5 coverslip that had been washed in ethanol for 30 minutes and plasma cleaned for 3 minutes to avoid nonspecific dye or other auto-fluorescent particles on the surface, and sealed around the

edges with Valap. Samples were imaged on an Eclipse Ti inverted microscope equipped for through-objective TIRF (Nikon), equipped with 642 nm excitation laser for SiR imaging (Spectral Applied Research) and 488 nm laser for mEGFP imaging (Spectra-Physics). Images were recorded through a 60x/1.49 NA objective (Nikon Apo TIRF), and further magnified with a 1.5x lens, and detected using an EMCCD camera (Andor iXon, DU897). The cells are magnified 90 times and the camera pixels are 16 μm in size, therefore the image pixels correspond to 178 nm. The microscope, camera, and illumination were controlled through Nikon Elements Software.

For recording TIRF movies for single-molecule tracking in SNAP-SiR labeled samples, the imaging focal plane is set about 1 to 1.5 μm below the cell midplane, just above the base of the cells adjacent to the coverslip, so that fluorescent spots in TIRF illumination are in focus. The 642 nm laser illumination intensity was set to 2.5% or 5% (measured power exiting the objective is 1.2 or 2.1 W/cm^2). The camera was set to 100 msec exposure, with EM gain set to 300 at 5MHz readout with 14-bit digitization depth. 60-second movies are recorded, starting recording with the laser off and turning it on after a few frames so that no fluorescence signal is lost in hardware delay times.

For imaging two-color strains, the microscope is not currently equipped with a dual-view beam splitter for simultaneous two-color imaging. I collected alternating red-channel and green-channel images with an acquisition protocol that switches between the SiR channel (642 nm laser at 2.1 W/cm^2) and a green channel (488 nm laser at 0.9 W/cm^2) with 200 msec exposure time and EM gain set to 300, with about 1 to 1.5 sec delay between acquisition frames to switch filter sets. A sample of Tetraspeck beads (0.2

µm) was prepared and imaged using the same protocol, to ensure alignment between channels.

A1.2.3 Spot localization and tracking

Super-resolution spot localization and track generation were done in the Python Microscopy Environment (PYME) (http://www.python-microscopy.org, (Baddeley *et al.*, 2011)). Image files are first opened with Fiji distribution of ImageJ (Schindelin *et al.*, 2012; Schneider *et al.*, 2012) and converted to TIFF file format. A metadata file is generated containing essential data such as the pixel size and other camera properties as text as follows:

```
md['voxelsize.units'] = 'um'
md['voxelsize.x'] = 0.178
md['voxelsize.y'] = 0.178
md['voxelsize.z'] = 0.300
md['Camera.TrueEMGain'] = 120
md['Camera.NoiseFactor'] = 1.41
md['Camera.ElectronsPerCount'] = 57.8
md['Camera.ReadNoise'] = 88.8
md['Camera.ADOffset'] = 105
md['EstimatedLaserOnFrameNo'] = 5
```

The camera Noise Factor of 1.41 is standard for any EMCCD camera, but the Electrons per count and Read noise can be found in the camera manufacturer's specifications sheet. The camera True EM Gain must be calibrated or determined independently, but this has not been done for the camera on the microscope I used. The value of 120 for the True EM Gain is only a rough estimate suitable for preliminary

analysis; the data will need to be re-processed with a true calibrated value in order to accurately determine the spot localization error and PSF size. The camera AD Offset ("dark level") can be determined for each movie by measuring the average pixel intensity in a dark frame from part of the movie before the laser is turned on.

I opened each movie file with DH5view and ran the spot localization analysis with the following settings: "Threshold", 1.2 (a scaling factor applied for local intensity for event detection); "Debounce rad", 3 (distance, in pixels, within which two spots cannot be separated); "Type of fit", LatGaussFitFR (uses a 2D Gaussian model for fitting individual spots); "Start at", use the frame after the frame when the laser was turned on; "Background", set to -0:0, and uncheck "Subtract Background" (the software is designed for STORM imaging, where persistent signals are attributed to background noise and are subtracted – I am interested in tracking these persistent signals and so I do not apply this). When spots are localized, the local background intensity is determined and subtracted from the total intensity, giving the fluorophore spot intensity.

The resulting set of localizations is then opened in PYME VisGUI, where it can be explored visually, corrected for drift, and filtered based on spot statistics such as brightness, size, or precision. These can be done manually in the GUI or by copying commands into the Python console. For the 2.5% laser power image conditions and data presented here, I used the following filters: A, 20-200 (fitted spot brightness); sig, 75-250 (spot width, as the standard deviation of the fitted gaussian); error_x, error_y, 0-150 (precision of fit in x and y). Note that sig and error_x and error_y are not accurately determined if the true EM gain is not calibrated, and therefore the filters used here are not very stringent. Single-molecule trajectories are generated using a maximum linking

distance of 100 nm and maximum gap of 10 frames. Again, these linking thresholds are somewhat lenient in order to account for any spots which may have been missed due to earlier filters. Any spots which are not part of a track of 3 or more spots are discarded (filter by clumpSize, 3-1000). The localization data and linked track indices are exported as a text file that can be analyzed separately.

A1.2.4 Tracks analysis

Localization and tracking results files are further analyzed in Matlab (MathWorks, Inc.) using custom-written scripts for managing these large sets of tracks as data structures. Briefly, tracks are identified by grouping all the localization entries (with their associated position, time, intensity, size and localization precision results) with shared track ID ("clumpIndex"). A variety of features are calculated such as the lifetime, start time, distance traveled, stepwise velocity, and other derivative characteristics. Tracks can be sorted, grouped or filtered based on any spot or track characteristics. Because the first few frames of the movies are more crowded (potentially introducing errors in track linking) and may contain molecules already present in CME structures (yielding only partial information on the molecule's true trajectory) or other artifacts (e.g. high background or molecular aggregates), tracks which started within 0.5 sec after the laser was turned on were discarded.

A1.3 aSyn membrane binding and tubulation assays

Adapted from Braun AR, Lacy MM, Ducas VC, Rhoades E, Sachs JN (2014). "α-Synuclein induced membrane remodeling is driven by binding affinity, partition depth, and inter-leaflet order asymmetry." *Journal of the American Chemical Society* 136:9962-72; and Braun AR, Lacy MM, Ducas VC, Rhoades E, Sachs JN (2017). "α-Synuclein's

uniquely long amphipathic helix enhances its membrane binding and remodeling capacity." *Journal of Membrane Biology* 250:183–193.

A1.3.1 Protein expression, purification, and labeling

aSyn100 was generated by introducing a stop codon via QuickChange mutagenesis (Stratagene) after residue 100 in a full-length aSyn plasmid. The aSynNAC-null construct was generated by circular polymerase extension cloning PCR (Quan and Tian, 2009). Primers were designed containing complementary sequences spanning residues Glu61-Gly67 and Asn79-Ala85; each primer contained an overhang with inverse complementary sequence coding for the residues EKTKEQVTNVG (lipid-binding repeat 5) to be inserted in place of the wild-type Gly68-Ala78 (lipid binding repeat 6).

A S9C mutation was introduced, also by QuickChange, to allow for site-specific fluorescent labeling. The protein was recombinantly expressed in *E. coli* and purified via ammonium sulfate precipitation followed by cation exchange at pH 4.0 and size exclusion chromatography. Purity and identity of protein was verified by SDS-PAGE and mass spectrometry.

For fluorescence correlation spectroscopy (FCS) experiments, aSyn variants were labeled with Alexa Fluor 488 maleimide (AL488) (Invitrogen) on the cysteine introduced at residue 9. The protein was incubated in Tris buffer (20 mM Tris, 150 mM NaCl, pH 7.4) with 10x molar excess TCEP for 5 minutes before adding 7x molar excess fluorophore for 2 hours at room temperature. Unconjugated dye was separated from the labeled protein by two stacked HiTrap desalting columns (GE Healthcare Life Sciences). UV-Vis absorbance at 495 nm was used to quantify the AL488 concentration, and the

protein concentration was determined by a modified Lowry assay (Bio-Rad). Labeling efficiency (molar ratio of dye to protein) was consistently above 85%.

A1.3.2 Vesicles

Liposomes were prepared from 100% 1-palmitoyl-2-oleoyl-sn-glycero-3-phosphoglycerol (POPG) lipid or a 1:1 mix of POPG and 1-palmitoyl-2-oleoyl-sn-glycero-3-phosphocholine (POPC) (Avanti Polar Lipids). Lipid powder was dissolved in chloroform to make 15-20 mg/mL stock solutions and stored at -20^{o} C. Aliquots of this solution were dried under nitrogen stream and desiccated overnight. The resulting film was resuspended to approximately 4 mM in MOPS buffer (20mM MOPS, 147 mM NaCl, 2.7 mM KCl, pH 7.4) for at least one hour and vortexed. The resulting liposome solutions were used as is for the tubulation assays. For FCS measurements, large unilamellar vesicles (LUVs) were prepared by extruding this suspension 21 times through two stacked membranes of 50 nm pore size (Whatman) in a Liposofast extruder (Avestin). LUVs are stored at room temperature for up to several days. Before analyses, all lipid concentrations were determined by assaying for total phosphate content (Chen *et al.*, 1956).

A1.3.3 Fluorescence Correlation Spectroscopy

FCS measurements were made on a lab-built instrument based around an IX71 inverted microscope (Olympus) and a 488 nm DPSS laser (Coherent) as described previously (Trexler and Rhoades, 2009). Laser power was adjusted to 5 μW prior to entering the microscope. Fluorescence emission was collected through the objective and separated from laser excitation using a Z488rdc long-pass dichroic and an HQ600/200m band-pass filter (Chroma) and focused onto the aperture of a 50 μm optical fiber (Oz

Optics) directly coupled to an avalanche photodiode (Pacer). A digital correlator (Flex03LQ-12, correlator.com) was used to generate the autocorrelation curve.

FCS measurements were made in 8-well chambered coverglasses (Nunc). Chambers were plasma treated and passivated by coating with polylysine-conjugated polyethylene glycol to prevent protein adsorption to the surface (Middleton and Rhoades, 2010). Binding studies were carried out at 20° C, mixing 100 nM protein with various concentrations of 100% POPG or 1:1 POPG:POPC LUVs in MOPS buffer in a well (250 μL total volume) and allowing to equilibrate for 8 to 10 minutes before measuring. For each FCS measurement, 30 traces of 10 seconds each were recorded and averaged together to obtain statistical variations. The average curve was fit to an equation for multiple species of differing brightness using MATLAB (The MathWorks):

$$G(\tau) = \frac{1}{N}\left(F * \frac{1}{1+\frac{\tau}{\tau_{D1}}} * \left(\frac{1}{1+\frac{s^2\tau}{\tau_{D1}}}\right)^{1/2} + Q * (1-F)\frac{1}{1+\frac{\tau}{\tau_{D2}}} * \left(\frac{1}{1+\frac{s^2\tau}{\tau_{D2}}}\right)^{1/2} \right)$$

where τD1 and τD2, the diffusion times for the free protein and vesicle-bound protein, are determined by measurements of samples in the absence of lipid and with very high lipid concentration (all protein is bound), respectively and fixed to within 5% of these values for fitting curves from intermediate lipid concentrations. The structure factor s, the ratio of the radial to axial dimensions of the focal volume, was calibrated by measuring a solution of Alexa488 hydrazide and was fixed to 0.17. The only free parameters are: N, the number of fluorescent species; F, the fraction of protein not bound to vesicles; and Q, the average brightness of the vesicles.

Binding data from experiments at various lipid concentrations were fit with a hyperbolic binding curve in Origin (OriginLab) to determine the K_D:

$$F' = \frac{[lipid]}{K_D + [lipid]}$$

where F' is the fraction of vesicle-bound protein, determined from fitting the FCS equation, and [*lipid*] is the molar concentration of accessible lipid, the outer membrane leaflet, calculated as 55% of the total lipid concentration.

A1.3.4 Vesicle tubulation

To monitor remodeling of liposomes into tubular structures by aSyn variants, the decrease in scattered light at 450 nm was measured as a function of time (Varkey *et al.*, 2010). Absorbance was monitored at 450nm with 1 nm slit width, 1 second response time in a spectrophotometer (Perkin-Elmer) every 2 seconds. To obtain a baseline signal, 150 μL of 400 μM lipids (100% POPG or 1:1 POPG:POPC liposomes) in MOPS buffer with 1 mM TCEP was placed in a quartz cuvette and monitored for at least 5 minutes. Appropriate amounts of protein (in MOPS buffer with 1 mM TCEP) were added to achieve a 1:10 ratio of bound protein:lipid as determined by the quadratic binding equation:

$$\frac{[PL]}{[P_{tot}]} = \frac{(K_D + [P_{tot}] + [L_{tot}]) - \sqrt{(K_D + [P_{tot}] + [L_{tot}])^2 - 4[P_{tot}][L_{tot}]}}{2[P_{tot}]}$$

where $[PL]$ is the concentration of lipid-bound protein, $[P_{tot}]$ is the total concentration of protein, $[L_{tot}]$ is the total concentration of accessible lipid, and K_D is the dissociation constant calculated from the FCS measurements.

Absorbance intensity traces were normalized to the initial lipid-only signal for each sample, and the extent of tubulation was determined by taking the average

absorbance of the 50 time points from 2400-2500 sec and subtracting from the initial value. At least three replicates were performed for each lipid composition.

A1.3.5 Circular Dichroism

Circular dichroism (CD) experiments were performed on an Aviv spectrometer, model 215. All samples were prepared in 10 mM sodium phosphate with 0.1mM TCEP, pH adjusted to 7.4. aSyn100 or aSyn78 was incubated at 500 μM with 1 mM TCEP for 30 min on ice, then diluted to 20 μM before measuring, with 0.1 mM TCEP during the measurement. The lipids were not extruded, resuspended to approximately 4mM in the phosphate buffer for ~1.5 h before the measurements, and diluted to 400 μM for measurement. Protein and lipid were mixed (20 μM aSyn and 400 μM POPG) and allowed to equilibrate for 10 min prior to measurement to allow sufficient time for the protein to bind.

Table 1 Yeast strains used in this study

Strain	Genotype	Source
FY527	*ade6-M216 his3-D1 leu1-32 ura4-D18 h-*	S. Forsburg
JB198	*pil1-SNAP-kanMX6 ade6-M216 his3-D1 leu1-32 ura4-D18 h-*	(Lacy 2017)
JB204	*pil1-mEGFP-kanMX6 ade6-M216 his3-D1 leu1-32 ura4-D18 h-*	(Lacy 2017)
JB57	*fim1-mEGFP-natMX6 ade6-M210 his3-D1 leu1-32 ura4-D18 h+*	(Berro and Pollard, 2014)
JB135	*fim1-SNAP-kanMX6 ade6-M216 his3-D1 leu1-32 ura4-D18 h-*	This study
JB150	*acp2-mEGFP-kanMX6 fim1-SNAP-kanMX6 ade6-M216 his3-D1 leu1-32 ura4-D18 h-*	This study
JB202	*clc1-SNAP-kanMX6 ade6-M216 his3-D1 leu1-32 ura4-D18 h-*	This study
JB216	*41nmt1-SNAP-actin-leu+ ade6-M216 his3-D1 ura4-D19 h-*	This study
JB304	*SNAP-myo1 fex1Δ fex2Δ ade6-M216 his3-D1 leu1-32 ura4-D18 h-*	This study
JB305	*acp1-SNAP fex1Δ fex2Δ ade6-M216 his3-D1 leu1-32 ura4-D18 h-*	This study

JB307	*end4-SNAP fex1Δ fex2Δ ade6-M216 his3-D1 leu1-32 ura4-D18 h-*	This study
JB320	*crn1-SNAP fex1Δ fex2Δ ade6-M216 his3-D1 leu1-32 ura4-D18 h-*	This study
JB338	*SNAP-aip1 fex1Δ fex2Δ ade6-M216 his3-D1 leu1-32 ura4-D18 h-*	This study
JB346	*arc5-SNAP fex1Δ fex2Δ ade6-M216 his3-D1 leu1-32 ura4-D18 h-*	This study
JB360	*arp3-SNAP fex1Δ fex2Δ ade6-M216 his3-D1 leu1-32 ura4-D18 h-*	This study
JB393	*SNAP-wsp1 fex1Δ fex2Δ ade6-M216 his3-D1 leu1-32 ura4-D18 h-*	This study

References

Adam, J., Basnet, N., and Mizuno, N. (2015). Structural insights into the cooperative remodeling of membranes by amphiphysin/BIN1. Sci Rep *5*, 15452.

Aghamohammadzadeh, S., and Ayscough, K.R. (2009). Differential requirements for actin during yeast and mammalian endocytosis. Nat Cell Biol *11*, 1039-1042.

Aguilar, P.S., Frohlich, F., Rehman, M., Shales, M., Ulitsky, I., Olivera-Couto, A., Braberg, H., Shamir, R., Walter, P., Mann, M., Ejsing, C.S., Krogan, N.J., and Walther, T.C. (2010). A plasma-membrane E-MAP reveals links of the eisosome with sphingolipid metabolism and endosomal trafficking. Nat Struct Mol Biol *17*, 901-908.

Antonny, B. (2011). Mechanisms of membrane curvature sensing. Annu Rev Biochem *80*, 101-123.

Arasada, R., and Pollard, T.D. (2011). Distinct roles for F-BAR proteins Cdc15p and Bzz1p in actin polymerization at sites of endocytosis in fission yeast. Curr Biol *21*, 1450-1459.

Arasada, R., Sayyad, W.A., Berro, J., and Pollard, T.D. (2018). High-speed superresolution imaging of the proteins in fission yeast clathrin-mediated endocytic actin patches. Mol Biol Cell *29*, 295-303.

Auluck, P.K., Caraveo, G., and Lindquist, S. (2010). alpha-Synuclein: membrane interactions and toxicity in Parkinson's disease. Annu Rev Cell Dev Biol *26*, 211-233.

Avinoam, O., Schorb, M., Beese, C.J., Briggs, J.A., and Kaksonen, M. (2015). Endocytic sites mature by continuous bending and remodeling of the clathrin coat. Science *348*, 1369-1372.

Baddeley, D., Crossman, D., Rossberger, S., Cheyne, J.E., Montgomery, J.M., Jayasinghe, I.D., Cremer, C., Cannell, M.B., and Soeller, C. (2011). 4D super-resolution microscopy with conventional fluorophores and single wavelength excitation in optically thick cells and tissues. PLoS One *6*, e20645.

Baggett, J.J., D'Aquino, K.E., and Wendland, B. (2003). The Sla2p talin domain plays a role in endocytosis in Saccharomyces cerevisiae. Genetics *165*, 1661-1674.

Bahler, J., Wu, J.Q., Longtine, M.S., Shah, N.G., McKenzie, A., 3rd, Steever, A.B., Wach, A., Philippsen, P., and Pringle, J.R. (1998). Heterologous modules for efficient and versatile PCR-based gene targeting in Schizosaccharomyces pombe. Yeast *14*, 943-951.

Benskey, M.J., Perez, R.G., and Manfredsson, F.P. (2016). The contribution of alpha synuclein to neuronal survival and function - Implications for Parkinson's disease. Journal of neurochemistry *137*, 331-359.

Berro, J., and Pollard, T.D. (2014a). Local and global analysis of endocytic patch dynamics in fission yeast using a new "temporal superresolution" realignment method. Mol Biol Cell *25*, 3501-3514.

Berro, J., and Pollard, T.D. (2014b). Synergies between Aip1p and capping protein subunits (Acp1p and Acp2p) in clathrin-mediated endocytosis and cell polarization in fission yeast. Mol Biol Cell *25*, 3515-3527.

Berro, J., Sirotkin, V., and Pollard, T.D. (2010). Mathematical modeling of endocytic actin patch kinetics in fission yeast: disassembly requires release of actin filament fragments. Mol Biol Cell *21*, 2905-2915.

Betzig, E., Patterson, G.H., Sougrat, R., Lindwasser, O.W., Olenych, S., Bonifacino, J.S., Davidson, M.W., Lippincott-Schwartz, J., and Hess, H.F. (2006). Imaging intracellular fluorescent proteins at nanometer resolution. Science *313*, 1642-1645.

Bhatia, V.K., Madsen, K.L., Bolinger, P.Y., Kunding, A., Hedegard, P., Gether, U., and Stamou, D. (2009). Amphipathic motifs in BAR domains are essential for membrane curvature sensing. EMBO J *28*, 3303-3314.

Boettner, D.R., Chi, R.J., and Lemmon, S.K. (2011). Lessons from yeast for clathrin-mediated endocytosis. Nat Cell Biol *14*, 2-10.

Bökel, C., and Brand, M. (2014). Endocytosis and signaling during development. Cold Spring Harb Perspect Biol *6*.

Bombardier, J.P., Eskin, J.A., Jaiswal, R., Correa, I.R., Jr., Xu, M.Q., Goode, B.L., and Gelles, J. (2015). Single-molecule visualization of a formin-capping protein 'decision complex' at the actin filament barbed end. Nat Commun *6*, 8707.

Bosch, P.J., Correa, I.R., Jr., Sonntag, M.H., Ibach, J., Brunsveld, L., Kanger, J.S., and Subramaniam, V. (2014). Evaluation of fluorophores to label SNAP-tag fused proteins for multicolor single-molecule tracking microscopy in live cells. Biophys J *107*, 803-814.

Boulant, S., Kural, C., Zeeh, J.C., Ubelmann, F., and Kirchhausen, T. (2011). Actin dynamics counteract membrane tension during clathrin-mediated endocytosis. Nat Cell Biol *13*, 1124-1131.

Brach, T., Godlee, C., Moeller-Hansen, I., Boeke, D., and Kaksonen, M. (2014). The initiation of clathrin-mediated endocytosis is mechanistically highly flexible. Curr Biol *24*, 548-554.

Brameshuber, M., and Schutz, G.J. (2012). Detection and quantification of biomolecular association in living cells using single-molecule microscopy. Methods Enzymol *505*, 159-186.

Braun, A.R., Lacy, M.M., Ducas, V.C., Rhoades, E., and Sachs, J.N. (2014). alpha-Synuclein-induced membrane remodeling is driven by binding affinity, partition depth, and interleaflet order asymmetry. J Am Chem Soc *136*, 9962-9972.

Braun, A.R., Lacy, M.M., Ducas, V.C., Rhoades, E., and Sachs, J.N. (2017). alpha-Synuclein's Uniquely Long Amphipathic Helix Enhances its Membrane Binding and Remodeling Capacity. The Journal of membrane biology *250*, 183-193.

Braun, A.R., and Sachs, J.N. (2015). alpha-Synuclein Reduces Tension and Increases Undulations in Simulations of Small Unilamellar Vesicles. Biophys J *108*, 1848-1851.

Braun, A.R., Sevcsik, E., Chin, P., Rhoades, E., Tristram-Nagle, S., and Sachs, J.N. (2012). alpha-Synuclein Induces Both Positive Mean Curvature and Negative Gaussian Curvature in Membranes. Journal of the American Chemical Society *134*, 2613-2620.

Bryan, K.E., and Rubenstein, P.A. (2005). An intermediate form of ADP-F-actin. J Biol Chem *280*, 1696-1703.

Busch, D.J., Houser, J.R., Hayden, C.C., Sherman, M.B., Lafer, E.M., and Stachowiak, J.C. (2015). Intrinsically disordered proteins drive membrane curvature. Nat Commun *6*, 7875.

Busch, D.J., Oliphint, P.A., Walsh, R.B., Banks, S.M., Woods, W.S., George, J.M., and Morgan, J.R. (2014). Acute increase of alpha-synuclein inhibits synaptic vesicle recycling evoked during intense stimulation. Mol Biol Cell *25*, 3926-3941.

Carlsson, A.E., and Bayly, P.V. (2014). Force generation by endocytic actin patches in budding yeast. Biophys J *106*, 1596-1606.

Carpy, A., Krug, K., Graf, S., Koch, A., Popic, S., Hauf, S., and Macek, B. (2014). Absolute proteome and phosphoproteome dynamics during the cell cycle of Schizosaccharomyces pombe (Fission Yeast). Mol Cell Proteomics *13*, 1925-1936.

Cataldo, A., Rebeck, G.W., Ghetri, B., Hulette, C., Lippa, C., Van Broeckhoven, C., van Duijn, C., Cras, P., Bogdanovic, N., Bird, T., Peterhoff, C., and Nixon, R. (2001). Endocytic disturbances distinguish among subtypes of Alzheimer's disease and related disorders. Annals of neurology *50*, 661-665.

Chandra, S., Chen, X.C., Rizo, J., Jahn, R., and Sudhof, T.C. (2003). A broken alpha-helix in folded alpha-synuclein. Journal of Biological Chemistry *278*, 15313-15318.

Chen, P.H., Bendris, N., Hsiao, Y.J., Reis, C.R., Mettlen, M., Chen, H.Y., Yu, S.L., and Schmid, S.L. (2017). Crosstalk between CLCb/Dyn1-Mediated Adaptive

Clathrin-Mediated Endocytosis and Epidermal Growth Factor Receptor Signaling Increases Metastasis. Dev Cell *40*, 278-288 e275.

Chen, P.S., Toribara, T.Y., and Warner, H. (1956). Microdetermination of Phosphorus. Analytical Chemistry *28*, 1756-1758.

Chen, Q., and Pollard, T.D. (2011). Actin filament severing by cofilin is more important for assembly than constriction of the cytokinetic contractile ring. J Cell Biol *195*, 485-498.

Chen, Q., and Pollard, T.D. (2013). Actin filament severing by cofilin dismantles actin patches and produces mother filaments for new patches. Curr Biol *23*, 1154-1162.

Cocucci, E., Aguet, F., Boulant, S., and Kirchhausen, T. (2012). The first five seconds in the life of a clathrin-coated pit. Cell *150*, 495-507.

Collins, A., Warrington, A., Taylor, K.A., and Svitkina, T. (2011). Structural organization of the actin cytoskeleton at sites of clathrin-mediated endocytosis. Curr Biol *21*, 1167-1175.

Cornell, R.B., and Taneva, S.G. (2006). Amphipathic helices as mediators of the membrane interaction of amphitropic proteins, and as modulators of bilayer physical properties. Current Protein & Peptide Science *7*, 539-552.

Cremona, O., Di Paolo, G., Wenk, M.R., Luthi, A., Kim, W.T., Takei, K., Daniell, L., Nemoto, Y., Shears, S.B., Flavell, R.A., McCormick, D.A., and De Camilli, P. (1999). Essential role of phosphoinositide metabolism in synaptic vesicle recycling. Cell *99*, 179-188.

Crowet, J.M., Lins, L., Dupiereux, I., Elmoualija, B., Lorin, A., Charloteaux, B., Stroobant, V., Heinen, E., and Brasseur, R. (2007). Tilted properties of the 67-78

fragment of alpha-synuclein are responsible for membrane destabilization and neurotoxicity. Proteins *68*, 936-947.

Cui, H., Lyman, E., and Voth, G.A. (2011). Mechanism of Membrane Curvature Sensing by Amphipathic Helix Containing Proteins. Biophysical Journal *100*, 1271-1279.

Dannhauser, P.N., and Ungewickell, E.J. (2012). Reconstitution of clathrin-coated bud and vesicle formation with minimal components. Nat Cell Biol *14*, 634-639.

Danuser, G., and Waterman-Storer, C.M. (2006). Quantitative fluorescent speckle microscopy of cytoskeleton dynamics. Annu Rev Biophys Biomol Struct *35*, 361-387.

Daste, F., Walrant, A., Holst, M.R., Gadsby, J.R., Mason, J., Lee, J.E., Brook, D., Mettlen, M., Larsson, E., Lee, S.F., Lundmark, R., and Gallop, J.L. (2017). Control of actin polymerization via the coincidence of phosphoinositides and high membrane curvature. J Cell Biol *216*, 3745-3765.

Daum, B., Auerswald, A., Gruber, T., Hause, G., Balbach, J., Kuhlbrandt, W., and Meister, A. (2016). Supramolecular organization of the human N-BAR domain in shaping the sarcolemma membrane. J Struct Biol *194*, 375-382.

Daumke, O., Roux, A., and Haucke, V. (2014). BAR domain scaffolds in dynamin-mediated membrane fission. Cell *156*, 882-892.

Di Paolo, G., and De Camilli, P. (2006). Phosphoinositides in cell regulation and membrane dynamics. Nature *443*, 651-657.

Dmitrieff, S., and Nedelec, F. (2015). Membrane Mechanics of Endocytosis in Cells with Turgor. PLoS Comput Biol *11*, e1004538.

Douglas, L.M., and Konopka, J.B. (2014). Fungal membrane organization: the eisosome concept. Annu Rev Microbiol *68*, 377-393.

Doyon, J.B., Zeitler, B., Cheng, J., Cheng, A.T., Cherone, J.M., Santiago, Y., Lee, A.H., Vo, T.D., Doyon, Y., Miller, J.C., Paschon, D.E., Zhang, L., Rebar, E.J., Gregory, P.D., Urnov, F.D., and Drubin, D.G. (2011). Rapid and efficient clathrin-mediated endocytosis revealed in genome-edited mammalian cells. Nat Cell Biol *13*, 331-337.

Drin, G., and Antonny, B. (2010). Amphipathic helices and membrane curvature. FEBS Lett *584*, 1840-1847.

Ducas, V.C., and Rhoades, E. (2012). Quantifying Interactions of beta-Synuclein and gamma-Synuclein with Model Membranes. Journal of Molecular Biology *423*, 528-539.

Ducas, V.C., and Rhoades, E. (2014). Investigation of Intramolecular Dynamics and Conformations of alpha-, beta- and gamma-Synuclein. Plos One *9*.

Fakhree, M.A.A., Zijlstra, N., Raiss, C.C., Siero, C.J., Grabmayr, H., Bausch, A.R., Blum, C., and Claessens, M. (2016). The number of α-synuclein proteins per vesicle gives insights into its physiological function. Sci Rep *6*.

Fernandez, R., and Berro, J. (2016). Use of a fluoride channel as a new selection marker for fission yeast plasmids and application to fast genome editing with CRISPR/Cas9. Yeast *33*, 549-557.

Floyd, D.L., Harrison, S.C., and van Oijen, A.M. (2010). Analysis of kinetic intermediates in single-particle dwell-time distributions. Biophys J *99*, 360-366.

Frohlich, F., Christiano, R., Olson, D.K., Alcazar-Roman, A., DeCamilli, P., and Walther, T.C. (2014). A role for eisosomes in maintenance of plasma membrane phosphoinositide levels. Mol Biol Cell *25*, 2797-2806.

Gaidarov, I., Santini, F., Warren, R.A., and Keen, J.H. (1999). Spatial control of coated-pit dynamics in living cells. Nat Cell Biol *1*, 1-7.

Gandhi, S., and Wood, N.W. (2005). Molecular pathogenesis of Parkinson's disease. Human molecular genetics *14 Spec No. 2*, 2749-2755.

Gardner, M.K., Charlebois, B.D., Janosi, I.M., Howard, J., Hunt, A.J., and Odde, D.J. (2011). Rapid microtubule self-assembly kinetics. Cell *146*, 582-592.

George, J.M., Jin, H., Woods, W.S., and Clayton, D.F. (1995). Characterization of a novel protein regulated during the critical period for song learning in the zebra finch. Neuron *15*, 361-372.

Georgieva, E.R., Ramlall, T.F., Borbat, P.P., Freed, J.H., and Eliezer, D. (2008). Membrane-bound alpha-synuclein forms an extended helix: long-distance pulsed ESR measurements using vesicles, bicelles, and rodlike micelles. J Am Chem Soc *130*, 12856-12857.

Gibson, T.J., Seiler, M., and Veitia, R.A. (2013). The transience of transient overexpression. Nat Methods *10*, 715-721.

Goedert, M., Jakes, R., and Spillantini, M.G. (2017). The Synucleinopathies: Twenty Years On. Journal of Parkinson's disease *7*, S53-s71.

Goldenbogen, B., Giese, W., Hemmen, M., Uhlendorf, J., Herrmann, A., and Klipp, E. (2016). Dynamics of cell wall elasticity pattern shapes the cell during yeast mating morphogenesis. Open biology *6*.

Goode, B.L., Eskin, J.A., and Wendland, B. (2015). Actin and endocytosis in budding yeast. Genetics *199*, 315-358.

Grove, J., Metcalf, D.J., Knight, A.E., Wavre-Shapton, S.T., Sun, T., Protonotarios, E.D., Griffin, L.D., Lippincott-Schwartz, J., and Marsh, M. (2014). Flat clathrin lattices: stable features of the plasma membrane. Mol Biol Cell *25*, 3581-3594.

Hatzakis, N.S., Bhatia, V.K., Larsen, J., Madsen, K.L., Bolinger, P.Y., Kunding, A.H., Castillo, J., Gether, U., Hedegard, P., and Stamou, D. (2009). How curved membranes recruit amphipathic helices and protein anchoring motifs. Nat Chem Biol *5*, 835-841.

Hellstrand, E., Grey, M., Ainalem, M.L., Ankner, J., Forsyth, V.T., Fragneto, G., Haertlein, M., Dauvergne, M.T., Nilsson, H., Brundin, P., Linse, S., Nylander, T., and Sparr, E. (2013). Adsorption of alpha-synuclein to supported lipid bilayers: positioning and role of electrostatics. ACS Chemical Neuroscience *4*, 1339-1351.

Hess, S.T., Girirajan, T.P., and Mason, M.D. (2006). Ultra-high resolution imaging by fluorescence photoactivation localization microscopy. Biophys J *91*, 4258-4272.

Iyer, A., Petersen N , O., Claessens M , M.A.E., and Subramaniam, V. (2014). Amyloids of Alpha-Synuclein Affect the Structure and Dynamics of Supported Lipid Bilayers. Biophys J *106*, 2585-2594.

Jansen, S., Collins, A., Chin, S.M., Ydenberg, C.A., Gelles, J., and Goode, B.L. (2015). Single-molecule imaging of a three-component ordered actin disassembly mechanism. Nat Commun *6*, 7202.

Jao, C.C., Hegde, B.G., Chen, J., Haworth, I.S., and Langen, R. (2008). Structure of membrane-bound alpha-synuclein from site-directed spin labeling and

computational refinement. Proceedings of the National Academy of Sciences of the United States of America *105*, 19666-19671.

Jiang, Z., de Messieres, M., and Lee, J.C. (2013). Membrane Remodeling by alpha-Synuclein and Effects on Amyloid Formation. Journal of the American Chemical Society *135*, 15970-15973.

Johannes, L., Parton, R.G., Bassereau, P., and Mayor, S. (2015). Building endocytic pits without clathrin. Nat Rev Mol Cell Biol *16*, 311-321.

Jonsdottir, G.A., and Li, R. (2004). Dynamics of yeast Myosin I: evidence for a possible role in scission of endocytic vesicles. Curr Biol *14*, 1604-1609.

Kabeche, R., Baldissard, S., Hammond, J., Howard, L., and Moseley, J.B. (2011). The filament-forming protein Pil1 assembles linear eisosomes in fission yeast. Mol Biol Cell *22*, 4059-4067.

Kabeche, R., Howard, L., and Moseley, J.B. (2015a). Eisosomes provide membrane reservoirs for rapid expansion of the yeast plasma membrane. J Cell Sci *128*, 4057-4062.

Kabeche, R., Madrid, M., Cansado, J., and Moseley, J.B. (2015b). Eisosomes Regulate Phosphatidylinositol 4,5-Bisphosphate (PI(4,5)P2) Cortical Clusters and Mitogen-activated Protein (MAP) Kinase Signaling upon Osmotic Stress. J Biol Chem *290*, 25960-25973.

Kaksonen, M., Sun, Y., and Drubin, D.G. (2003). A pathway for association of receptors, adaptors, and actin during endocytic internalization. Cell *115*, 475-487.

Kaksonen, M., Toret, C.P., and Drubin, D.G. (2005). A modular design for the clathrin- and actin-mediated endocytosis machinery. Cell *123*, 305-320.

Kaksonen, M., Toret, C.P., and Drubin, D.G. (2006). Harnessing actin dynamics for clathrin-mediated endocytosis. Nat Rev Mol Cell Biol *7*, 404-414.

Kamp, F., Exner, N., Lutz, A.K., Wender, N., Hegermann, J., Brunner, B., Nuscher, B., Bartels, T., Giese, A., Beyer, K., Eimer, S., Winklhofer, K.F., and Haass, C. (2010). Inhibition of mitochondrial fusion by alpha-synuclein is rescued by PINK1, Parkin and DJ-1. Embo Journal *29*, 3571-3589.

Karotki, L., Huiskonen, J.T., Stefan, C.J., Ziolkowska, N.E., Roth, R., Surma, M.A., Krogan, N.J., Emr, S.D., Heuser, J., Grunewald, K., and Walther, T.C. (2011). Eisosome proteins assemble into a membrane scaffold. J Cell Biol *195*, 889-902.

Kay, B.K., Yamabhai, M., Wendland, B., and Emr, S.D. (1999). Identification of a novel domain shared by putative components of the endocytic and cytoskeletal machinery. Protein Sci *8*, 435-438.

Keppler, A., Gendreizig, S., Gronemeyer, T., Pick, H., Vogel, H., and Johnsson, K. (2003). A general method for the covalent labeling of fusion proteins with small molecules in vivo. Nat Biotechnol *21*, 86-89.

Khanduja, N., and Kuhn, J.R. (2014). Processive acceleration of actin barbed-end assembly by N-WASP. Mol Biol Cell *25*, 55-65.

Kirchhausen, T., Owen, D., and Harrison, S.C. (2014). Molecular structure, function, and dynamics of clathrin-mediated membrane traffic. Cold Spring Harb Perspect Biol *6*, a016725.

Kjaer, L., Giehm, L., Heimburg, T., and Otzen, D. (2009). The Influence of Vesicle Size and Composition on α-Synuclein Structure and Stability. Biophys J *96*, 2857-2870.

Klein, T., Loschberger, A., Proppert, S., Wolter, S., van de Linde, S., and Sauer, M. (2011). Live-cell dSTORM with SNAP-tag fusion proteins. Nat Methods *8*, 7-9.

Kozlov, M.M., Campelo, F., Liska, N., Chernomordik, L.V., Marrink, S.J., and McMahon, H.T. (2014). Mechanisms shaping cell membranes. Curr Opin Cell Biol *29*, 53-60.

Kuhn, J.R., and Pollard, T.D. (2007). Single molecule kinetic analysis of actin filament capping. Polyphosphoinositides do not dissociate capping proteins. J Biol Chem *282*, 28014-28024.

Kukulski, W., Schorb, M., Kaksonen, M., and Briggs, J.A. (2012). Plasma membrane reshaping during endocytosis is revealed by time-resolved electron tomography. Cell *150*, 508-520.

Kumari, S., Mg, S., and Mayor, S. (2010). Endocytosis unplugged: multiple ways to enter the cell. Cell research *20*, 256-275.

Lacy, M.M., Baddeley, D., and Berro, J. (2017). Single-molecule imaging of the BAR-domain protein Pil1p reveals filament-end dynamics. Mol Biol Cell *28*, 2251-2259.

Lautenschlager, J., Kaminski, C.F., and Kaminski Schierle, G.S. (2017). alpha-Synuclein - Regulator of Exocytosis, Endocytosis, or Both? Trends Cell Biol *27*, 468-479.

Liu, J., Sun, Y., Drubin, D.G., and Oster, G.F. (2009). The mechanochemistry of endocytosis. PLoS Biol *7*, e1000204.

Lowengrub, J., Allard, J., and Aland, S. (2016). Numerical simulation of endocytosis: Viscous flow driven by membranes with non-uniformly distributed curvature-inducing molecules. J Comput Phys *309*, 112-128.

Lukinavicius, G., Reymond, L., and Johnsson, K. (2015). Fluorescent labeling of SNAP-tagged proteins in cells. Methods Mol Biol *1266*, 107-118.

Lukinavicius, G., Umezawa, K., Olivier, N., Honigmann, A., Yang, G., Plass, T., Mueller, V., Reymond, L., Correa, I.R., Jr., Luo, Z.G., Schultz, C., Lemke, E.A., Heppenstall, P., Eggeling, C., Manley, S., and Johnsson, K. (2013). A near-infrared fluorophore for live-cell super-resolution microscopy of cellular proteins. Nat Chem *5*, 132-139.

Ma, R., and Berro, J. (2017). Structural organization and energy storage in crosslinked actin-assemblies. bioRxiv.

Madsen, K.L., and Herlo, R. (2017). Recursive Alterations of the Relationship between Simple Membrane Geometry and Insertion of Amphiphilic Motifs. Membranes *7*.

Malinska, K., Malinsky, J., Opekarova, M., and Tanner, W. (2003). Visualization of protein compartmentation within the plasma membrane of living yeast cells. Mol Biol Cell *14*, 4427-4436.

Manley, S., Gillette, J.M., Patterson, G.H., Shroff, H., Hess, H.F., Betzig, E., and Lippincott-Schwartz, J. (2008). High-density mapping of single-molecule trajectories with photoactivated localization microscopy. Nat Methods *5*, 155-157.

Marks, J., and Hyams, J.S. (1985). Localization of F-Actin through the Cell-Division Cycle of Schizosaccharomyces Pombe. European Journal of Cell Biology *39*, 27-32.

Mattila, J.P., Shnyrova, A.V., Sundborger, A.C., Hortelano, E.R., Fuhrmans, M., Neumann, S., Muller, M., Hinshaw, J.E., Schmid, S.L., and Frolov, V.A. (2015).

A hemi-fission intermediate links two mechanistically distinct stages of membrane fission. Nature *524*, 109-113.

Maxfield, F.R. (2014). Role of endosomes and lysosomes in human disease. Cold Spring Harb Perspect Biol *6*, a016931.

McDonald, N.A., and Gould, K.L. (2016). Linking up at the BAR: Oligomerization and F-BAR protein function. Cell Cycle *15*, 1977-1985.

McMahon, H.T., and Boucrot, E. (2011). Molecular mechanism and physiological functions of clathrin-mediated endocytosis. Nat Rev Mol Cell Biol *12*, 517-533.

McMurray, M.A., and Thorner, J. (2008). Septin stability and recycling during dynamic structural transitions in cell division and development. Curr Biol *18*, 1203-1208.

Mellman, I., and Yarden, Y. (2013). Endocytosis and cancer. Cold Spring Harb Perspect Biol *5*, a016949.

Mercer, J., Schelhaas, M., and Helenius, A. (2010). Virus entry by endocytosis. Annu Rev Biochem *79*, 803-833.

Merrifield, C.J., and Kaksonen, M. (2014). Endocytic accessory factors and regulation of clathrin-mediated endocytosis. Cold Spring Harb Perspect Biol *6*, a016733.

Mettlen, M., Loerke, D., Yarar, D., Danuser, G., and Schmid, S.L. (2010). Cargo- and adaptor-specific mechanisms regulate clathrin-mediated endocytosis. J Cell Biol *188*, 919-933.

Middleton, E.R., and Rhoades, E. (2010). Effects of Curvature and Composition on alpha-Synuclein Binding to Lipid Vesicles. Biophysical Journal *99*, 2279-2288.

Mim, C., and Unger, V.M. (2012). Membrane curvature and its generation by BAR proteins. Trends Biochem Sci *37*, 526-533.

Minc, N., Boudaoud, A., and Chang, F. (2009). Mechanical forces of fission yeast growth. Curr Biol *19*, 1096-1101.

Moore, D.J., West, A.B., Dawson, V.L., and Dawson, T.M. (2005). Molecular pathophysiology of Parkinson's disease. Annual review of neuroscience *28*, 57-87.

Mooren, O.L., Galletta, B.J., and Cooper, J.A. (2012). Roles for actin assembly in endocytosis. Annu Rev Biochem *81*, 661-686.

Moseley, J.B. (2013). An expanded view of the eukaryotic cytoskeleton. Mol Biol Cell *24*, 1615-1618.

Mund, M., van der Beek, J.A., Deschamps, J., Dmitrieff, S., Monster, J.L., Picco, A., Nedelec, F., Kaksonen, M., and Ries, J. (2017). Systematic analysis of the molecular architecture of endocytosis reveals a nanoscale actin nucleation template that drives efficient vesicle formation. bioRxiv.

Nakamura, K. (2013). alpha-Synuclein and Mitochondria: Partners in Crime? Neurotherapeutics *10*, 391-399.

Nath, A., and Rhoades, E. (2013). A flash in the pan: dissecting dynamic amyloid intermediates using fluorescence. FEBS Lett *587*, 1096-1105.

Olivera-Couto, A., Grana, M., Harispe, L., and Aguilar, P.S. (2011). The eisosome core is composed of BAR domain proteins. Mol Biol Cell *22*, 2360-2372.

Olivera-Couto, A., Salzman, V., Mailhos, M., Digman, M.A., Gratton, E., and Aguilar, P.S. (2015). Eisosomes are dynamic plasma membrane domains showing pil1-lsp1 heteroligomer binding equilibrium. Biophys J *108*, 1633-1644.

Outeiro, T.F., and Lindquist, S. (2003). Yeast cells provide insight into alpha-synuclein biology and pathobiology. Science *302*, 1772-1775.

Pandey, A.P., Haque, F., Rochet, J.C., and Hovis, J.S. (2009). Clustering of α-Synuclein on Supported Lipid Bilayers: Role of Anionic Lipid, Protein, and Divalent Ion Concentration. Biophys J *96*, 540-551.

Payne, G.S., and Schekman, R. (1985). A test of clathrin function in protein secretion and cell growth. Science *230*, 1009-1014.

Pearse, B.M. (1976). Clathrin: a unique protein associated with intracellular transfer of membrane by coated vesicles. Proceedings of the National Academy of Sciences *73*, 1255-1259.

Peter, B.J., Kent, H.M., Mills, I.G., Vallis, Y., Butler, P.J., Evans, P.R., and McMahon, H.T. (2004). BAR domains as sensors of membrane curvature: the amphiphysin BAR structure. Science *303*, 495-499.

Picco, A., Mund, M., Ries, J., Nedelec, F., and Kaksonen, M. (2015). Visualizing the functional architecture of the endocytic machinery. Elife *4*.

Pollard, T.D. (2016). Actin and Actin-Binding Proteins. Cold Spring Harb Perspect Biol *8*.

Pollard, T.D., and Borisy, G.G. (2003). Cellular motility driven by assembly and disassembly of actin filaments. Cell *112*, 453-465.

Quan, J., and Tian, J. (2009). Circular polymerase extension cloning of complex gene libraries and pathways. PLoS One *4*, e6441.

Reis, C.R., Chen, P.H., Srinivasan, S., Aguet, F., Mettlen, M., and Schmid, S.L. (2015). Crosstalk between Akt/GSK3beta signaling and dynamin-1 regulates clathrin-mediated endocytosis. EMBO J *34*, 2132-2146.

Reuel, N.F., Bojo, P., Zhang, J., Boghossian, A.A., Ahn, J.H., Kim, J.H., and Strano, M.S. (2012). NoRSE: noise reduction and state evaluator for high-frequency single event traces. Bioinformatics *28*, 296-297.

Robinson, M.S. (2015). Forty Years of Clathrin-coated Vesicles. Traffic *16*, 1210-1238.

Roland, J., Berro, J., Michelot, A., Blanchoin, L., and Martiel, J.L. (2008). Stochastic severing of actin filaments by actin depolymerizing factor/cofilin controls the emergence of a steady dynamical regime. Biophys J *94*, 2082-2094.

Roth, T.F., and Porter, K.R. (1964). Yolk Protein Uptake in the Oocyte of the Mosquito Aedes Aegypti. L. J Cell Biol *20*, 313-332.

Roux, A., Uyhazi, K., Frost, A., and De Camilli, P. (2006). GTP-dependent twisting of dynamin implicates constriction and tension in membrane fission. Nature *441*, 528-531.

Rust, M.J., Bates, M., and Zhuang, X. (2006). Sub-diffraction-limit imaging by stochastic optical reconstruction microscopy (STORM). Nat Methods *3*, 793-795.

Saheki, Y., and De Camilli, P. (2012). Synaptic vesicle endocytosis. Cold Spring Harb Perspect Biol *4*, a005645.

Sahl, S.J., Hell, S.W., and Jakobs, S. (2017). Fluorescence nanoscopy in cell biology. Nat Rev Mol Cell Biol *18*, 685-701.

Schindelin, J., Arganda-Carreras, I., Frise, E., Kaynig, V., Longair, M., Pietzsch, T., Preibisch, S., Rueden, C., Saalfeld, S., Schmid, B., Tinevez, J.Y., White, D.J.,

Hartenstein, V., Eliceiri, K., Tomancak, P., and Cardona, A. (2012). Fiji: an open-source platform for biological-image analysis. Nat Methods *9*, 676-682.

Schneider, C.A., Rasband, W.S., and Eliceiri, K.W. (2012). NIH Image to ImageJ: 25 years of image analysis. Nature Methods *9*, 671-675.

Shi, Z., and Baumgart, T. (2015). Membrane tension and peripheral protein density mediate membrane shape transitions. Nat Commun *6*, 5974.

Simunovic, M., Evergren, E., Golushko, I., Prevost, C., Renard, H.F., Johannes, L., McMahon, H.T., Lorman, V., Voth, G.A., and Bassereau, P. (2016). How curvature-generating proteins build scaffolds on membrane nanotubes. Proceedings of the National Academy of Sciences of the United States of America *113*, 11226-11231.

Simunovic, M., Manneville, J.B., Renard, H.F., Evergren, E., Raghunathan, K., Bhatia, D., Kenworthy, A.K., Voth, G.A., Prost, J., McMahon, H.T., Johannes, L., Bassereau, P., and Callan-Jones, A. (2017). Friction Mediates Scission of Tubular Membranes Scaffolded by BAR Proteins. Cell *170*, 172-184 e111.

Simunovic, M., Mim, C., Marlovits, T.C., Resch, G., Unger, V.M., and Voth, G.A. (2013). Protein-mediated transformation of lipid vesicles into tubular networks. Biophys J *105*, 711-719.

Simunovic, M., Voth, G.A., Callan-Jones, A., and Bassereau, P. (2015). When Physics Takes Over: BAR Proteins and Membrane Curvature. Trends Cell Biol *25*, 780-792.

Sirotkin, V., Berro, J., Macmillan, K., Zhao, L., and Pollard, T.D. (2010). Quantitative analysis of the mechanism of endocytic actin patch assembly and disassembly in fission yeast. Mol Biol Cell *21*, 2894-2904.

Skau, C.T., Courson, D.S., Bestul, A.J., Winkelman, J.D., Rock, R.S., Sirotkin, V., and Kovar, D.R. (2011). Actin filament bundling by fimbrin is important for endocytosis, cytokinesis, and polarization in fission yeast. J Biol Chem *286*, 26964-26977.

Skruzny, M., Brach, T., Ciuffa, R., Rybina, S., Wachsmuth, M., and Kaksonen, M. (2012). Molecular basis for coupling the plasma membrane to the actin cytoskeleton during clathrin-mediated endocytosis. Proc Natl Acad Sci U S A *109*, E2533-2542.

Smith, B.A., Gelles, J., and Goode, B.L. (2014). Single-molecule studies of actin assembly and disassembly factors. Methods Enzymol *540*, 95-117.

Smith, M.B., Kiuchi, T., Watanabe, N., and Vavylonis, D. (2013). Distributed actin turnover in the lamellipodium and FRAP kinetics. Biophys J *104*, 247-257.

Sochacki, K.A., Dickey, A.M., Strub, M.P., and Taraska, J.W. (2017). Endocytic proteins are partitioned at the edge of the clathrin lattice in mammalian cells. Nat Cell Biol *19*, 352-361.

Sochacki, K.A., and Taraska, J.W. (2017). Correlative Fluorescence Super-Resolution Localization Microscopy and Platinum Replica EM on Unroofed Cells. Methods Mol Biol *1663*, 219-230.

Song, L., Hennink, E.J., Young, I.T., and Tanke, H.J. (1995). Photobleaching kinetics of fluorescein in quantitative fluorescence microscopy. Biophys J *68*, 2588-2600.

Sorre, B., Callan-Jones, A., Manzi, J., Goud, B., Prost, J., Bassereau, P., and Roux, A. (2012). Nature of curvature coupling of amphiphysin with membranes depends on its bound density. Proc Natl Acad Sci U S A *109*, 173-178.

Spillantini, M.G., Crowther, R.A., Jakes, R., Hasegawa, M., and Goedert, M. (1998). alpha-Synuclein in filamentous inclusions of Lewy bodies from Parkinson's disease and dementia with lewy bodies. Proc Natl Acad Sci U S A *95*, 6469-6473.

Stachowiak, J.C., Hayden, C.C., and Sasaki, D.Y. (2010). Steric confinement of proteins on lipid membranes can drive curvature and tubulation. Proc Natl Acad Sci U S A *107*, 7781-7786.

Stagge, F., Mitronova, G.Y., Belov, V.N., Wurm, C.A., and Jakobs, S. (2013). SNAP-, CLIP- and Halo-tag labelling of budding yeast cells. PLoS One *8*, e78745.

Strádalová, V., Stahlschmidt, W., Grossmann, G., Blazikova, M., Rachel, R., Tanner, W., and Malinsky, J. (2009). Furrow-like invaginations of the yeast plasma membrane correspond to membrane compartment of Can1. J Cell Sci *122*, 2887-2894.

Suetsugu, S. (2016). Higher-order assemblies of BAR domain proteins for shaping membranes. Microscopy (Oxf) *65*, 201-210.

Sun, Y., Leong, N.T., Wong, T., and Drubin, D.G. (2015). A Pan1/End3/Sla1 complex links Arp2/3-mediated actin assembly to sites of clathrin-mediated endocytosis. Mol Biol Cell *26*, 3841-3856.

Sun, Y., Martin, A.C., and Drubin, D.G. (2006). Endocytic internalization in budding yeast requires coordinated actin nucleation and myosin motor activity. Dev Cell *11*, 33-46.

Sung, Y.H., and Eliezer, D. (2006). Secondary structure and dynamics of micelle bound beta- and gamma-synuclein. Protein Sci *15*, 1162-1174.

Taylor, M.J., Perrais, D., and Merrifield, C.J. (2011). A high precision survey of the molecular dynamics of mammalian clathrin-mediated endocytosis. PLoS Biol *9*, e1000604.

Tenreiro, S., Rosado-Ramos, R., Gerhardt, E., Favretto, F., Magalhaes, F., Popova, B., Becker, S., Zweckstetter, M., Braus, G.H., and Outeiro, T.F. (2016). Yeast reveals similar molecular mechanisms underlying alpha- and beta-synuclein toxicity. Human molecular genetics *25*, 275-290.

Theriot, J.A., and Mitchison, T.J. (1991). Actin microfilament dynamics in locomoting cells. Nature *352*, 126-131.

Ti, S.C., and Pollard, T.D. (2011). Purification of actin from fission yeast Schizosaccharomyces pombe and characterization of functional differences from muscle actin. J Biol Chem *286*, 5784-5792.

Trexler, A.J., and Rhoades, E. (2009). alpha-Synuclein Binds Large Unilamellar Vesicles as an Extended Helix. Biochemistry *48*, 2304-2306.

Tweten, D.J., Bayly, P.V., and Carlsson, A.E. (2017). Actin growth profile in clathrin-mediated endocytosis. Phys Rev E *95*, 052414.

Ulmer, T.S., and Bax, A. (2005). Comparison of structure and dynamics of micelle-bound human alpha-synuclein and Parkinson disease variants. Journal of Biological Chemistry *280*, 43179-43187.

Ulmer, T.S., Bax, A., Cole, N.B., and Nussbaum, R.L. (2005). Structure and dynamics of micelle-bound human alpha-synuclein. Journal of Biological Chemistry *280*, 9595-9603.

Uno, S.N., Kamiya, M., Yoshihara, T., Sugawara, K., Okabe, K., Tarhan, M.C., Fujita, H., Funatsu, T., Okada, Y., Tobita, S., and Urano, Y. (2014). A spontaneously blinking fluorophore based on intramolecular spirocyclization for live-cell super-resolution imaging. Nat Chem *6*, 681-689.

Uversky, V.N., Li, J., Souillac, P., Millett, I.S., Doniach, S., Jakes, R., Goedert, M., and Fink, A.L. (2002). Biophysical properties of the synucleins and their propensities to fibrillate - Inhibition of alpha-synuclein assembly by beta- and gamma-synucleins. Journal of Biological Chemistry *277*, 11970-11978.

Vargas, K.J., Makani, S., Davis, T., Westphal, C.H., Castillo, P.E., and Chandra, S.S. (2014). Synucleins regulate the kinetics of synaptic vesicle endocytosis. J Neurosci *34*, 9364-9376.

Varkey, J., Isas, J.M., Mizuno, N., Jensen, M.B., Bhatia, V.K., Jao, C.C., Petrlova, J., Voss, J.C., Stamou, D.G., Steven, A.C., and Langen, R. (2010). Membrane Curvature Induction and Tubulation Are Common Features of Synucleins and Apolipoproteins. Journal of Biological Chemistry *285*, 32486-32493.

von Zastrow, M., and Williams, J.T. (2012). Modulating neuromodulation by receptor membrane traffic in the endocytic pathway. Neuron *76*, 22-32.

Walther, T.C., Brickner, J.H., Aguilar, P.S., Bernales, S., Pantoja, C., and Walter, P. (2006). Eisosomes mark static sites of endocytosis. Nature *439*, 998-1003.

Wang, X., Galletta, B.J., Cooper, J.A., and Carlsson, A.E. (2016). Actin-Regulator Feedback Interactions during Endocytosis. Biophys J *110*, 1430-1443.

Watanabe, N., and Mitchison, T.J. (2002). Single-molecule speckle analysis of actin filament turnover in lamellipodia. Science *295*, 1083-1086.

Watanabe, S., Rost, B.R., Camacho-Perez, M., Davis, M.W., Sohl-Kielczynski, B., Rosenmund, C., and Jorgensen, E.M. (2013). Ultrafast endocytosis at mouse hippocampal synapses. Nature *504*, 242-247.

Weinberg, J., and Drubin, D.G. (2012). Clathrin-mediated endocytosis in budding yeast. Trends Cell Biol *22*, 1-13.

Westphal, C.H., and Chandra, S.S. (2013). Monomeric Synucleins Generate Membrane Curvature. Journal of Biological Chemistry *288*, 1829-1840.

Wu, J.Q., McCormick, C.D., and Pollard, T.D. (2008). Counting proteins in living cells by quantitative fluorescence microscopy with internal standards. Methods Cell Biol *89*, 253-273.

Wu, J.Q., and Pollard, T.D. (2005). Counting cytokinesis proteins globally and locally in fission yeast. Science *310*, 310-314.

Wu, X., Zhao, X., Baylor, L., Kaushal, S., Eisenberg, E., and Greene, L.E. (2001). Clathrin exchange during clathrin-mediated endocytosis. J Cell Biol *155*, 291-300.

Wu, X., Zhao, X., Puertollano, R., Bonifacino, J.S., Eisenberg, E., and Greene, L.E. (2003). Adaptor and clathrin exchange at the plasma membrane and trans-Golgi network. Mol Biol Cell *14*, 516-528.

Wu, X.S., Lee, S.H., Sheng, J., Zhang, Z., Zhao, W.D., Wang, D., Jin, Y., Charnay, P., Ervasti, J.M., and Wu, L.G. (2016). Actin Is Crucial for All Kinetically Distinguishable Forms of Endocytosis at Synapses. Neuron *92*, 1020-1035.

Yamashiro, S., Mizuno, H., Smith, M.B., Ryan, G.L., Kiuchi, T., Vavylonis, D., and Watanabe, N. (2014). New single-molecule speckle microscopy reveals modification of the retrograde actin flow by focal adhesions at nanometer scales. Mol Biol Cell *25*, 1010-1024.

Yu, J. (2016). Single-Molecule Studies in Live Cells. Annu Rev Phys Chem *67*, 565-585.

Zemel, A., Ben-Shaul, A., and May, S. (2008). Modulation of the spontaneous curvature and bending rigidity of lipid membranes by interfacially adsorbed amphipathic peptides. Journal of Physical Chemistry B *112*, 6988-6996.

Zhu, C., Das, S.L., and Baumgart, T. (2012). Nonlinear Sorting, Curvature Generation, and Crowding of Endophilin N-BAR on Tubular Membranes. Biophysical Journal *102*, 1837-1845.

Ziolkowska, N.E., Karotki, L., Rehman, M., Huiskonen, J.T., and Walther, T.C. (2011). Eisosome-driven plasma membrane organization is mediated by BAR domains. Nat Struct Mol Biol *18*, 854-856.